Ph.D. DISSERTATION

Compliance-Based Peg-in-Hole Strategy for Assembly Task with Uncertainty

불확실성을 포함하는 조립작업을 위한 컴플라이언스 기반 펙인홀 전략

BY

HYEONJUN PARK

AUGUST 2020

DEPARTMENT OF TRANSDISCIPLINARY STUDIES
THE GRADUATE SCHOOL OF CONVERGENCE
SCIENCE AND TECHNOLOGY
SEOUL NATIONAL UNIVERSITY

Ph.D. DISSERTATION

Compliance-Based Peg-in-Hole Strategy for Assembly Task with Uncertainty

불확실성을 포함하는 조립작업을 위한 컴플라이언스 기반 펙인홀 전략

BY

HYEONJUN PARK

AUGUST 2020

DEPARTMENT OF TRANSDISCIPLINARY STUDIES
THE GRADUATE SCHOOL OF CONVERGENCE
SCIENCE AND TECHNOLOGY
SEOUL NATIONAL UNIVERSITY

Compliance-Based Peg-in-Hole Strategy for Assembly Task with Uncertainty

불확실성을 포함하는 조립작업을 위한 컴플라이언스 기반 펙인홀 전략

지도교수 박 재 흥

이 논문을 공학박사 학위논문으로 제출함

2020년 7월

서울대학교 대학원

융합과학부

박 현 준

박현준의 공학박사 학위 논문을 인준함

2020년 6월

위 원 장	안 정 호	(인)
부위원장	박 재 흥	(인)
위 원	이 동 준	(인)
위 원	최 영 진	(인)
위 원	배 지 훈	(인)

Abstract

The peg-in-hole assembly is a representative robotic task that involves physical contact with the external environment. The strategies generally involve performing the assembly task by estimating the contact state between the peg and the hole. The contact forces and moments, measured using force sensors, are primarily used to estimate the contact state. In this paper, in contrast to past research in the area, which has involved the utilization of such expensive devices as force/torque sensors or remote compliance mechanisms, an inexpensive method is proposed for peg-in-hole assembly without force feedback or passive compliance mechanisms. The method consists of an analysis of the state of contact between the peg and the hole as well as a strategy to overcome the inevitable positional uncertainty of the hole incurred in the recognition process. A control scheme was developed to yield compliant behavior from the robot with physical contact under the condition of hybrid position/force control. Proposed peg-in-hole strategy is based on compliance characteristics and generating the force and moment. The peg is inserted into the hole as it adapts to the external environment. The effectiveness of the proposed method was experimentally verified using a humanoid upper body robot with fifty degrees of freedom and a peg-in-hole apparatus with a small clearance (0.1 mm). Three cases of experiments were conducted; Assembling the peg attached to the arm in the hole fixed in the external environment, grasping a peg with an anthropomorphic hand and assembling it into a fixed hole, and grasping both peg and hole with both hands and assembling each other. In order to assemble the peg-in-hole through the proposed strategy by the humanoid upper body robot, I present a

method of gripping an object, estimating the kinematics of the gripped object, and manipulating the gripped object. In addition to the cost aspect, which is the fundamental motivation for the proposed strategy, the experimental results show that the proposed strategy has advantages such as fast assembly time and high success rate, but has the disadvantage of unpredictable elapsed time. The reason for having a high variance value for the success time is that the spiral trajectory, which is most commonly used, is used. In this study, I analyze the efficiency of spiral force trajectory and propose an improved force trajectory. The proposed force trajectory reduces the distribution of elapsed time by eliminating the uncertainty in the time required to find a hole. The efficiency of the force trajectory is analyzed numerically, verified through repeated simulations, and verified by the actual experiment with humanoid upper body robot developed by Korea institute of industrial technology.

keywords: Compliant assembly, Peg-in-hole, Force control

student number: 2014-30817

Contents

List of Tables

List of Figures

Chapter 1

INTRODUCTION

1.1 Motivation: Peg-in-Hole Assembly

peg-in-hole assembly is an essential task in assembly processes in various fields, such as manufacturing lines. The performance of this task using robots significantly expands the field of practical applications of robotics research. A robotic peg-in-hole task can be performed based on pure position control if accurate position of the relevant object (i.e., the hole) is provided and the position control error of the robot is zero. However, in practice, these conditions can only be obtained with specialized robots designed for a limited class of purposes. In the case of more versatile robots, such as industrial manipulators, some magnitude of position error is inevitable due to imperfect sensors and mechanical errors generated by the robot.

While a human performs the assembly task, the position of the assembly parts is roughly recognized by sight, and mating parts are fitted by touch. In

case of robots, sight can be replaced by cameras and touch by force/torque (F/T) sensors. In past research, cameras were used to extract the boundaries of the object and inspect the overall process of the peg-in-hole task [1], [2]. Micro-peg-in-hole tasks with a peg of diameter 88 μm and a hole of 100 μm were performed using visual feedback in [3]. Tele-operation peg-in-hole tasks were researched using a vision system and a human motion-capture system in [4][5].

Another conventional method to perform peg-in-hole tasks involves the utilization of an F/T sensor commonly installed on the wrist of the robot's arm. Shirinzadeh et al. presented a comprehensive study of robot-based cylindrical peg-in-hole tasks [6]. The F/T sensor accurately detects the force of contact and thus helps compensate for the positional uncertainty of the object. Moreover, the sensor enables stable contact between the peg and the hole through real-time contact force feedback [7]-[9]. Newman et al. proposed a force torque map consisting of force and torque values of each contact point [10]. The location of the hole was estimated using the measured reaction moment occurred by the contact [11], [12].

1.2 Contributions of Thesis

It is obvious that performing peg-in-hole tasks without F/T sensors is more cost efficient than with them. The contact force feedback increases overall system cost and operation time, and requires a significantly high control frequency. Therefore, some research to estimate the state of contact using joint position sensors has been being conducted [13]-[15]. The authors of this study have shown

in past work that the robotic peg-in-hole task can be accomplished without contact force information and inaccurate vision data[16]. In the relevant study, an intuitive assembly strategy inspired by human behavior was proposed, where the peg was rubbed at a point close to the location of the hole until the relevant objects were mated using compliant characteristics. The compliance enabled stable contact between the peg and the hole without force feedback by allowing the robot to softly adapt to the external object, i.e., the hole [17]-[20].

In this paper, an advanced strategy for robotic peg-in-hole tasks is proposed based on analyzing and investigating the peg-in-hole process. The strategy is independent of external devices such as F/T sensors or Remote-center-compliance devices[21]. The method presented in this paper does not require a force analysis process for contact points in peg and hole. The absence of force feedback helps reduce task time and overall system cost[22].

1.3 Overview of Thesis

The proposed strategy consists of three parts. The first involves the designing of four unit motions based on an analysis of the state of contact during the peg-in-hole procedure with positional uncertainty. The second part consists of a method to estimate contact conditions to check the strategy using kinematical information without force feedback. This method was ideally designed and experimentally tuned. The third part of the proposed strategy involves a control scheme to implement compliant robotic behavior.

In Section II, I analyze the contact state of the peg-in-hole task, and propose the strategy for the construction of the four unit motions. The control

framework for compliance behavior and the controller for the implementation of the proposed strategy are described. For the verification of the proposed design, three cases of peg-in-hole experiments were carried out using a manipulator with fifty degrees of freedom (DoF) that had inaccurate hole information provided by KINECT^{TM}.

In Section III, I analyze the problems of adopting the most commonly used spiral trajectory as the force trajectory of the proposed strategy, and propose an improved force trajectory. In order to compare the performance of the peg-in-hole strategy with the proposed force trajectory compared to the spiral force trajectory, iterative simulations and experiments are performed.

Chapter 2

COMPLIANCE BASED STRATEGY

2.1 Background & Related Works

The peg-in-hole assembly process begins with uncertain geometrical information about the hole. The peg-in-hole strategy corrects these errors and helps to ensure that the assembly is appropriately performed. The common approach is to use a force sensor. When the peg and the hole are in contact, the contact force and the moment are measured using the force sensor, and then the contact state is estimated based on the measurements. The method using a force-torque map is a representative force feedback strategy. This method maps, in advance, the force and moment data to the contact state. During the peg-in-hole operation, the contact state is estimated, and the motion of the peg corresponding to the current state is generated. Peg-in-hole assembly using learning has also been studied extensively[23]-[25]. Reinforcement learning in peg-in-hole assembly is a learning sequence of optimal actions by exploring the environment to maximize the expected reward. The current position of the peg, the contact force between

the peg and the hole, and the contact moment are set as the current state, and the force and moment applied to the peg are defined as the action. The peg-in-hole operation is performed by selecting the action with the highest reward in the current state.

2.2 Analysis of Peg-in-Hole Procedure

Fig. 2.1 shows four states involving a peg and a hole while the peg is in contact with the hole under a force pushing the peg toward the hole. Fig. 2.1(a) shows a planar contact state between the bottom of the peg and the top of the hole. This situation generally arises when the center of the bottom of the peg is located beyond the surface of the hole. If the center of the peg is close to the hole, (assuming the existence of a compliant robot), the peg is tilted and two-point contact occurs, as shown in Fig. 2.1(b). In this configuration, slippage at the contact points is allowable, because of which the peg can be moved along the edge of the hole in order to maintain two-point contact. Three-point contact is

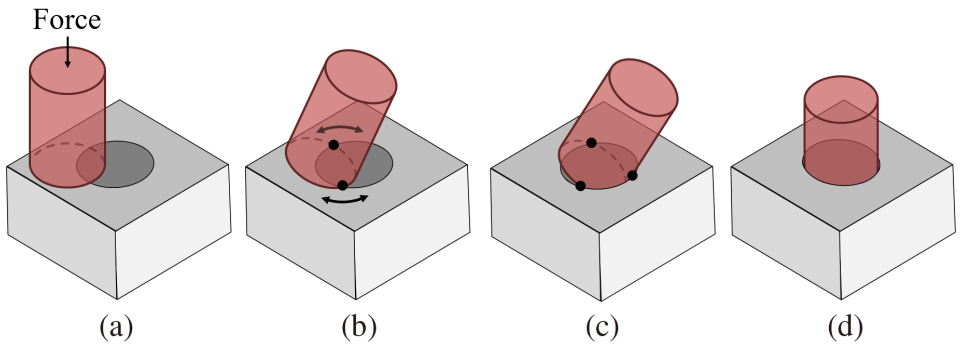

Figure 2.1: State of contact of cylindrical peg and hole under assembly force. (a) Bottom plane contact. (b) Two-point contact. (c) Three-point contact. (d) Side-plane contact.

shown in Fig. 2.1(c), and occurs when the center of the bottom of the peg and the hole are close enough but the tilting angle of the peg persists. If the tiling angle is zero, the peg naturally falls into the hole, as shown in Fig. 2.1(d). These are the four states generally observed in the peg-in-hole process. Based on this observation, the remainder of this sub-section presents a more detailed analysis of the peg-in-hole process, using which I devise a strategy for the sensorless peg-in-hole process.

Analysis of the two-point contact state is important because it is the most frequent situation encountered in the peg-in-hole process. Obtaining the two-point contact state is not difficult. As mentioned above, it can be simply achieved by placing the center of the bottom of the peg on any area of the hole, which means that the allowable positional uncertainty of the peg is as great in magnitude as the size of the hole. In serial manipulators, the absolute positional error of the end effector, i.e., the peg, mainly arises due to the mechanical misalignment of joints. The magnitude of the positional error is of the order of millimeters, which is far smaller than the radius of the hole in general. Therefore, most peg-in-hole tasks start from the two-point contact state.

2.2.1 Contact Analysis

I assume that the peg is in the two-point contact state. Fig. 2.2 shows a diagram of the two-point contact situation at points B and C. The peg is tilted along the straight line connecting B and C. The diagram shows a force that pushes the peg toward the hole, hereafter called the "assembly force." The assembly force $\boldsymbol{f}_{\mathrm{a}}$ shown in Fig. 2.2(a) induces reaction forces $\boldsymbol{f}_{\mathrm{A}}$ and $\boldsymbol{f}_{\mathrm{B}}$ at contact points A and B. Note that the sum of these reaction forces, $\boldsymbol{f}_{\mathrm{sum}}$, is always directed

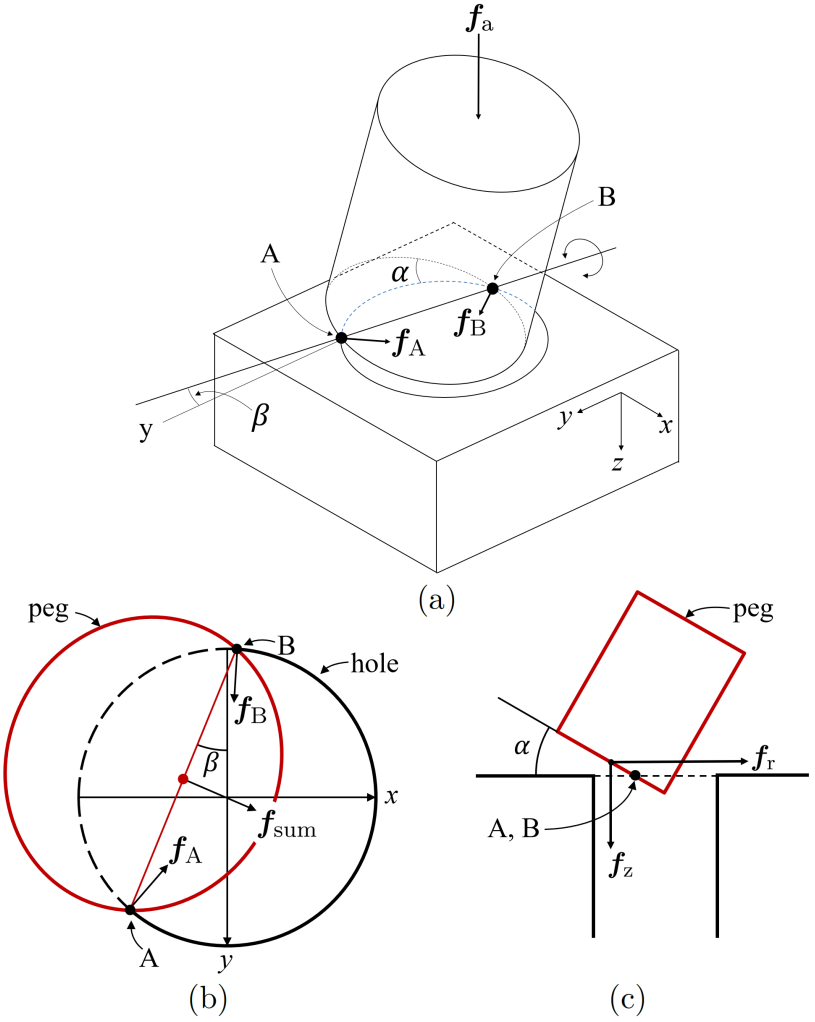

Figure 2.2: Two-point contact state of cylindrical peg and hole. (a) Diagram of the state. (b) Top view. (c) Side view.

toward the center of the hole as long as the assembly force $\boldsymbol{f}_a$ is applied. If friction at the contact point is ignored, the peg spontaneously starts to slip due to $\boldsymbol{f}_{sum}$. This slippage guides the peg into the center of the hole. This "natural attraction" is the main reason for how peg-in-hole tasks as well as general assembly tasks can be successfully accomplished even with positional uncertainty.

While $\boldsymbol{f}_{\mathrm{sum}}$ contributes as the main source of the force to attract the peg into the hole, static friction at the contact points hinders the peg from moving. To overcome friction, an additional force can be considered. Generating this additional force is the most important part of the peg-in-hole problem.

2.2.2 Basic Idea

I assume a new assembly force, $\boldsymbol{f}_{\mathrm{d}}$, which replaces the original assembly force $\boldsymbol{f}_{\mathrm{a}}$. An example of $\boldsymbol{f}_{\mathrm{d}}$ is as follows:

$$
\begin{aligned}
\boldsymbol{f}_{\mathrm{d}} &= \boldsymbol{f}_{\mathrm{r}} + \boldsymbol{f}_{\mathrm{z}}, \\
\boldsymbol{f}_{\mathrm{r}} &= \begin{bmatrix} f_{\mathrm{r}}\cos\hat{\beta} & f_{\mathrm{r}}\sin\hat{\beta} & 0 \end{bmatrix}^{\mathrm{T}}, \\
\boldsymbol{f}_{\mathrm{z}} &= \begin{bmatrix} 0 & 0 & f_{\mathrm{z}} \end{bmatrix}^{\mathrm{T}}.
\end{aligned}
\tag{2.1}
$$

Forces $\boldsymbol{f}_{\mathrm{r}}$ and $\boldsymbol{f}_{\mathrm{z}}$ denote the projection component of the assembly force $\boldsymbol{f}_{\mathrm{d}}$ on the xy-plane and the z-axis, respectively. f_{r} and f_{z} are magnitudes of the projection component forces, respectively, $\hat{\beta}$ denotes the estimated tilting angle β, which is defined as the angle between the straight line connecting the two contact points and the y-axis as shown in Fig. 2.2(a) and (b). If $\hat{\beta}$ is precisely calculated, the direction of $\boldsymbol{f}_{\mathrm{r}}$ is the same as that of $\boldsymbol{f}_{\mathrm{sum}}$. Then, the summation of $\boldsymbol{f}_{\mathrm{sum}}$ and $\boldsymbol{f}_{\mathrm{r}}$ moves the peg into the hole, thus overcoming the frictional force.

Estimating β generally requires an additional sensor, such as a vision system or a six-axis F/T sensor at the wrist of the robot. Moreover, these sensory inputs should be updated in real time (β is changed in real time), because of which a

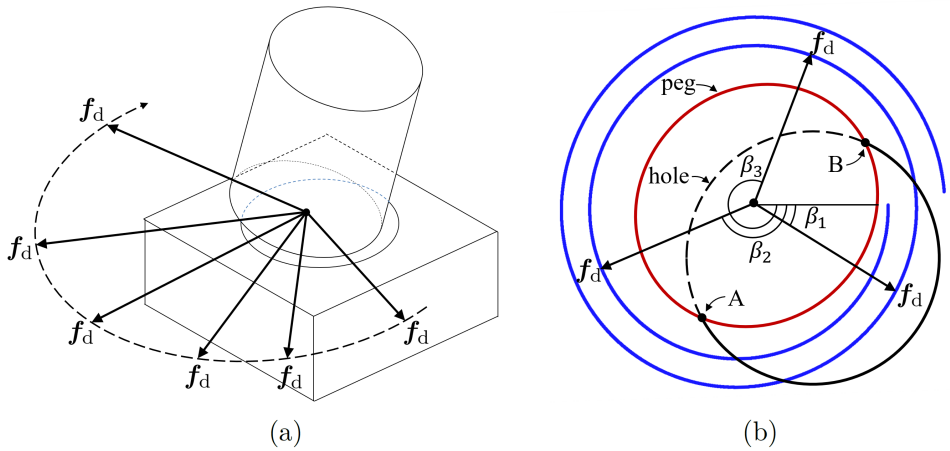

Figure 2.3: Overcoming uncertainty in the contact situation. (a) Generating force in various directions. (b) The spiral trajectory of the force vector.

certain form of feedback is necessary.

In this paper, I propose a method to avoid the above complexities. In fact, the main role of $\boldsymbol{f}_{\mathrm{r}}$ is to "kick" the peg to overcome static friction at the contact points. Note that this "kick out" occurs when $\boldsymbol{f}_{\mathrm{r}}$ and $\boldsymbol{f}_{\mathrm{sum}}$ are in the same direction. If not, the forces are canceled out and the peg does not move due to static friction. Once the peg starts to move, it tends to keep moving toward the center of the hole due to $\boldsymbol{f}_{\mathrm{sum}}$. This observation leads to the superfluity of precise measurement and real-time feedback of the value of β using additional sensors.

The proposed idea can be roughly described as arbitrary selection and continuous change in the value of $\hat{\beta}$. In this idea, once $\hat{\beta}$ accidentally matches β, the peg is quickly drawn into the center of the hole. More precisely, I simultaneously increase and decrease f_{r} and $\hat{\beta}$, respectively, in a certain range while keeping f_{z} fixed. This results in a time-varying force vector $\boldsymbol{f}_{\mathrm{r}}$ whose trajectory draws a spiral shape, as shown in Fig. 2.3. This spiral force first enables state

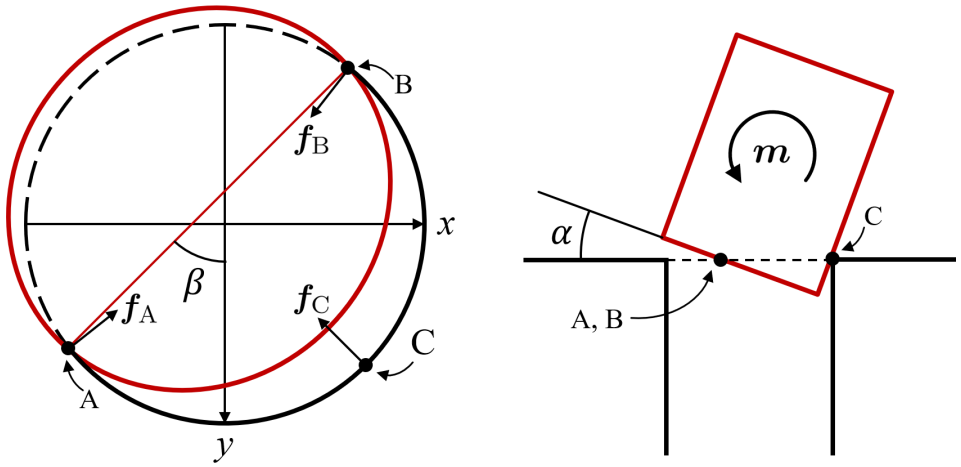

(a) (b)

Figure 2.4: Three-point contact state of a cylindrical peg and hole (a) top view; (b) side view.

transitions from planar contact to two-point contact. Assuming the peg is in planar contact, the spiral force makes the peg sweep a certain circular area on the surface of the hole. If the hole exists in the swept area, the peg is eventually caught by the hole and two-point contact occurs. At this time, the spiral force also enables the state transition to escape the two-point contact. The spiral force then makes the peg move, overcoming friction at the contact points, such that the peg is naturally attracted to the hole.

When the peg is drawn into the center of the hole, there are two possibilities. If the tilt angle α is zero, the peg tends to immediately fall into the hole; otherwise, the three-point contact configuration occurs. Fig. 2.4 shows three-point contact from the top and side. In order to insert the peg into the hole from the three-point contact state, an additional moment $\boldsymbol{m}$ related to α and β is needed to rotate the peg to reduce the value of α. Since α and β are unknown, a moment is also generated with $\hat{\alpha}$, which is an arbitrarily selected value of α.

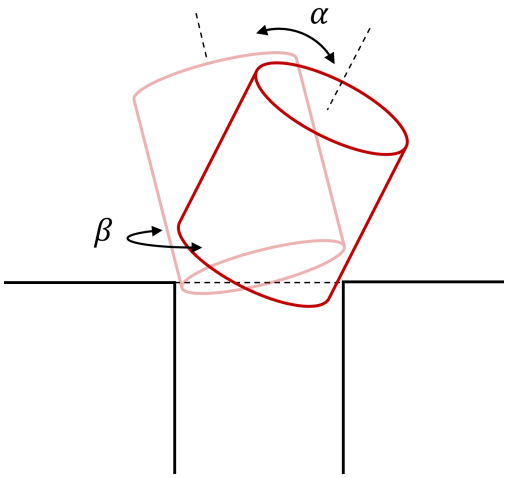

Figure 2.5: Movement of the peg necessary to overcome the rotation uncertainty of the hole.

Similarly to $\hat{\beta}$, $\hat{\alpha}$ continuously increases and decreases until the peg is inserted into the hole. Fig. 2.5 shows movement of the peg rotating about $\hat{\alpha}$ and $\hat{\beta}$.

In the next sub-section, I formulate expressions for a number of physical motions of the robot to implement the above forces.

2.3 Peg-in-Hole Strategy

2.3.1 Unit Motions

Based on the analysis of contact states, I designed four unit motions to implement the peg-in-hole task as shown in Fig. 2.6. The unit motions were "pushing," "rubbing," "wiggling," and "screwing." The "pushing" motion provided the z-axis component of the assembly force, which corresponded to $\boldsymbol{f}_z$ in (2.1). The "rubbing" motion provided the x-y plane component of the assembly force

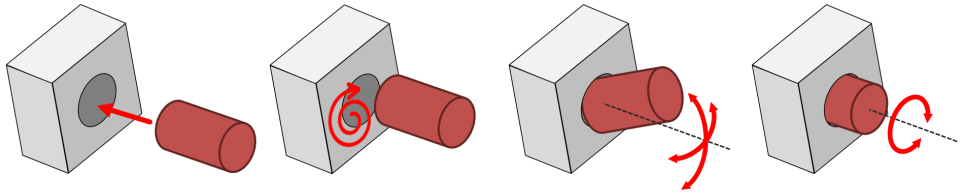

Figure 2.6: Unit motions for peg-in-hole assembly. (a) Pushing. (b) Rubbing. (c) Wiggling. (d) Screwing.

corresponding to $\boldsymbol{f}_{\mathrm{r}}$ in (2.1).

The "wiggling" motion created the arbitrarily generated moment $\boldsymbol{m}$ shown in Fig. 2.3(b). Finally, the "screwing" motion prevented jamming when the peg was being inserted into the hole. Pushing was achieved by single-axial force control in a feed-forward manner. Rubbing was implemented on two-axis positional control. The rubbing motion was drawn by using an Archimedes spiral, which has been proposed as the optimal scan trajectory [26], [27]. The wiggling and screwing motions were implemented by controlling the orientation of the peg.

2.3.2 State of Strategy

Fig. 2.7 shows the actual peg-in-hole procedure implemented by the proposed strategy. The process consisted of three steps and three conditions. Detailed explanations of the steps, involving a combination of the unit motions, are first addressed, followed by the conditions.

Reaching (accomplished by pushing): The peg-in-hole procedure begins with the reaching step, where the peg is outside the hole. In this step, the robot first measures the location of the hole (with some degree of positional uncer-

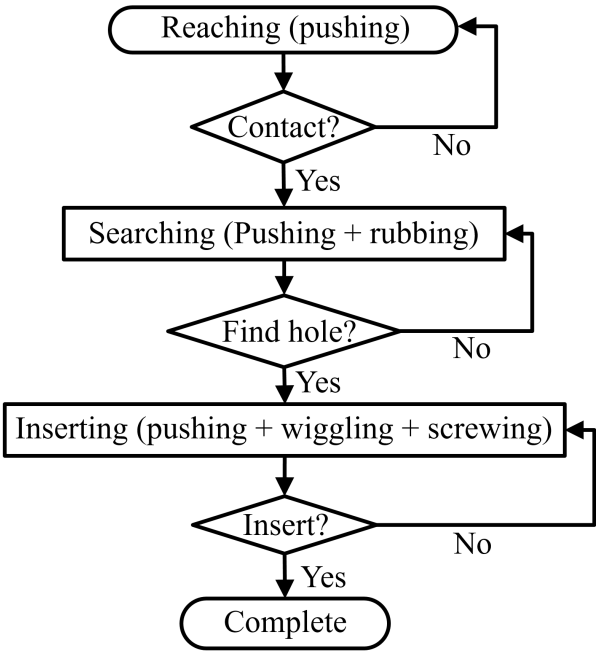

Figure 2.7: Flowchart of peg-in-hole procedure.

tainty), following which the assembly force is continuously activated until the peg touches the hole in the given object. When the task starts, the peg approaches the hole by the force generated by the "pushing" unit motion. From the inaccurately measured position of the hole, which includes some degree of uncertainty, the peg stops in the vicinity of the hole.

Searching (pushing + rubbing): Once the end of the peg is in contact with the object close to the hole, the location of the hole is discovered using the spiral motion shown in Fig. 2.6(b). In this task, the pushing and the rubbing unit motions provide the projected components of assembly force $\boldsymbol{f}_d$ along the z-axis and the xy plane. The spiral motion is generated and centered at the estimated hole position.

Inserting (pushing + wiggling + screwing): Once the location of the hole

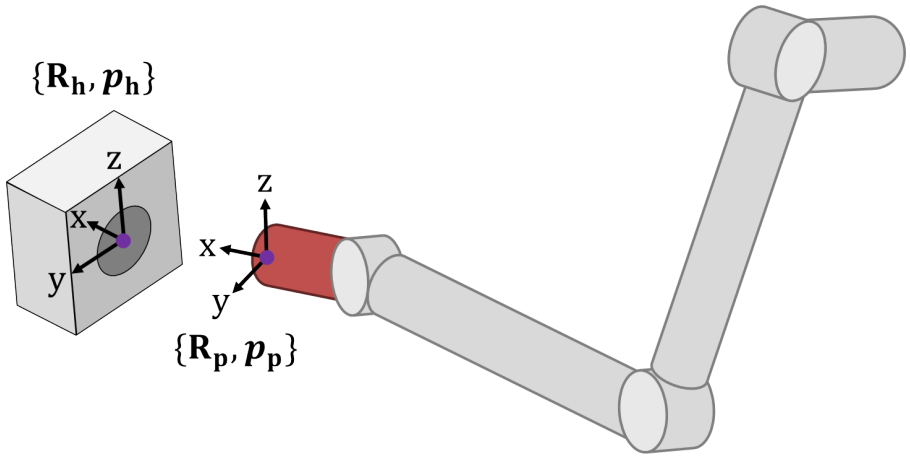

Figure 2.8: Local frame of the peg and the hole.

is found with three-point contact, the combined motions of pushing, wiggling, and screwing are activated. The wiggling shown in Fig. 2.6(c) helps the robot fit the peg in the hole by repeatedly rotating it along the vertical and horizontal planes. The screwing motion is used to reduce the frictional force and prevent the jamming of the peg.

2.3.3 Conditions for State Transition

The proposed strategy is carried out in the sequence: reaching, searching, and inserting. In order to transit into a subsequent task, several conditions to judge the success of each task are designed. Only the kinematical information of the manipulator, which can be obtained from the joint position sensors, is required for such determination.

Fig. 2.8 shows the local frames fixed on the peg and the hole, respectively. $\boldsymbol{R}_{\mathrm{p}}$ and $\boldsymbol{R}_{\mathrm{h}}$ denote the rotation matrices of the peg and the hole, respectively, and $\boldsymbol{p}_{\mathrm{p}}$ and $\boldsymbol{p}_{\mathrm{h}}$ denote the position vector of the end of the peg and the entrance

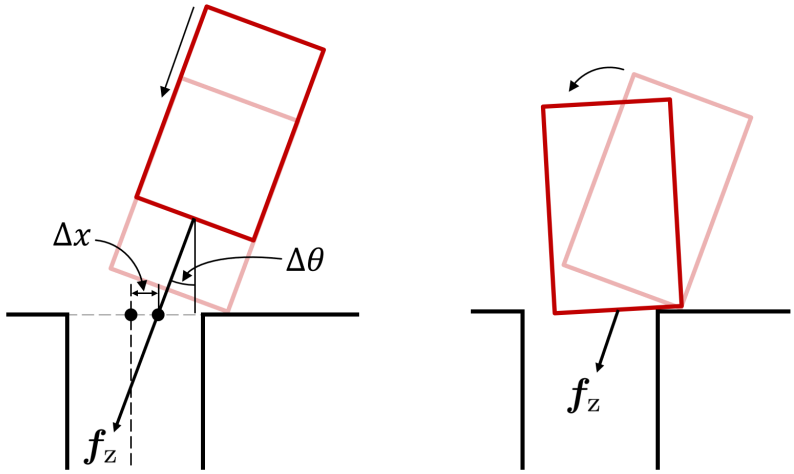

Figure 2.9: Reaching motions: (a) approaching the peg; (b) adapting to the hole.

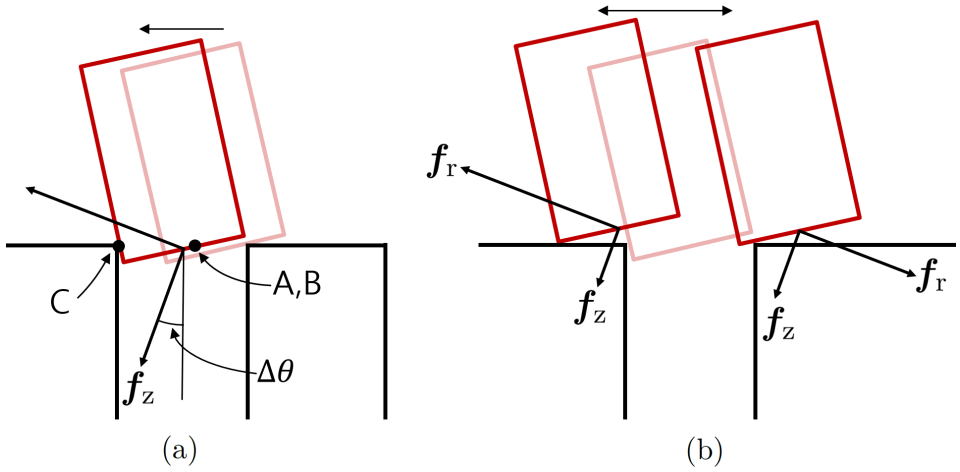

Figure 2.10: Movement of the peg due to the assembly force and spiral force: (a) finding the hole; (b) missing the hole.

of the hole, respectively. The goal of the peg-in-hole task can be expressed by that $\boldsymbol{p}_{\mathrm{p}}$ pass on the $\boldsymbol{p}_{\mathrm{h}}$ with same of $\boldsymbol{R}_{\mathrm{p}}$ and $\boldsymbol{R}_{\mathrm{h}}$.

When the peg-in-hole procedure starts with the reaching step, the approach of the peg is blocked by contact with the hole as shown in Fig. 2.9(a). The

recognition error of translation and rotation are expressed as Δx and $\Delta\theta$, respectively, in Fig. 2.9(a). If the peg is controlled with low-control gain, it is adapted to the hole as shown in Fig. 2.9(b). If Δx is smaller than the radius of the peg, the peg contacts the hole at two points. Otherwise, the peg is in planar contact with the object close to the hole. In both cases, the peg stops. The contact of the peg with the hole is recognized by observing the velocity of the peg. The condition of the contact state can be ideally expressed as $\dot{\boldsymbol{p}}_{\mathrm{p}} = 0$. $\dot{\boldsymbol{p}}_{\mathrm{p}}$ denotes the velocity of the peg calculated by forward kinematics.

After detecting contact, the strategy jumps to the searching step. The peg moves following the rubbing motion near the hole. When the robot finds the location of the hole with three-point contact, the configuration of the peg and the hole is set as shown in Fig. 2.10(a). Fig. 2.10(b) shows the configuration required to escape the hole due to imbalance in the z-axis assembly force $\boldsymbol{f}_{\mathrm{z}}$ and the spiral force $\boldsymbol{f}_{\mathrm{r}}$. The spiral force $\boldsymbol{f}_{\mathrm{r}}$ can be expressed as $k_{\mathrm{p}}(\boldsymbol{x}_{\mathrm{d}} - \boldsymbol{x}_{\mathrm{c}})$. k_{p} denotes proportional gain in Cartesian space. $\boldsymbol{x}_{\mathrm{d}}$ and $\boldsymbol{x}_{\mathrm{c}}$ represent the desired and given positions, respectively. If the force consists of $\boldsymbol{f}_{\mathrm{z}}$, and $\boldsymbol{f}_{\mathrm{r}}$ is suitable for stopping the peg, this configuration is defined as "find hold" and shown in Fig. 2.7. A balance in the magnitudes of $\boldsymbol{f}_{\mathrm{z}}$ and k_{p} is experimentally discussed in Section IV. Although the rubbing motion is still generated during the three-point contact of the peg and hole, the peg can be stopped due to balanced forces. Judging the three-point contact is also accomplished by using $\dot{\boldsymbol{p}}_{\mathrm{p}}$.

When the location of the hole is found, the peg-in-hole task jumps to the insertion step. The conclusion of the insertion state is that of the peg-in-hole task as well. The completion of the task is detected by $\dot{\boldsymbol{p}}_{\mathrm{p}} = 0$.

2.4 Control Frameworks

2.4.1 Control for Compliant Behavior

The equations of motion for an n-DoF manipulator are given by

$$\boldsymbol{A}(\boldsymbol{q})\ddot{\boldsymbol{q}} + \boldsymbol{b}(\boldsymbol{q}, \dot{\boldsymbol{q}}) + \boldsymbol{g}(\boldsymbol{q}) = \boldsymbol{\tau} + \boldsymbol{\tau}_{\text{ext}}, \tag{2.2}$$

where $\boldsymbol{A} \in \mathbb{R}^{n\times n}$, $\boldsymbol{b} \in \mathbb{R}^{n\times 1}$, and $\boldsymbol{g} \in \mathbb{R}^{\boldsymbol{n\times 1}}$ represent the inertial matrix, the vector of the centrifugal and the Coriolis forces, and gravity, respectively. $\boldsymbol{\tau}$ and $\boldsymbol{\tau}_{\text{ext}} \in \mathbb{R}^{n\times 1}$ denote the input torque vector for each joint and the joint torque vector associated by contact with the external environment, respectively. Fig. 2.13 shows the diagram of the state of contact between the robot and the external object. The contact force $\boldsymbol{f}_{\text{ext}}$ affects each joint to generate the external torque $\boldsymbol{\tau}_{\text{ext}}$.

The control framework is designed by combining conventional proposed controllers, such as the "Jacobian transpose controller(JTC) [28]", "task-oriented

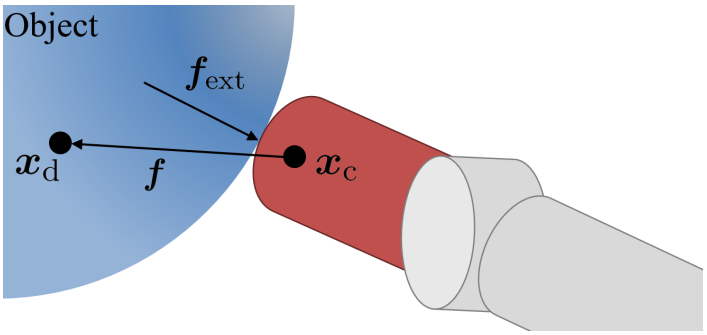

Figure 2.11: Contact between the robot and an object.

coordinate controller(TCC) [29][30]", and "force-motion separating controller(FSC) [31]". JTC was chosen as the basic framework because it better suited force generation tasks. TCC controlled the position and orientation of the end effector in the operational space and generated the required force in the desired direction. The FSC was used to separate force generation from position control. Position and rotation of the end-effector are controlled by feedback control, and force is generated in a feed-forward manner. The control framework for input torque $\boldsymbol{\tau}$, which considers the orientation of the end effector, gravity compensation, frictional compensation, and joint damping, can be expressed as follows:

$$\boldsymbol{\tau} = -\mathrm{C}\dot{\boldsymbol{q}} + \boldsymbol{J}^{\mathrm{T}} \begin{bmatrix} \boldsymbol{f} \\ \boldsymbol{m} \end{bmatrix} + \boldsymbol{\tau}_{\mathrm{g}} + \boldsymbol{\tau}_{\mathrm{fric}}, \tag{2.3}$$

where $\boldsymbol{\tau}_{\mathrm{g}} \in \mathbb{R}^{n\times 1}$ denotes the gravity-compensated torque vector, $\boldsymbol{J} \in \mathbb{R}^{6\times n}$ is a Jacobian matrix of the end effector, $\mathrm{C} \in \mathbb{R}^{n\times n}$ is a matrix for damping shaping in the joint space, and $\boldsymbol{f}$ and $\boldsymbol{m} \in \mathbb{R}^{3\times 1}$ denote the vectors of the force and the moment at the end effector.

The movements of the peg (e.g., move, rotate, and push) are generated by the wrench vector of $[\boldsymbol{f} \;\; \boldsymbol{m}]^{\mathrm{T}}$. Since $\boldsymbol{f}$ and $\boldsymbol{m}$ are chosen to be smaller than the force needed to fix the hole in the environment, the peg can likely be fitted to the shape and location of the hole.

In order for the manipulator to adapt to external contact force, the controller was designed to allow for error in the manipulator. In PID (proportional–differential–integral)-based position controllers, the integral gain eliminates the

steady state error, which generally occurs due to an external force. In order to preserve the effect of the external force, $\boldsymbol{f}$ is designed by using a proportional controller realized in Cartesian space [32]. The desired input force vector $\boldsymbol{f}$ is generated as (2.4) with the given position to the desired position of the end effector shown in Fig. 2.13.

$$\boldsymbol{f} = k_{\mathrm{p}}(\boldsymbol{x}_{\mathrm{d}} - \boldsymbol{x}_{\mathrm{c}}), \tag{2.4}$$

where k_{p} is the proportional gain constant, $\boldsymbol{x}_{\mathrm{d}}$ and $\boldsymbol{x}_{\mathrm{c}} \in \mathbb{R}^{3\times 1}$ denote the desired and the given position vectors, respectively. Determining k_{p} is important to ensuring compliant behavior. Setting k_{p} to a low value renders the robot softer.

Fig. 2.12(a) shows experiments environments for verification of compliance. The end point of the manipulator was set to follow the circular trajectory of the air, and an obstacle(table) was placed in the circular trajectory to check the contact stability. Fig. 2.12(b) show the desired and following trajectory graphs. Through the graph, it was clearly seen that stable contact occurs without vibration at the point where the robot contacts the table.

2.4.2 Friction Compensate

Back-drivability is essential for the robot to adapt to external forces. Joint friction compensation is a representative approach for making robots have compliance characteristics. Because friction is difficult to estimate the exact model nu-

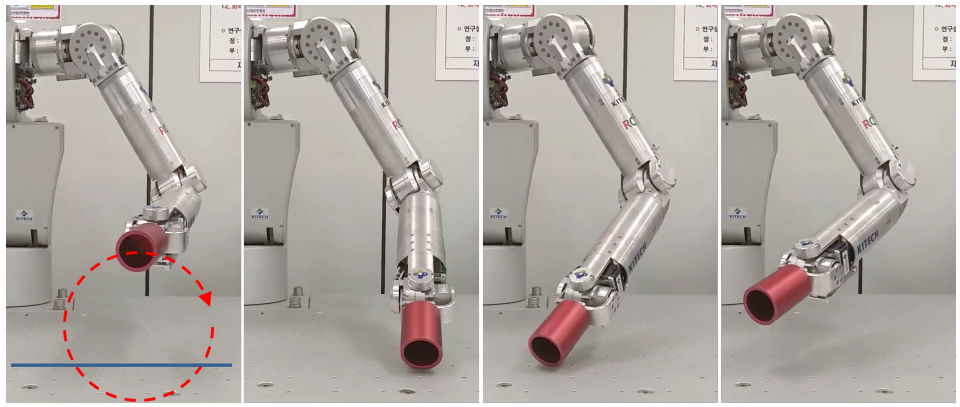

(a)

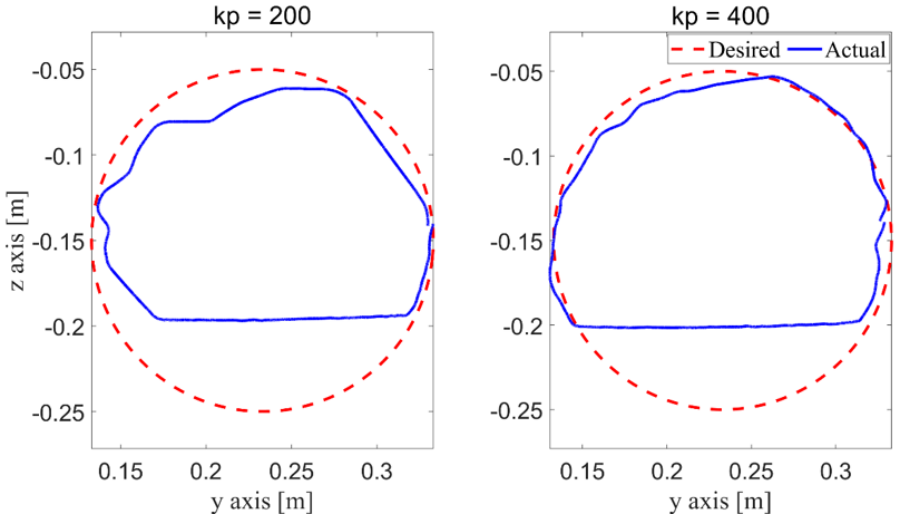

(b)

Figure 2.12: Compliance verification: contact stability experiment. (a) experiment environment, (b) desired and follow trajectories.

merically, friction-compensated torque is designed experimentally. The friction-compensated torque is generated in the direction of the angular velocity of each joint [33]. The friction-compensated torque used in this paper is as

$$\boldsymbol{\tau}_{\text{fric}} = \boldsymbol{f}_{\text{c}} \tanh(s_{\text{f}} \dot{\boldsymbol{q}}). \tag{2.5}$$

The tanh function was used to make the friction-compensated torque act linearly near the joint angular velocity of zero. $\boldsymbol{f}_{\text{c}}$ denotes the Coulomb friction constant matrix. The magnitude of $\boldsymbol{f}_{\text{c}}$ is correspond to friction of each joint. s_{f} is a constant that determines the slope of friction-compensated torque according to the joint velocity. s_{f} was determined experimentally considering the range of angular velocity while the robot was moving for a given task. Since each joint of the manipulator used in the experiment rotated within an angular velocity of $5deg/s$ while implementing the peg-in-hole task, a value of s_{f} was used as 50. Fig. 2.13 shows the graph when $\boldsymbol{f}_{\text{c}}$ is 1 and s_{f} is 50.

Since each instance of joint friction renders the robot robust against the external force, joint friction compensation is compulsory. The coefficient of the friction on each joint is different. $\boldsymbol{f}_{\text{c}}$ was calculated heuristically and intuitively.

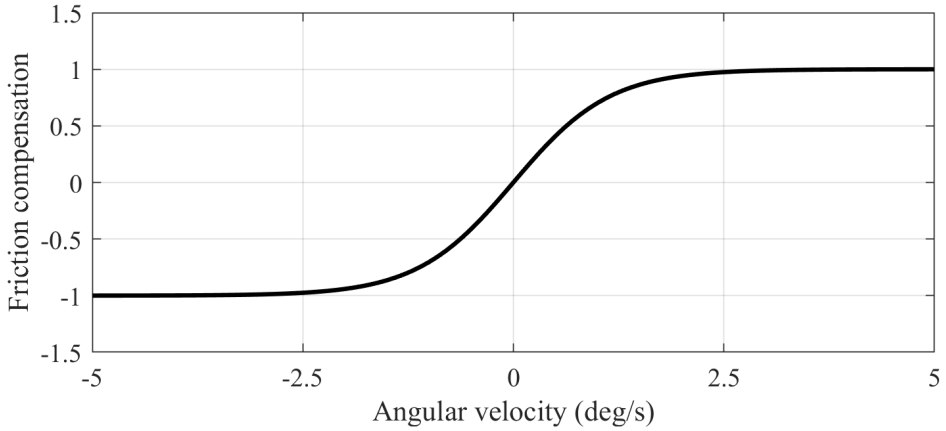

Figure 2.13: Graph of joint friction compensation.

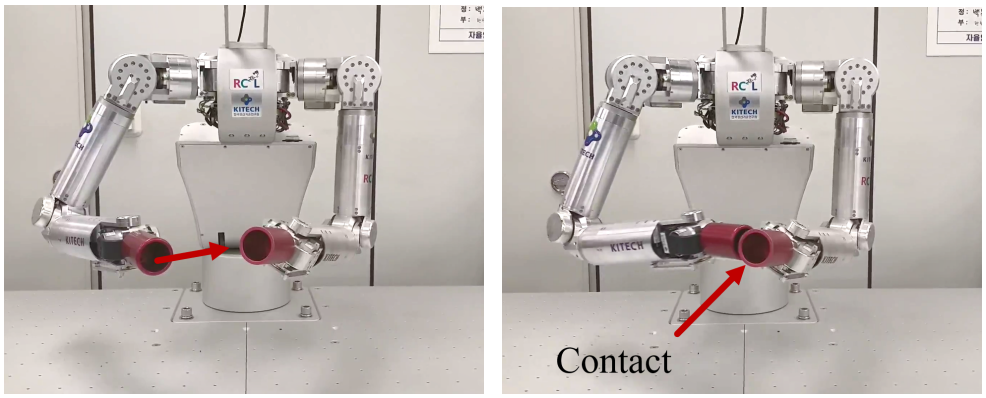

(a) (b)

(c) (d)

Figure 2.14: Friction verification: post-collision reaction experiment. (a) initial posture, (b) moment of collision, (c) After collision posture without friction compensation, and (d) After collision posture with friction compensation.

In consideration of the assembly state and gear friction of each joint of the robot, Eq. (2.6).

$$\begin{aligned} \boldsymbol{f}_{\text{c\_right}} &= \text{diag}(2.0, 4.0, 2.0, 1.0, 1.0, 1.5, 0.5, 0.5), \\ \boldsymbol{f}_{\text{c\_left}} &= \text{diag}(2.0, 2.0, 1.4, 0.7, 0.7, 0.5, 0.2, 0.2). \end{aligned} \tag{2.6}$$

Viscous friction is not considered because the actual driving range of the

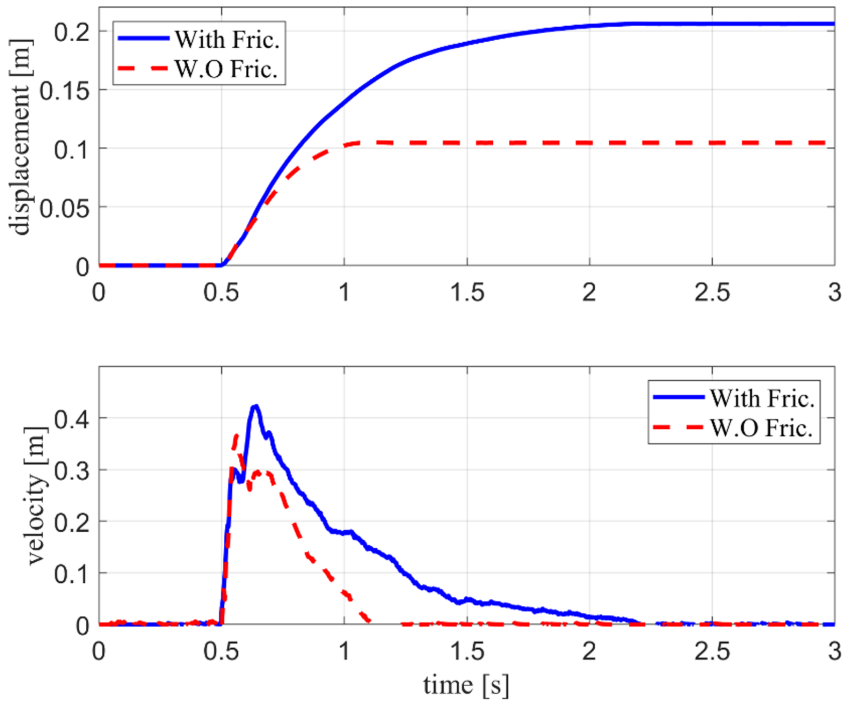

Figure 2.15: Graphs of change of displacement and velocity.

angular velocity of each joint during the peg-in-hole task was narrow.

Fig. 2.14 show an experiment snapshots to verify the effect of friction compensation. The experiment proceeded as follows. The left arm is controlled by gravity compensation or gravity compensation and friction compensation. The right arm causes a collision with the left arm through position control. The effect of friction compensation is confirmed by observing the movement of the left arm after impact. Fig. 2.14 (a) and (b) show the initial posture and moment of collision. Fig. 2.14 (c) and (d) show the post-collision reaction with and without friction compensation with gravity compensation. Fig. 2.15 show the graphs of change of displacement and velocity after collision. When friction compensation is activated, it can be clearly seen that the displacement amount

after collision is large.

2.4.3 Control Input for the Strategy

In the implementation of the proposed strategy, the robot control framework could separately generate force in the desired directions and control the position of the end effector. The sequence of combining the unit motions was accomplished by designing the wrench vector of $\begin{bmatrix} \boldsymbol{f} & \boldsymbol{m} \end{bmatrix}^{\mathrm{T}}$ as follows:

$$\begin{aligned} \boldsymbol{f} &= k_v \boldsymbol{\Omega}(\boldsymbol{p}_{\mathrm{h}} - \boldsymbol{p}_{\mathrm{p}}) + \boldsymbol{f}^* \\ \boldsymbol{m} &= \boldsymbol{K}_\omega \boldsymbol{\delta\Phi}, \quad \boldsymbol{\delta\Phi} = \boldsymbol{E}_{\mathrm{r}}(\boldsymbol{R}^* \boldsymbol{R}_{\mathrm{h}}, \boldsymbol{R}_{\mathrm{p}}), \end{aligned} \tag{2.7}$$

where $\boldsymbol{\Omega} \in \mathbb{R}^{3\times3}$ denotes the generalized task-specification matrix used to separate position control space from force control space, and $\boldsymbol{f}^*$ is the desired force and position control input. k_v is the proportional gain for the position control, $\boldsymbol{K}_\omega$ denotes the orientation control gain matrix, $\boldsymbol{K}_\omega$ expresses diag(g_{s}, g_{w}, g_{w}), g_{s} and g_{w} represent the control gains in the screwing and wiggling motions, respectively, $\boldsymbol{p}_{\mathrm{h}}$ and $\boldsymbol{p}_{\mathrm{p}} \in \mathbb{R}^{3\times1}$ are the position vectors of the hole and the peg, respectively, and $\boldsymbol{R}_{\mathrm{h}}$ and $\boldsymbol{R}_{\mathrm{p}} \in \mathbb{R}^{3\times3}$ are the rotation matrices of the hole and the peg, respectively, as shown in Fig. 2.8. Finally, $\boldsymbol{R}^*$ is the desired rotation matrix of the peg. $\boldsymbol{\delta\Phi} \in \mathbb{R}^{3\times1}$ denotes the angular rotation error vector, $\boldsymbol{E}_{\mathrm{r}}(\boldsymbol{A}, \boldsymbol{B})$, defined as a function that calculates the orientation error between the rotation matrix $\boldsymbol{A}$, and $\boldsymbol{B}$ is calculated by

$$
\begin{aligned}
&\boldsymbol{E}_{\mathrm{r}}(\boldsymbol{A},\boldsymbol{B}) = \left[\boldsymbol{a}_1 \times \boldsymbol{b}_1 + \boldsymbol{a}_2 \times \boldsymbol{b}_2 + \boldsymbol{a}_3 \times \boldsymbol{b}_3\right], \\
&\boldsymbol{A} = \left[\boldsymbol{a}_1 \quad \boldsymbol{a}_2 \quad \boldsymbol{a}_3\right],\ \boldsymbol{B} = \left[\boldsymbol{b}_1 \quad \boldsymbol{b}_2 \quad \boldsymbol{b}_3\right].
\end{aligned}
\tag{2.8}
$$

$\boldsymbol{a}_i$ and $\boldsymbol{b}_i$ denote the ith column vector of $\boldsymbol{A}$ and $\boldsymbol{B}$. From (3.12), the peg was controlled to move along the straight line passing through $\boldsymbol{p}_{\mathrm{h}}$ to the x-axis of $\boldsymbol{R}_{\mathrm{h}}$.

Since $\boldsymbol{\Omega}$ separated the space of force and position control, the peg moved in the direction of the assembly force. With the local frame of the peg and hole shown in Fig. 2.8, the generalized task-specification matrix $\boldsymbol{\Omega}$ was designed as follows:

$$
\begin{aligned}
&\boldsymbol{\Omega} = \boldsymbol{R}_h \boldsymbol{\Sigma} \boldsymbol{R}_{\mathrm{h}}^{\mathrm{T}}, \\
&\overline{\boldsymbol{\Omega}} = \boldsymbol{R}_{\mathrm{h}} \overline{\boldsymbol{\Sigma}} \boldsymbol{R}_{\mathrm{h}}^{\mathrm{T}}, \quad \overline{\boldsymbol{\Sigma}} = \boldsymbol{I} - \boldsymbol{\Sigma},
\end{aligned}
\tag{2.9}
$$

where $\boldsymbol{\Sigma} \in \mathbb{R}^{3\times3}$ denotes the force specification matrix. In case the local frame of the hole was attached as shown in Fig. 2.8, the force was generated in the direction of the x-axis of the hole frame and the peg was controlled along the y-z plain of the hole frame. Hence, the force specification matrix, $\boldsymbol{\Sigma}$, was set by $\mathrm{diag}(0,1,1)$ in this coordinate configuration.

Control inputs $\boldsymbol{f}^*$ and $\boldsymbol{R}^*$ are defined as the sum of $\boldsymbol{f}_i$ and the inner product of $\boldsymbol{R}_i$, respectively. Here, $\boldsymbol{f}_i$ and $\boldsymbol{R}_i (i = a, b, c, d)$ denote control inputs for achieving each type of unit motion: pushing, rubbing, wiggling, and screwing.

For example, in the case of the approach and searching steps, $\boldsymbol{f}^*$ and $\boldsymbol{R}^*$ are expressed as

$$\begin{aligned} \boldsymbol{f}^*_{\mathrm{reach}} &= \boldsymbol{f}_{\mathrm{a}}, \qquad \boldsymbol{R}^*_{\mathrm{reach}} = \boldsymbol{R}_{\mathrm{a}}, \\ \boldsymbol{f}^*_{\mathrm{search}} &= \boldsymbol{f}_{\mathrm{a}} + \boldsymbol{f}_{\mathrm{b}}, \ \boldsymbol{R}^*_{\mathrm{search}} = \boldsymbol{R}_{\mathrm{a}}\boldsymbol{R}_{\mathrm{b}}, \end{aligned} \tag{2.10}$$

and the control input of the inserting step is expressed by

$$\begin{aligned} \boldsymbol{f}^*_{\mathrm{insert}} &= \boldsymbol{f}_{\mathrm{a}} + \boldsymbol{f}_{\mathrm{c}} + \boldsymbol{f}_{\mathrm{d}}, \\ \boldsymbol{R}^*_{\mathrm{insert}} &= \boldsymbol{R}_{\mathrm{a}}\boldsymbol{R}_{\mathrm{c}}\boldsymbol{R}_{\mathrm{d}}. \end{aligned} \tag{2.11}$$

The components of control input $\boldsymbol{f}_i$ and $\boldsymbol{R}_i$ are expressed as follows:

$$\begin{aligned} \boldsymbol{f}_{\mathrm{a}} &= \overline{\boldsymbol{\Omega}}\boldsymbol{R}_{\mathrm{h}} \begin{bmatrix} f & 0 & 0 \end{bmatrix}^{\mathrm{T}}, \\ \boldsymbol{f}_{\mathrm{b}} &= k_v \boldsymbol{\Omega}\boldsymbol{R}_{\mathrm{h}} \begin{bmatrix} 0 & r\sin\theta & r\cos\theta \end{bmatrix}^{\mathrm{T}}, \\ \boldsymbol{f}_{\mathrm{c}} &= \boldsymbol{f}_{\mathrm{d}} = \begin{bmatrix} 0 & 0 & 0 \end{bmatrix}^{\mathrm{T}}, \end{aligned} \tag{2.12}$$

$$\begin{aligned} &\boldsymbol{R}_{\mathrm{a}} = \boldsymbol{R}_{\mathrm{b}} = \boldsymbol{I}, \\ &\boldsymbol{R}_{\mathrm{c}} = \boldsymbol{R}_{\mathrm{y}}(\beta)\boldsymbol{R}_{\mathrm{z}}(\gamma), \quad \beta = k_{\mathrm{w}}\sin\phi, \ \ \gamma = k_{\mathrm{w}}\cos\phi, \\ &\boldsymbol{R}_{\mathrm{d}} = \boldsymbol{R}_{\mathrm{x}}(\alpha), \qquad \alpha = k_{\mathrm{s}}\sin\phi. \end{aligned} \tag{2.13}$$

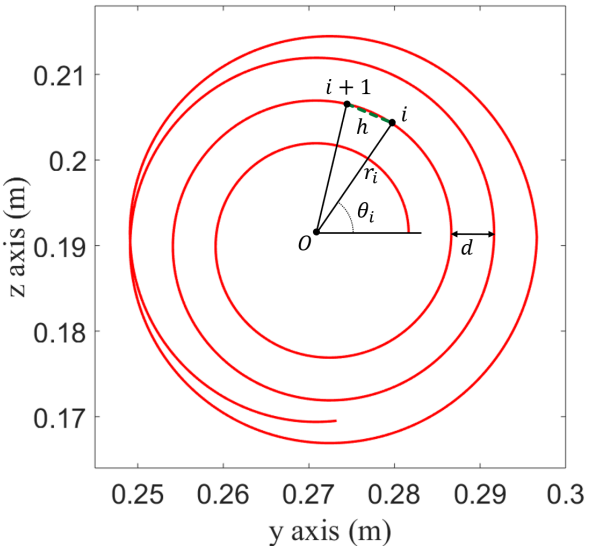

Figure 2.16: Spiral trajectory.

The insertion force f was separated from the position control for the hole search by the task-specification matrix $\overline{\mathbf{\Omega}}$. r and θ denote the distance and angle in polar coordinates, and spiral motion was generated by changing these in the yz-plane of $\boldsymbol{R}_{\mathrm{h}}$. $\boldsymbol{R}_{\mathrm{x}}(\alpha)$, $\boldsymbol{R}_{\mathrm{y}}(\beta)$, and $\boldsymbol{R}_{\mathrm{z}}(\gamma)$ represent rotation matrices about the x, y, and z axes with α, β, and γ degrees, respectively. The wiggling and screwing motions were generated by increasing ϕ, and the amplitudes of these motions was determined by wiggling rotation gain k_{w} and screw rotation gain k_{s}. In order to generate the spiral motions, r and θ in f_{b} in (2.12) were determined by Archimedes' spiral trajectory:

$$\begin{aligned} \theta_{i+1} &= \theta_i + \delta\theta, \quad \delta\theta = \tan^{-1}(\frac{h}{r_i}), \\ r_{i+1} &= r_i + (\theta_{i+1} - \theta_i)\frac{d}{2\pi}, \end{aligned} \tag{2.14}$$

where d denotes the distance between the next and previous desired positions. Δr denotes the radius increment as shown in Fig. 2.16. The maximum radius of the spiral is experimentally determined to within twice the maximum position error. The other parameters of the trajectory are decided by considering the control frequency and search speed.

2.5 Experiment

2.5.1 Experiment Environment

In order to verify the effectiveness of the proposed method, peg-in-hole experiments were implemented with a real robot. In the experiment, a humanoid upper body robot developed by the Robotics R&D Group of the Korea Institute of Industrial Technology was used. The robot consist of dual eight-DOF

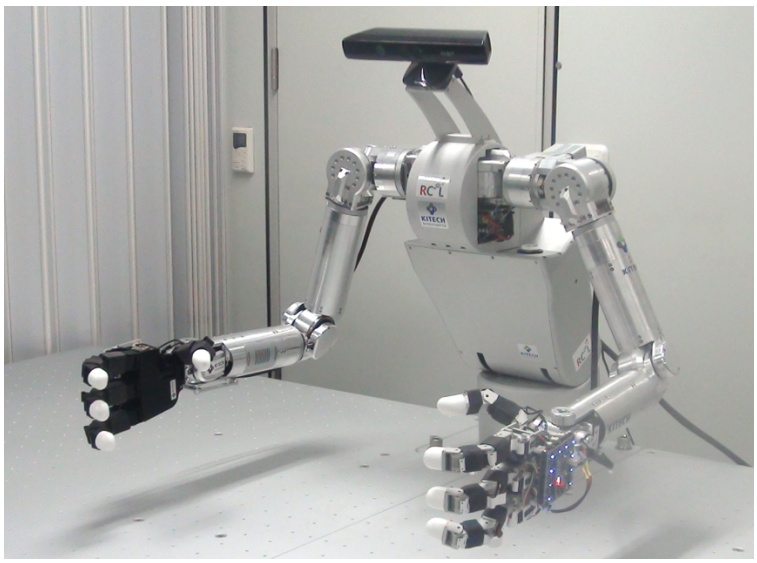

Figure 2.17: KITECH upper body robot.

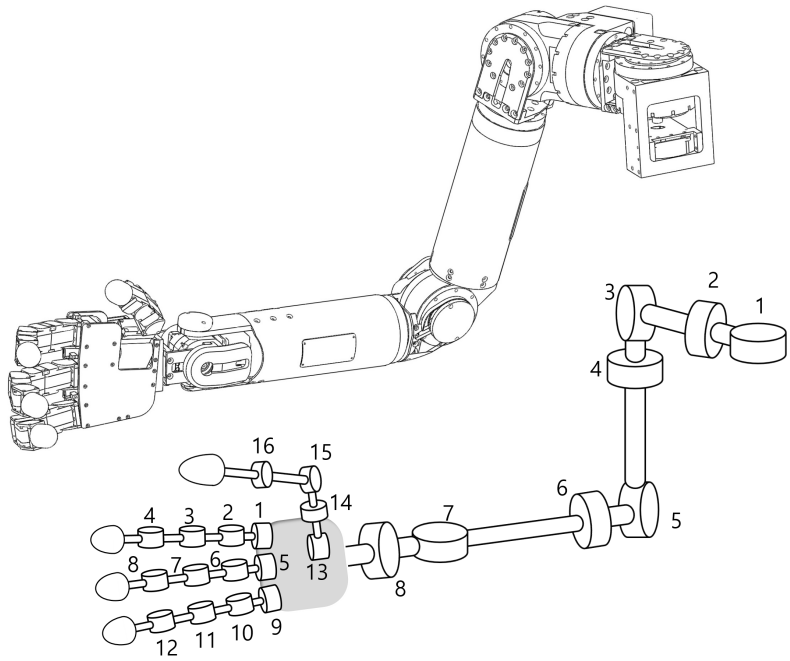

Figure 2.18: Joint arrangement of KITECH arm and hand.

arms, two-DOF wrist, and couple of multifinger hand with four fingers of four joints. All gears in the joint are used as Harmonic with a gear ratio of 100: 1. The robot receives torque input for each joint. Fig 2.17 shows the humanoid upper body robot used in experiment.

Fig. 2.18 shows the arm and hand joint arrangement. The hand and arm exchange information only for gravity compensation with each other and are controlled independently. The fingers of the hand are numbered in the order of the index finger, middle finger, ring finger, and thumb.

2.5.2 Fixed Peg and Fixed Hole

Fig. 2.19 shows experiment environment. The experiments were conducted using the left arm of the robot. Kinect was installed on its head to recognize the position and orientation of the hole. The peg is installed on the tip of the manipulator and the hole is installed at an arbitrary location within the workspace of the manipulator. The diameter of the peg was 50.00 mm, and the clearance between the peg and hole was 0.01 mm. The peg and the hole were chamferless. The position and orientation of the hole were approximated using Kinect with Canny edge detection and the Hough transform algorithm.

Table 2.1: Parameters used in the experiment.

Parameter	Value
f [N]	7.5
k_v	300
$\boldsymbol{K}_w$	diag(5.0, 3.0, 3.0)
$\boldsymbol{f}_\mathrm{c}$	diag(2.0, 2.0, 1.4, 0.7, 0.7, 0.5, 0.2, 0.2)

Since it is necessary to prove whether the proposed strategy is valid for peg-in-hole assembly and overcome uncertainty, the position value of the hole is obtained using a low-cost vision sensor. Fig. 2.20 show the process of hole recognition by Kinect. The standard deviation of the position and orientation value obtained by extraction 1000 data was $1.4mm$ and $2.65deg$, respectively.

2.5.2.1 Experiment Results

Fig. 2.21 shows snapshots taken during the experiment. Fig. 2.22-Fig. 2.24 shows the desired and actually calculated positions and orientations of the peg

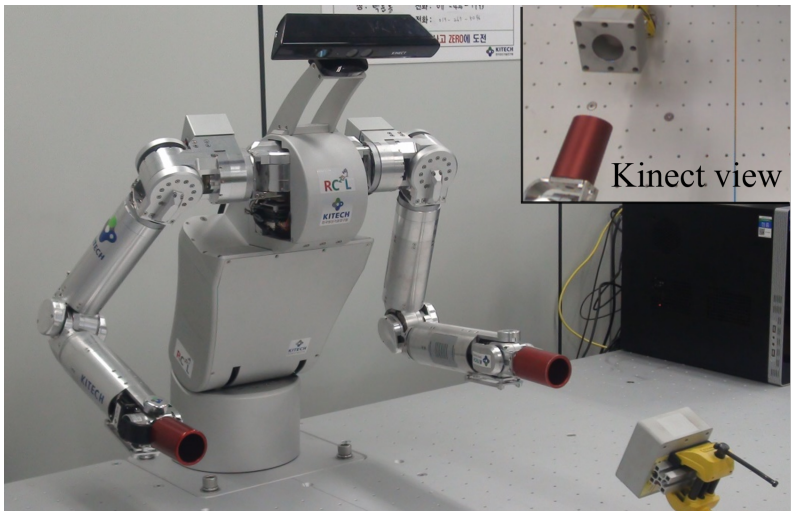

Figure 2.19: Experimental environment.

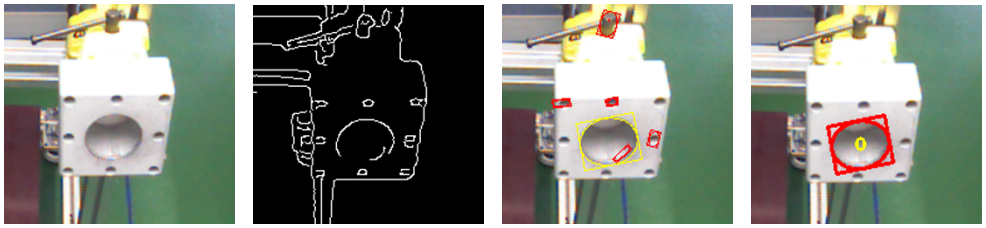

(a) (b) (c) (d)

Figure 2.20: Recognition of the hole using Kinect: (a) original image; (b) edge detection; (c) circle detection; (d) hole extraction.

during steps of the peg-in-hole task carried out according to the proposed strategy. All graphs are expressed with respect to the local frame of the hole. The graphs that took the most time (12 s) were chosen because the rubbing and wiggling motions were not clearly seen in most cases due to the too-rapid transition between steps. Fig. 2.22 shows the trajectory of the peg during the peg-in-hole experiment in Cartesian space. Figs. 2.23 and Figs. 2.24 show the position and rotation of the peg throughout the peg-in-hole procedure.

Fig. 2.23 shows the graphs of the velocity of the peg along the x, y, and z

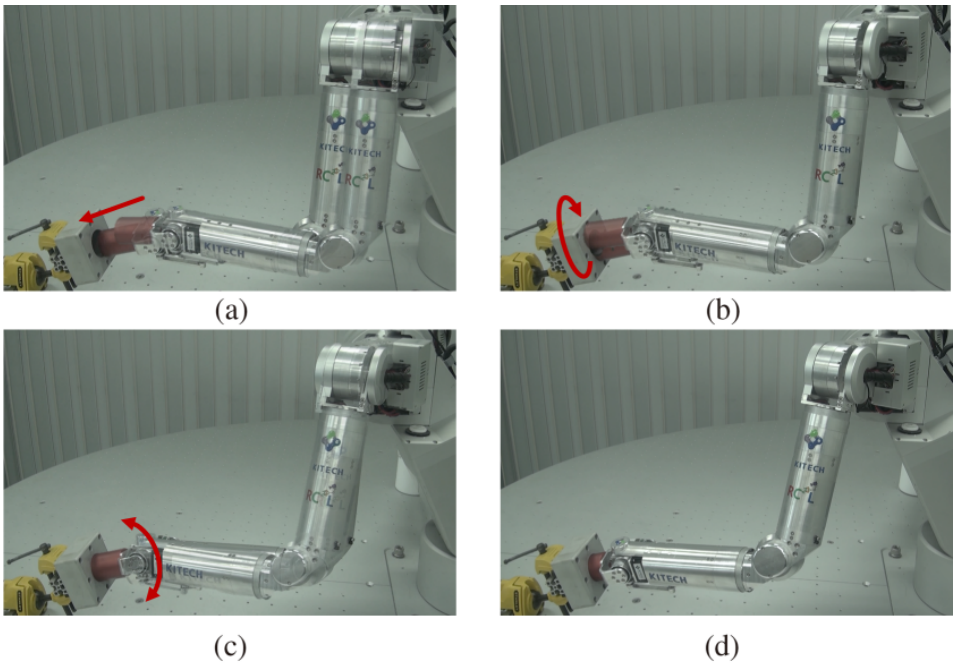

Figure 2.21: Snapshots of the peg-in-hole assembly: (a) approaching; (b) reaching; (c) finding the hole; (d) insertion.

axes, respectively. When the peg-in-hole task begins with the reaching step, the approach of the peg is blocked by the hole by contact. In Fig. 2.23, the second graph shows the change of the position of the peg in the approach direction. The peg is stopped by contact at 1.2 s, and the velocity of the peg converges to nearly 0 m/s. The end of the approach process is detected by observing the velocity of the peg, and the state is automatically passed to the searching step.

The velocity of the peg is ideally zero during stopping. However, the velocity calculated from forward kinematics information includes some error caused by fluctuations of joint encoder values. In an actual peg-in-hole task environment, the condition for detecting contact is a change to (2.15) with the experimentally deduced threshold v_t (0.02 is used in this experiment).

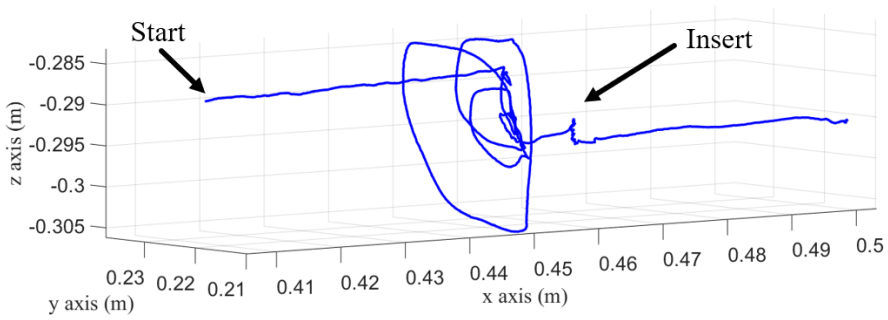

Figure 2.22: Experimental results of the peg-in-hole procedure: trajectory of the peg.

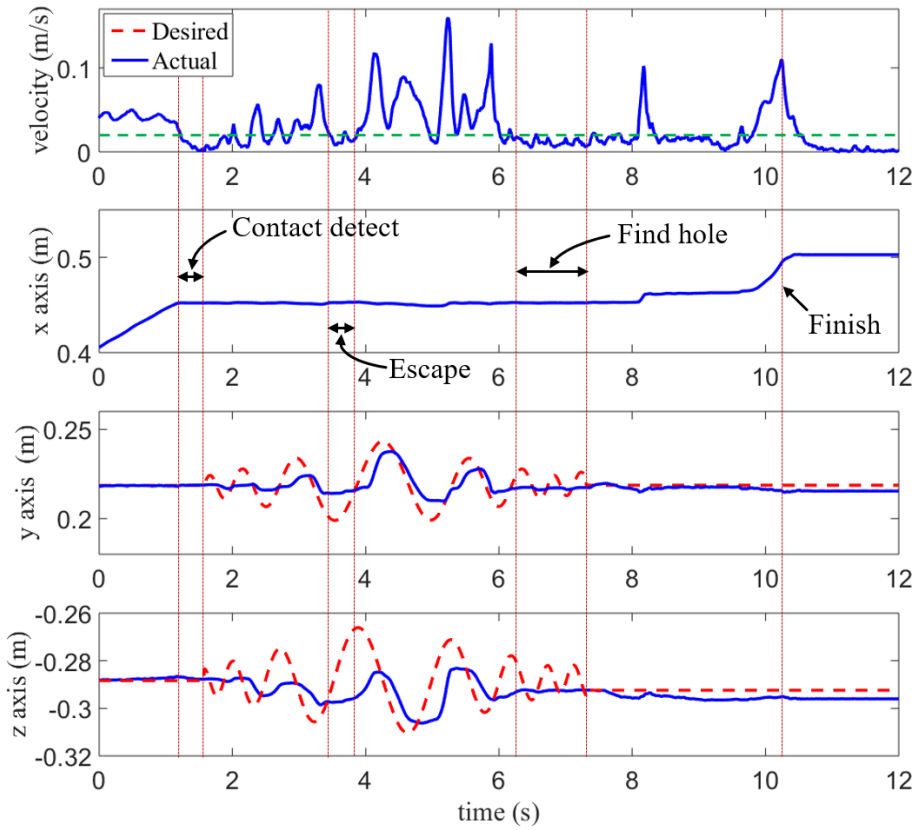

Figure 2.23: Experimental results of the peg-in-hole procedure : translations of desired and actual trajectories.

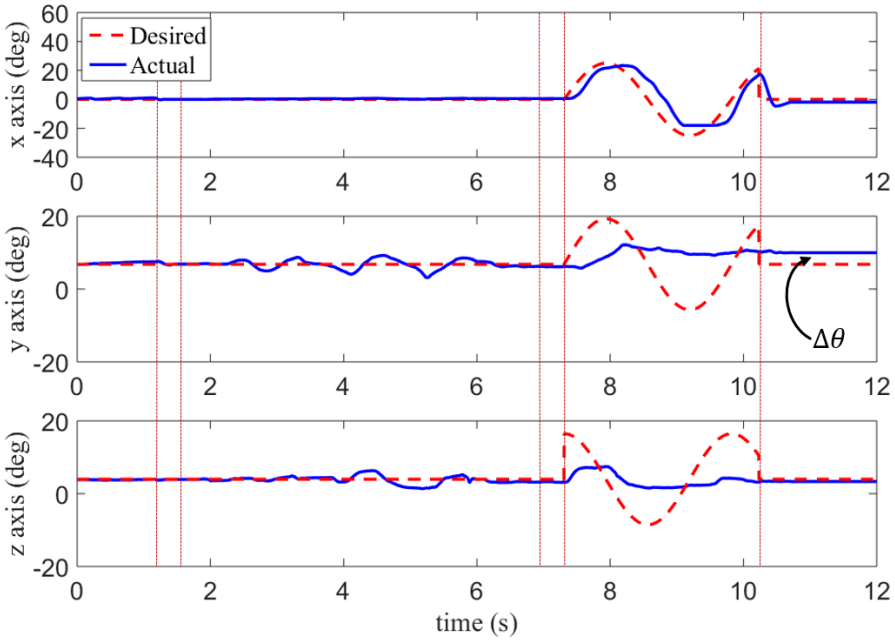

Figure 2.24: Experimental results of the peg-in-hole procedure: orientations of desired and actual trajectories.

$$\dot{\boldsymbol{p}}_{\mathrm{p}} < v_{\mathrm{t}} \quad \text{during} \quad 0.3\mathrm{s} \tag{2.15}$$

In the third and fourth graphs of Fig. 2.23, the spiral search motion was generated after 1.8 s. Due to the applied frictional force, the peg moved by roughly drawing a spiral. At 3.5 s in Fig. 2.23, the velocity of the peg temporarily decreased to 0 m/s. In this case, the state of the peg is shown in Fig. 2.10. However, the hole was temporarily found, and the peg passed by the hole and following the desired trajectory was attempted. This is explained by the fact that the position control input f^* was sufficiently larger than the assembly force f shown in Fig. 2.10(b). Starting at 6.5 s in Fig. 2.23, although the desired spiral

trajectory was still being generated, the peg could not move because its tip was caught at the hole entrance. The end of the search process was also detected by (2.15).

In Fig. 2.24, the rotation of the peg changed with the tilting motion when the hole was found by the spiral movement of the peg due to the compliant behavior of the robot's arm. Once the hole search was complete at 7.5 s, inserting movements with unit motions of pushing, wiggling, and screwing were activated. Once the peg was inserted into the hole, the mismatch between the desired and actual positions was expressed as the recognition error. The completion of the peg-in-hole assembly was detected by comparing the hole location recognized by the sensor and the given peg position.

For the improved validation in various experimental conditions, experiments with smaller pegs/holes were conducted (20mm and 10 mm). As shown in Fig. 2.26(a),(b), the size of peg and hole is much smaller than ones of previous experiment (50mm), but the same method was applied for the experiments.

Figs. fig:graphs2010b(c),(d) and fig:graphs2010b shows the spatial and time domain trajectories of the peg while the experiments. As shown in the results, the proposed method was equally effective for various sized pegs.

2.5.2.2 Analysis of Force and Control Gain

When the hole was found by the rubbing motion, the balance of suitable ratio between the assembly force and the spiral motion control gain was important to prevent the peg from escaping from the hole. In order to find a suitable scale for the force and the position control gain, the experiment was implemented

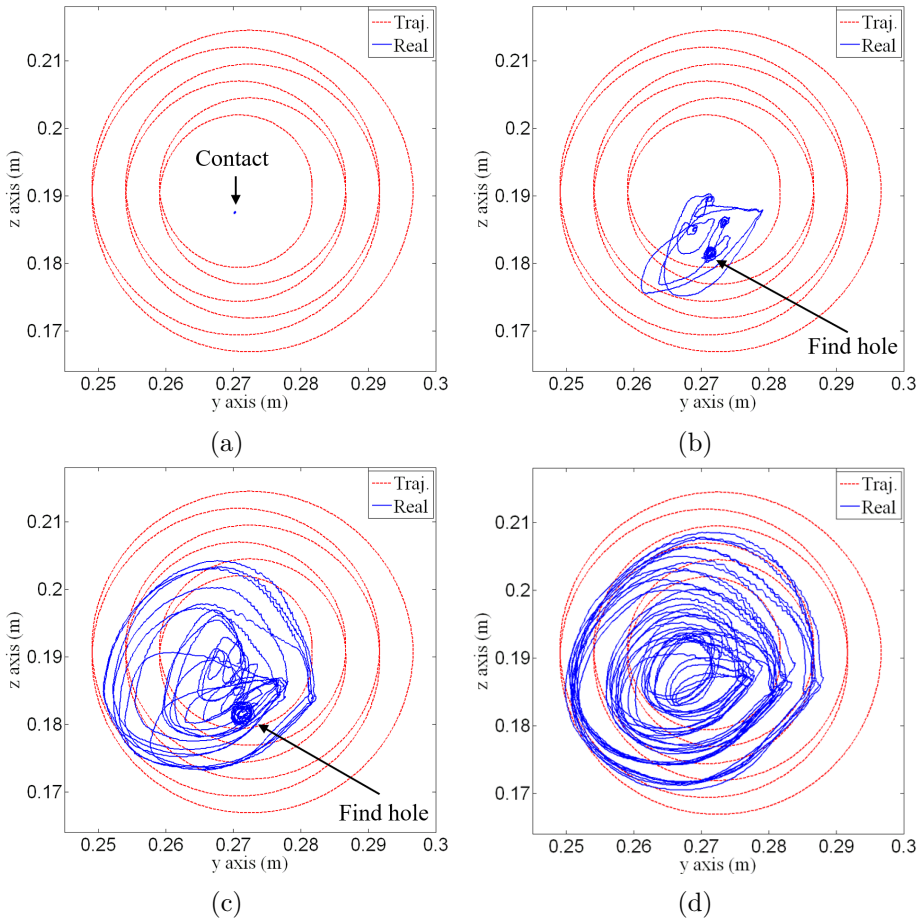

Figure 2.25: Desired and actual trajectories of the peg in local coordinates of the hole when f was fixed at 7.5. (a) $k_v = 100$, (b) $k_v = 300$, (c) $k_v = 500$, and (d) $k_v = 700$.

by various assembly force values of f and position control gain k_v expressed in (2.12).

Fig. 2.25 shows the trajectories of the position of the peg during spiral motion in a state of contact. All graphs are shown in the xy-plain in the local frame of the hole. In all cases, f was set to 7.5 N, and the values of k_v were 100, 300, 500, and 700, respectively.

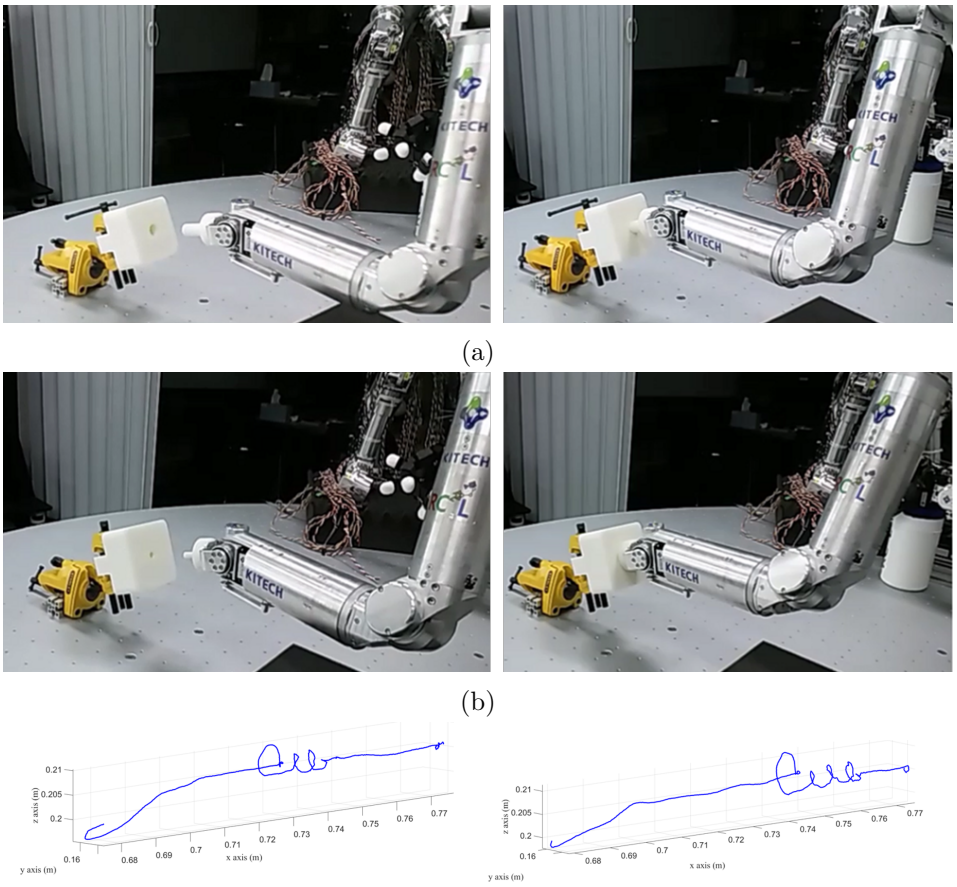

Figure 2.26: Experimental scens of (a) $20mm$ and (b) $10mm$ peg-in-hole assembly; spatial trajectory of the peg when peg diameter is (c) $20mm$ (d) $10mm$.

While the location of the hole obtained by Kinect was [0.271 0.190], the location of the hole found by the proposed strategy was [0.272 0.182]. In Fig. 2.25(a), the peg cannot move at the first contact point due to friction. This phenomenon occurred because the ratio of k_v to f was too small to overcome the friction force. In Fig. 2.25(d), the trajectory of the peg roughly exhibits spiral motion; however, the location of the hole could not be found because of the high value of k_v. In case of graphs (b) and (c) in Fig. 2.25, the hole was found. The average time taken to find the hole in case k_v was 300 and 500 was

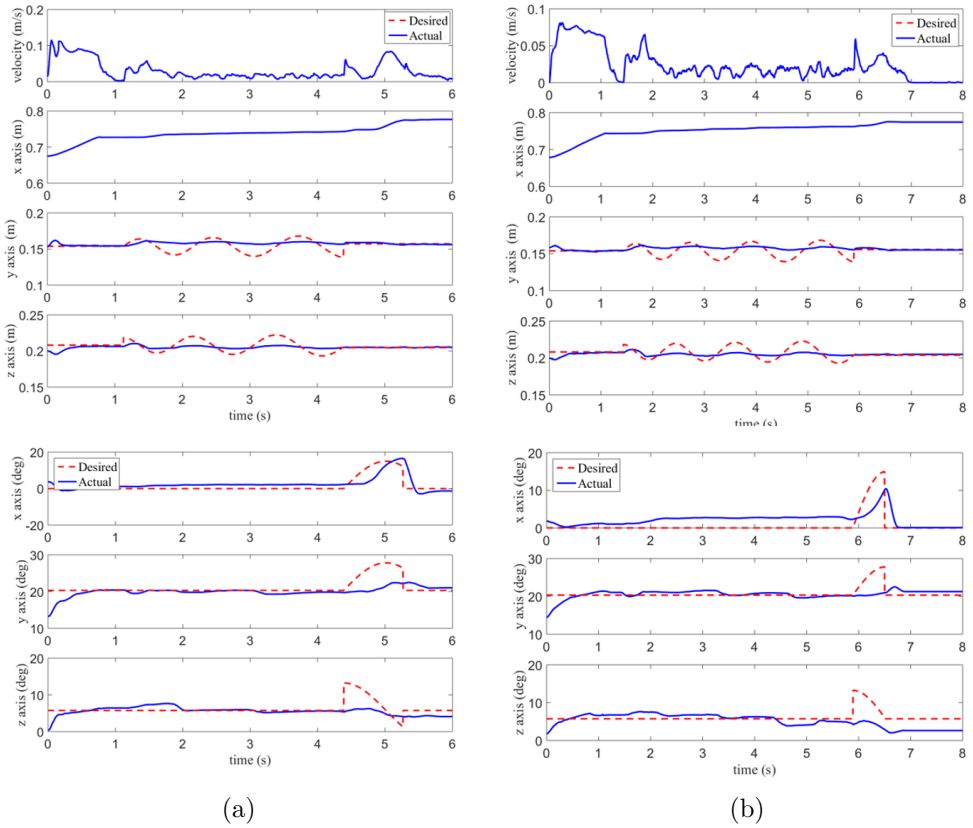

(a) (b)

Figure 2.27: Velocity magnitude, position and orientation of peg when peg diameter is (a) 20 mm and (b) 10 mm.

4.58 s and 19.23 s, respectively.

From the graphs, if the value of k_v was too low, the peg could not move. A suitable low value of k_v made the peg-in-hole task faster. By contrast, a high value of k_v made the peg roughly follow the trajectory. However, the robot lost the compliance characteristic. In order to prevent breaking the assembly objects or the robot, setting a low value of f is desirable. In order to find suitable values of f and k_v, the performance factor f_p was designed to evaluate the effect of the magnitude of the force and position gain on the rate of success and time to achieve success as in (2.16).

$$f_p = \frac{n_s}{t_a} \tag{2.16}$$

where n_s and t_a denote the number of successes and average success time, respectively. If the number of successes was high or success time was low, f_p was high. The experiment was conducted as follows: the peg approached the detected location of the hole with some error. When contact occurred, the velocity of the peg became zero. Then, the robot started to rub the peg near the hole using the proposed search motion with various values of assembly forces f and k_v. When the location of the hole was found, the velocity of the peg became zero. t_a was calculated by averaging the time spent between the two points where the velocity of the peg was zero.

In Fig. 2.28, the measured values of f_p is dotted in case f was set to 5, 7.5, and 10, and k_v was changed to 100, 150, and 600, respectively. In all cases of f, f_p is expressed by zero in case k_v was lower than 100 or higher than 650. Continuous relations between f_p and f, k_v were estimated using Gaussian curve fitting, expressed by (2.17):

$$f_p' = \mathrm{a}e^{-((k_v-\mathrm{b})/\mathrm{c})^2}. \tag{2.17}$$

Each estimated performance factor f_p' is shown in Fig. 2.28. Each of the a, b, and c of (2.17) is listed in Table 2.2. b means k_v when f_p' was expected to be at its highest value. From these results, it seemed that f and b were similarly

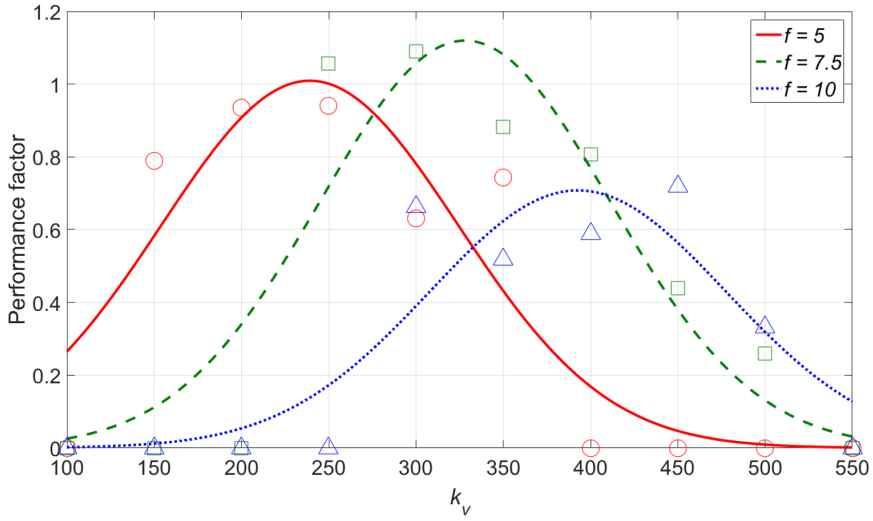

Figure 2.28: Gaussian curve-fitting graph of the relationship between performance factors and position control gains for a fixed assembly force.

in a proportional relationship in case of various values of f. In order to decide a suitable assembly force and task control gain, f was first chosen considering the material of the object of assembly to prevent breakdown, and the value of k_v was decided using proportional relationships.

Table 2.2: Coefficients of Gaussian fitting.

f	a	b	c	f/b
5	1.009	239.2	120.3	0.021
7.5	1.12	328.1	117.3	0.023
10	0.7079	392.7	120.1	0.025

2.5.3 Peg-in-Hole with Multi Finger Hand

Assembling the grasped object using the hand is more complicated than the experiment shown in the previous subsection because the kinematic estimation

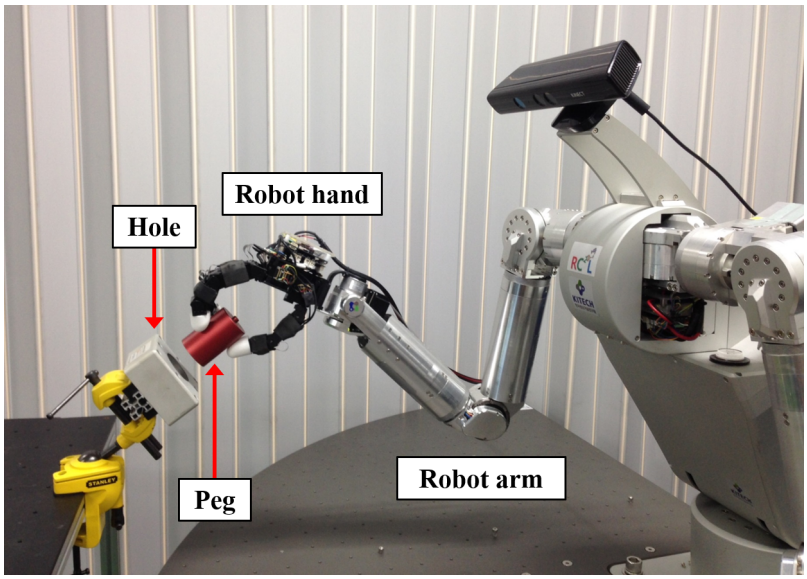

Figure 2.29: Experiment environment with anthropomorphic hand.

error of the grasped object must also be considered with the information error about the hole. In this subsection, I show the effectiveness of the strategy by grasping the peg placed in the external environment using anthropomorphic hand and implementing the peg-in-hole experiment[34]. Fig. 2.29 shows the experiment environment. The peg is gripped using multi-finger hand and assembled by hand and arm cooperation.

2.5.3.1 Object Grasping

For a robot to grasp an object with multiple fingers cooperatively, internal forces have been mainly considered[35]. A virtual linkage model was presented to characterize internal forces and moments that act during manipulation of grasp with multiple manipulator[36]. Internal force-based impedance control was adopted to determine the relationship between the velocity of each manipulator and the

internal force on the objects[37].

Object-level grasp controllers have been proposed to manipulate an object intuitively[38]-[40]. The object-level controller realizes object motion by determining the corresponding object impedance that generates the force driving the object frame to the desired object frame[41].

Wimböck presented a method for translating and rotating a ball while holding it with four fingertips contacts[42]. To achieve this, a virtual object frame is defined geometrically by the positions of the fingertips. In addition, object level control law is addressed passivity based impedance controller. Cole presented a method for manipulating objects of arbitrary shape by a multifingered hand[43]. The kinematics of rolling contact for two surfaces was derived, and simulations were performed to demonstrate the effectiveness of the control scheme. Sapio presented an approach to formulate task-level motion control for holonomically constrained multibody systems based on mass-weighted orthogonal decomposition[44].

In this paper, "Blind Grasp" method is used to grasp an object[45]-[49].

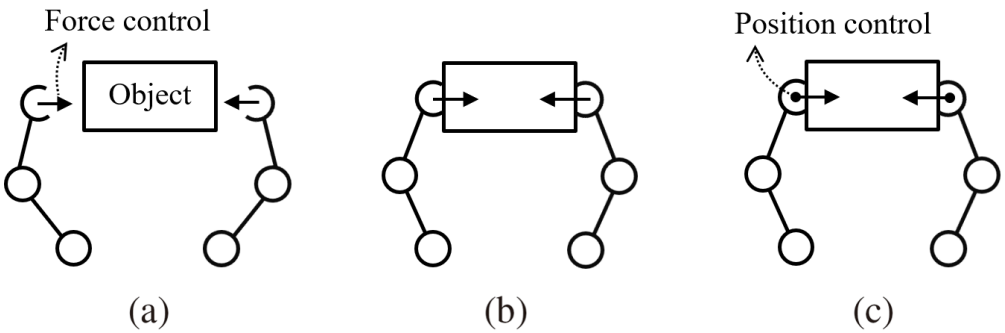

Figure 2.30: Grasp scheme: (a) initial posture; (b) grasping the object; (c) force-position control.

"Blind Grasp" is the strategy of manipulating an object when the grasping force for holding an object is generated from each fingertip to the center of the object, and the position of each fingertip is controlled by passivity-based impedance controller in the Cartesian space simultaneously. In order to manipulate the grasped object, an additional external force is generated by each fingertip. Most approaches adopted to manipulate a grasped object is based on hybrid force/position control to control the position of the fingertip and generate the grasp force.

In this paper, the object grasping and manipulating method used in this paper is inspired from "Blind Grasp". Fig. 2.30 shows how to grasp the object. First, a constant grasping force is generated towards the opposite fingertips. When contact with an object occurs and the object is grasped, the current position of each fingertip is recorded. Finally, with the generation of the grasping force, the position control of each fingertip is activated to the recorded position. Basically, object grasping is achieved by this approach. When grasping an object using three or four fingers,

2.5.3.2 Object In-Hand Manipulation

Fig. 2.31(a) shows a triangle defined when holding an object with three fingers. In this paper, this triangle is defined as a virtual triangle, and the center of the triangle is regarded as the center of the object. Fig. 2.31(a) shows the force created to hold the object. Considering thumb opposability, the fingers except the thumb generate the force in the direction of the thumb, and the thumb creates a force such that the sum of all grasping forces is zero. Fig. 2.31(b) depicts the decomposition of the grasping force. The grasping force

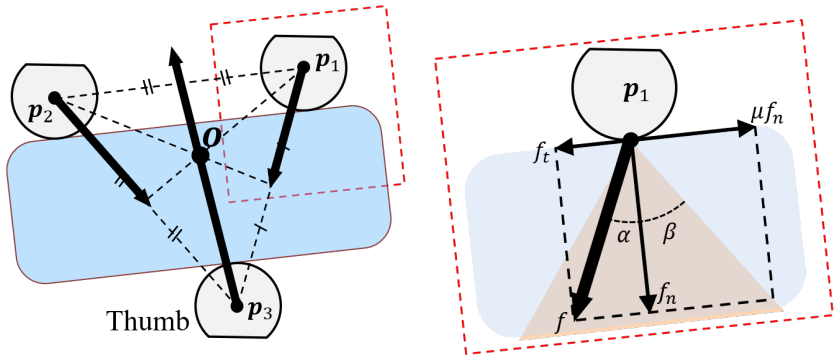

(a) (b)

Figure 2.31: (a) Virtual triangle formed by three fingertips and grasping force considering thumb opposability; (b) grasping force decomposition.

is decomposed into vertical and horizontal components with respect to the contact point, and only the vertical component acts as the grasping force. As the horizontal component of the grasping force is generated smaller than the frictional force caused by the vertical component force, the hand stably grips the object without slipping.

Fig. 2.32(a) shows a virtual triangle defined when the actual hand holds the object. Each finger of the hand is controlled by position and force generation in the operational space, and orientation of the fingertip is not controlled. The controller of each finger is as

$$\begin{aligned} \boldsymbol{\tau} &= \boldsymbol{J}^{\mathrm{T}} \boldsymbol{f}^{*} + \boldsymbol{f}_{\mathrm{grasp}} + \boldsymbol{\tau}_{\mathrm{g}} + \boldsymbol{\tau}_{\mathrm{fric}} + \boldsymbol{q}^{*}, \\ \boldsymbol{f}^{*} &= \boldsymbol{K}_{\mathrm{p}}(\boldsymbol{p}_t - \boldsymbol{p}_c), \\ \boldsymbol{q}^{*} &= \boldsymbol{K}_{\mathrm{t}}(\boldsymbol{q}_d - \boldsymbol{q}_c). \end{aligned} \tag{2.18}$$

$\boldsymbol{J}$, $\boldsymbol{f}_{\mathrm{grasp}}$, $\boldsymbol{\tau}_{\mathrm{g}}$, and $\boldsymbol{\tau}_{\mathrm{fric}}$ denote Jacobian matrix, grasping force vector, grav-

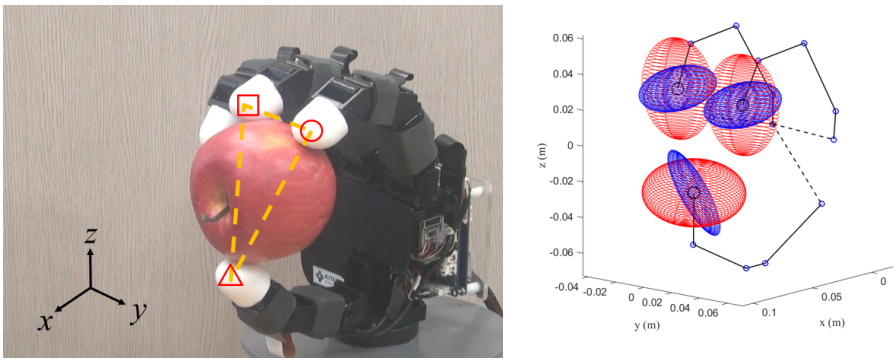

(a) (b)

Figure 2.32: (a) Virtual triangle formed by index, middle, and thumb fingers; (b) manipulability ellipsoid of each finger.

ity compensation torque, and friction-compensated torque, respectively. The redundancy of the hand is solved by adding $\boldsymbol{q}^*$. $\boldsymbol{K}_\mathrm{t}$ is the diagonal torsional spring gain matrix[32]. $\boldsymbol{q}_d$ and $\boldsymbol{q}_c$ denote the constant joint configuration for manipulability efficiency and current joint angle, respectively. Since $\boldsymbol{q}^*$ disturbs the grasp and manipulation task caused by full ranked $\boldsymbol{K}_\mathrm{t}$ obviously has DOF of the finger and total task is over the DOF of the system, in this experiment, $\boldsymbol{K}_\mathrm{t}$ was designed to have only one rank.

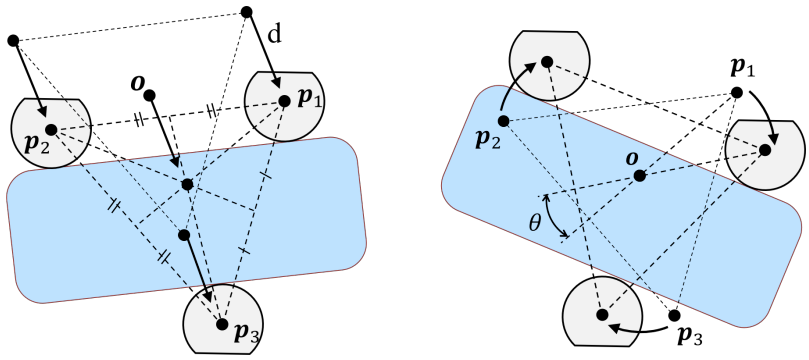

Figure 2.33: Object translation and rotation.

Fig. 2.33 shows a diagram of an in-hand manipulation of an object. The

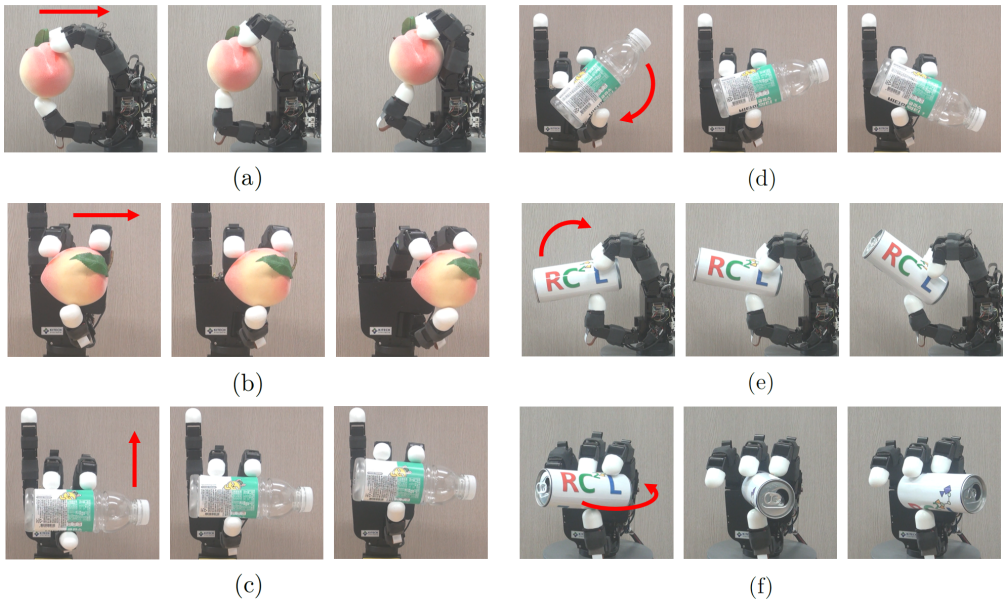

Figure 2.34: Snapshots of object in-hand manipulation: (a) translate in x-axis, (b) translate in y-axis, (c) translate in z-axis, (d) rotate in x-axis, (e) rotate in y-axis, and (f) rotate in z-axis.

translation and rotation of the object in the hand is realized by translating and rotating the virtual triangle. The center of the triangle and the center of the object are definitely different, but this inaccuracy is overcome through the proposed assembly strategy.

The expression of object in-hand manipulation is as

$$\boldsymbol{p}_{\mathrm{t}} = \boldsymbol{R}_{\mathrm{d}}(\boldsymbol{p}_{\mathrm{i}} - \boldsymbol{o}_{\mathrm{i}}) + \boldsymbol{o}_{\mathrm{i}} + \boldsymbol{p}_{\mathrm{d}}. \tag{2.19}$$

$\boldsymbol{p}_{\mathrm{t}}$ and $\boldsymbol{p}_{\mathrm{i}}$ indicate the desired position and initial position of each fingertip. $\boldsymbol{o}_{\mathrm{i}}$ denotes the initial position of virtual triangle. $\boldsymbol{R}_{\mathrm{d}}$ and $\boldsymbol{p}_{\mathrm{d}}$ represent the target

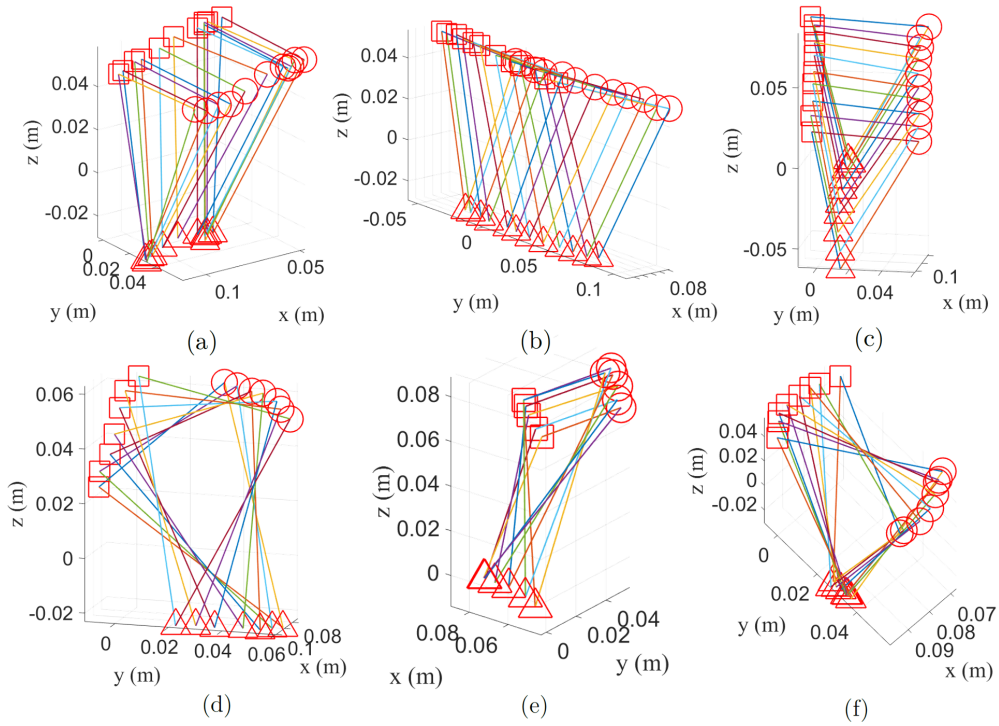

Figure 2.35: Graphs of object in-hand manipulation: (a) translate in x-axis, (b) translate in y-axis, (c) translate in z-axis, (d) rotate in x-axis, (d) rotate in y-axis, and (d) rotate in z-axis.

rotation matrix to rotate and the vector to translate compared to the initial posture. Fig. 2.32(b) shows the manipulability ellipsoid defined at each fingertip when the KITECH hand grasps the object. Since the manipulability ellipsoid of each finger is different for each configuration, different control responses are different depending on the input by the same $\boldsymbol{R}_{\mathrm{d}}$ and $\boldsymbol{p}_{\mathrm{d}}$. However, by using a low control gain, the instability can be reduced by adapting each fingertip to the object surface.

Fig. 2.34 shows snapshots of the experimental results of in-hand manipulating the grasped object using the KITECH anthropomorphic hand. Fig. 2.35 graphically show the location of each finger tip during in-hand manipulation of

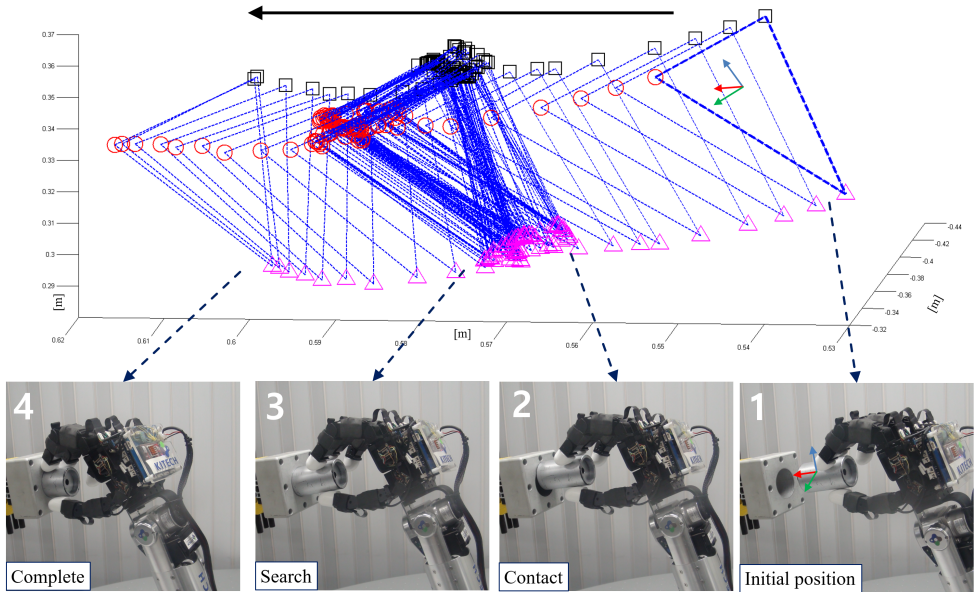

Figure 2.36: Peg-in-hole assembly with hand-arm coordinate.

the object.

2.5.3.3 Experiment Results

Fig. 2.36 shows the peg-in hole assembly experiment with the hand arm system. In the assembly process, the trajectory of the three fingertips grasping the peg was graphed, and the process of searching the hole is clearly revealed. The effectiveness of the proposed peg-in-hole strategy was proved by successfully carrying out the peg-in-hole experiment involving the kinematic estimation error of the grasped object.

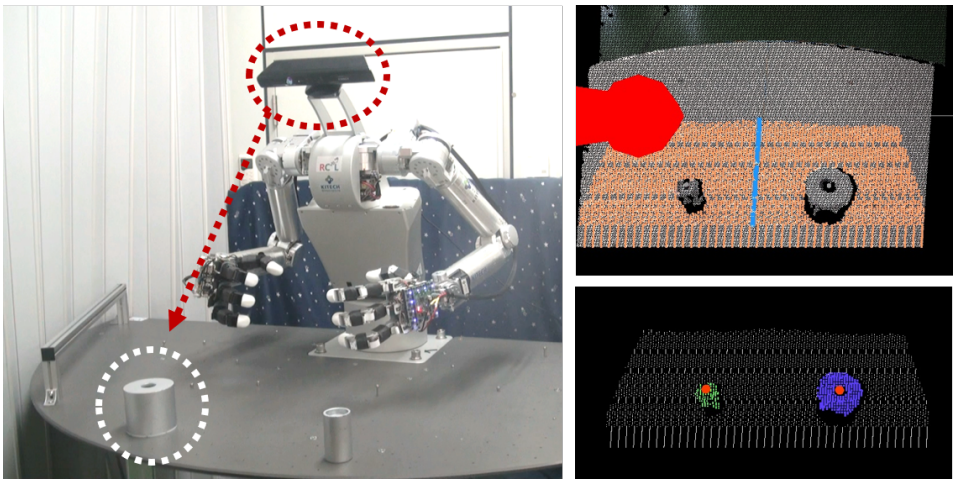

Figure 2.37: Recognition of hole and peg on the floor; the position of hole and peg are extracted by Kinect, the standard deviation of the hole and peg position are $1.3mm$ and $0.91mm$, respectively.

2.5.4 With Upper Body Robot

The anthropomorphic hand can exert great advantages in the assembly of objects. Assembly work is usually done through an exclusive gripper made for the specific object. The anthropomorphic hand can be used to replace various exclusive grippers because it can hold various objects. In this paper, I present the performing peg-in-hole task which is a typical assembly work using the anthropomorphic hand.

The peg-in-hole assembly proceeds as follows. The peg and hole are placed on the table, and information about the location is given roughly. The anthropomorphic hand has a left-handed and right-handed structure that includes the concept of a thumb. The hand consists of four fingers of four active joints and these are attached to two robotic arms, respectively. The two hands grasp the each objects and estimating the position and orientation of grasped objects using kinematics information of hand-arm systems.

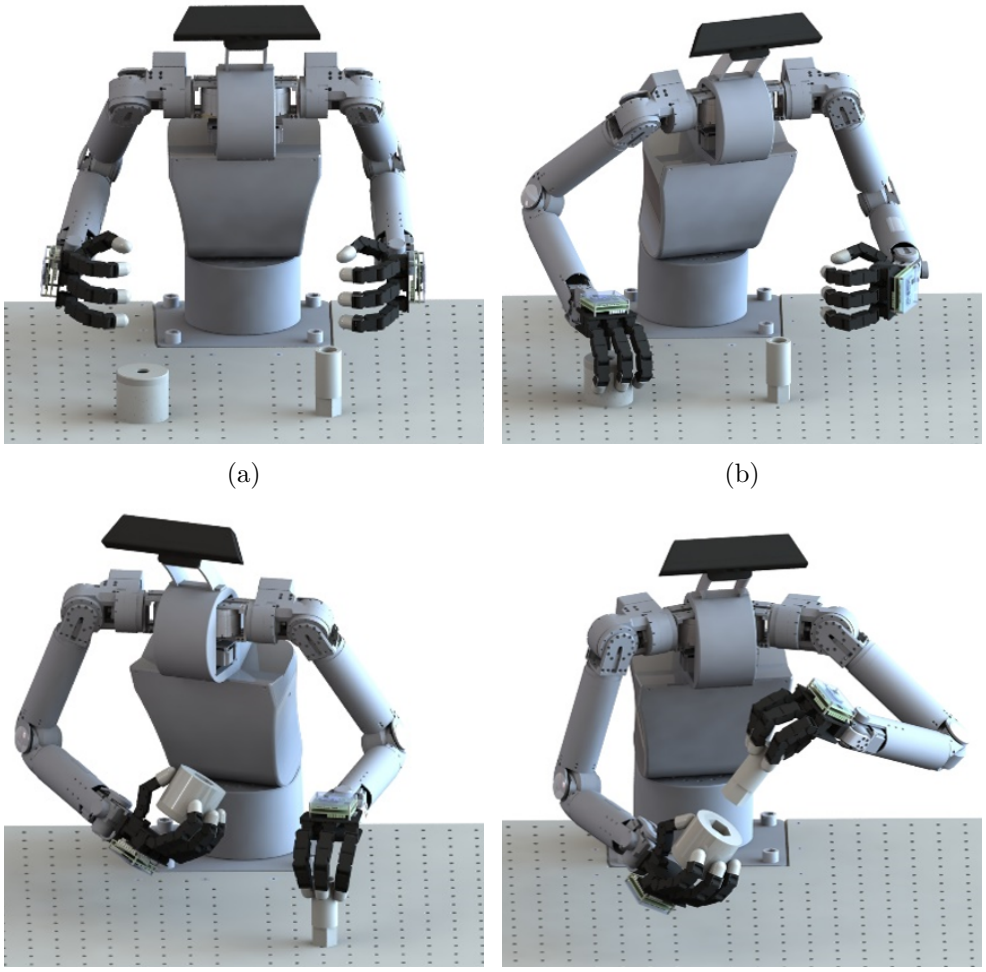

(a) (b)

(c) (d)

Figure 2.38: Procedure of dual arm peg-in-hole task: (a) initial posture; (b) grasping the hole with right hand; (c) grasping the peg with left hand; (d) assembling the peg and hole.

In the process of grasping and assembling an object with a humanoid hand, the kinematics information of the grasped object inevitably includes an error. Compliance-based peg-in-hole strategy is suitable for overcoming these initial object position errors, errors occurring during the grasping process, and estimation errors of the grasped objects.

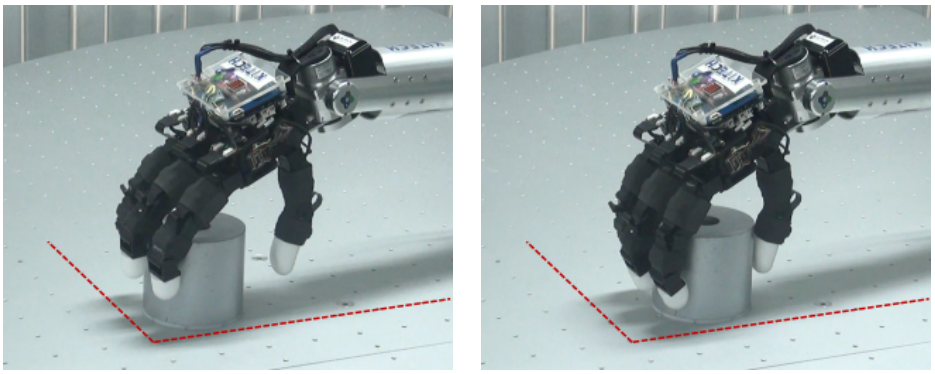

(a) (b)

Figure 2.39: Sliding the object on the table: (a) initial posture; (b) grasping the object.

2.5.4.1 Peg-in-Hole Procedure

The peg and the hole are placed on the table, and the position and orientation information of the object includes the uncertainty error. Fig. 2.38 show the procedure of peg in hole task with upper body robot.

The peg and hole are placed on the table, and the insertion direction of the peg and hole is perpendicular to the table. The robot holds the peg and the hole with both arms, and assembles them using the proposed strategy. As shown in Fig. 2.38(b) and (c), once each hand grasps the placed object, a gravity compensation term considering the weight of the object is added to the controller in subsequent operations. In order for the hand to grasp the placed object in a stable posture, the hand slides the object into the desired position in the hand. Fig. 2.39 shows before and after sliding the object.

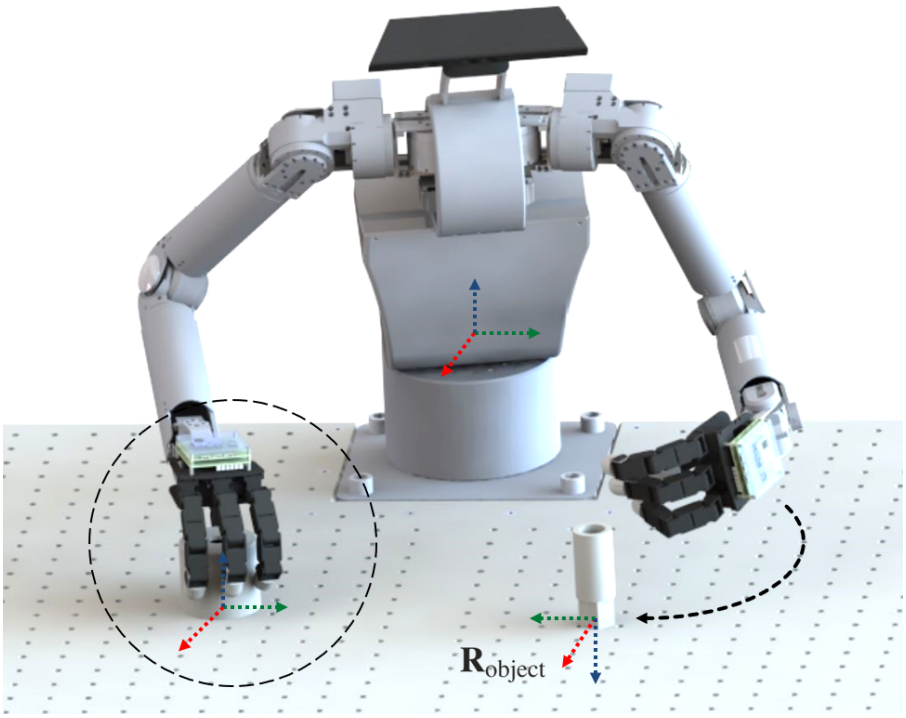

(a)

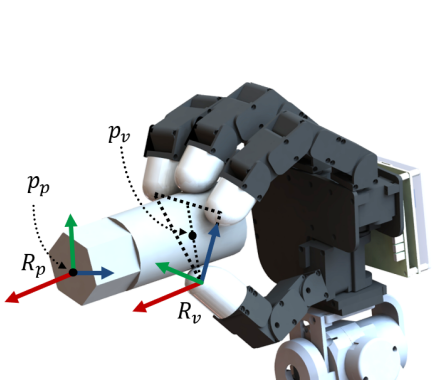

(b)

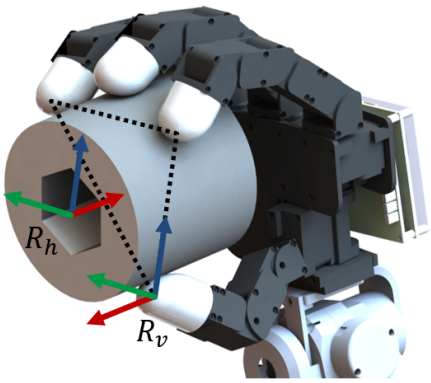

(c)

Figure 2.40: Kinematics of the grasped object: (a) the peg; (b) the hole.

2.5.4.2 Kinematics of Grasped Object

For the kinematic analysis of the object grasped by the hand, it is assumed that there is no slip and rolling between the fingertips and the grasped object. By the assumption, the kinematics of the gripped object was estimated using the kinematics information of the fingertips. Fig. 2.40(a) shows the moment when the robot grasps the object placed on the table.

Let's define the transformation matrix of an object placed on the floor as ${}^{0}\boldsymbol{T}_{\text{object}}$ in the global coordinate system. If the transformation matrix of the triangle defined by three fingers is expressed as ${}^{0}\boldsymbol{T}_{\text{v}}$, the kinematics of the object at the moment of grip is defined as

$$ {}^{0}\boldsymbol{T}_{\text{object}} = {}^{0}\boldsymbol{T}_{\text{v}} \, {}^{\text{v}}\hat{\boldsymbol{T}}_{\text{object}}. \tag{2.20} $$

${}^{0}\boldsymbol{T}_{\text{v}}$ is calculated using kinematics, and ${}^{\text{v}}\hat{\boldsymbol{T}}_{\text{object}}$ at the moment of holding the object is obtained as a constant matrix. Then, when lifting and handling the object, the kinematics of the object are estimated by multiplying the current ${}^{0}\boldsymbol{T}_{\text{v}}$ by ${}^{\text{v}}\hat{\boldsymbol{T}}_{\text{object}}$. Fig. 2.40(b) and (c) show the ${}^{0}\boldsymbol{T}_{\text{v}}$ and ${}^{\text{v}}\hat{\boldsymbol{T}}_{\text{object}}$.

2.5.4.3 Control Frameworks

The control input torque vector is defined as follows:

$$\boldsymbol{\tau}_{\mathrm{u}} = \begin{bmatrix} \boldsymbol{\tau}_{\mathrm{w}} & \boldsymbol{\tau}_{\mathrm{ra}} & \boldsymbol{\tau}_{\mathrm{la}} & \boldsymbol{\tau}_{\mathrm{rh}} & \boldsymbol{\tau}_{\mathrm{lh}} \end{bmatrix}^{\mathrm{T}}. \tag{2.21}$$

Where $\boldsymbol{\tau}_{\mathrm{w}}$, $\boldsymbol{\tau}_{\mathrm{ra}}$, $\boldsymbol{\tau}_{\mathrm{la}}$, $\boldsymbol{\tau}_{\mathrm{lh}}$, and $\boldsymbol{\tau}_{\mathrm{rh}}$ denote torque input for waist, right arm, left arm, right hand, left hand, respectively. The left and right hands are controlled independently, and only play the role of grasping peg and hole. Since the right arm and the left arm share the waist joint, the waist control input was calculated by adding the control input of each arm. $\boldsymbol{\tau}_{\mathrm{w}}$, $\boldsymbol{\tau}_{\mathrm{ra}}$, and $\boldsymbol{\tau}_{\mathrm{la}}$ are defined as

$$\begin{aligned} \boldsymbol{\tau}_{\mathrm{w}} &= \boldsymbol{S}_{\mathrm{w}}(\boldsymbol{\tau}_{\mathrm{r}} + \boldsymbol{\tau}_{\mathrm{l}}), \\ \boldsymbol{\tau}_{\mathrm{ra}} &= \boldsymbol{S}_{\mathrm{a}}\boldsymbol{\tau}_{\mathrm{r}}, \\ \boldsymbol{\tau}_{\mathrm{la}} &= \boldsymbol{S}_{\mathrm{a}}\boldsymbol{\tau}_{\mathrm{l}}. \end{aligned} \tag{2.22}$$

The KITECH upper body robot's waist and arm consist of 2 and 8-DOF. So, selection matrices $\boldsymbol{S}_{\mathrm{w}} \in \mathbb{R}^{2\times 8}$ and $\boldsymbol{S}_{\mathrm{a}} \in \mathbb{R}^{8\times 10}$ are designed as

$$\begin{aligned} \boldsymbol{S}_{\mathrm{w}} &= \begin{bmatrix} \mathrm{diag}(1,1) & 0_{2,6} \end{bmatrix}, \\ \boldsymbol{S}_{\mathrm{a}} &= \begin{bmatrix} 0_{8,2} & \mathrm{diag}(1,1,1,1,1,1,1,1) \end{bmatrix}. \end{aligned} \tag{2.23}$$

Where $0_{m,n}$ denote the $m \times n$ zero matrix. Jacobian matrix of the right and left arm including waist joint $\boldsymbol{J}_{\mathrm{r}}$ and $\boldsymbol{J}_{\mathrm{l}} \in \mathbb{R}^{6\times 10}$ are designed as

$$\begin{aligned} \boldsymbol{J}_{\mathrm{r}} &= \left[\frac{\partial \boldsymbol{p}_{\mathrm{r}}}{\partial \boldsymbol{q}_{\mathrm{r}}}\right], \quad \boldsymbol{q}_{\mathrm{r}} = [\boldsymbol{q}_{\mathrm{w}}\ \boldsymbol{q}_{\mathrm{ra}}]^{\mathrm{T}} \\ \boldsymbol{J}_{\mathrm{l}} &= \left[\frac{\partial \boldsymbol{p}_{\mathrm{l}}}{\partial \boldsymbol{q}_{\mathrm{l}}}\right], \quad \boldsymbol{q}_{\mathrm{l}} = [\boldsymbol{q}_{\mathrm{w}}\ \boldsymbol{q}_{\mathrm{la}}]^{\mathrm{T}} \end{aligned} \tag{2.24}$$

$\boldsymbol{q}_{\mathrm{r}}$ and $\boldsymbol{q}_{\mathrm{l}} \in \mathbb{R}^{10\times 1}$ denote the joint angle vector of each wrist including waist joint. By replacing $\boldsymbol{J}$ in Eq. (2.3) with $\boldsymbol{J}_{\mathrm{r}}$ and $\boldsymbol{J}_{\mathrm{l}}$, it becomes the $\boldsymbol{\tau}_{\mathrm{r}}$ and $\boldsymbol{\tau}_{\mathrm{l}}$ in Eq. (2.22).

2.5.4.4 Experiment Results

Fig. 2.41 shows the path of the peg and hole during the assembly process. In the process of searching, spiral trajectory of the peg clearly appears. Through the experiment, the feasibility of the proposed strategy was confirmed despite the

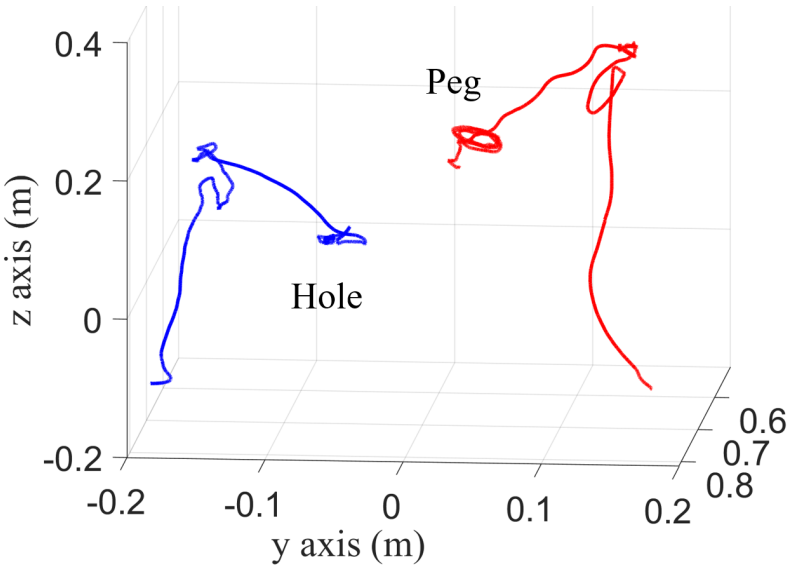

Figure 2.41: Trajectory of peg and hole grasped by hand.

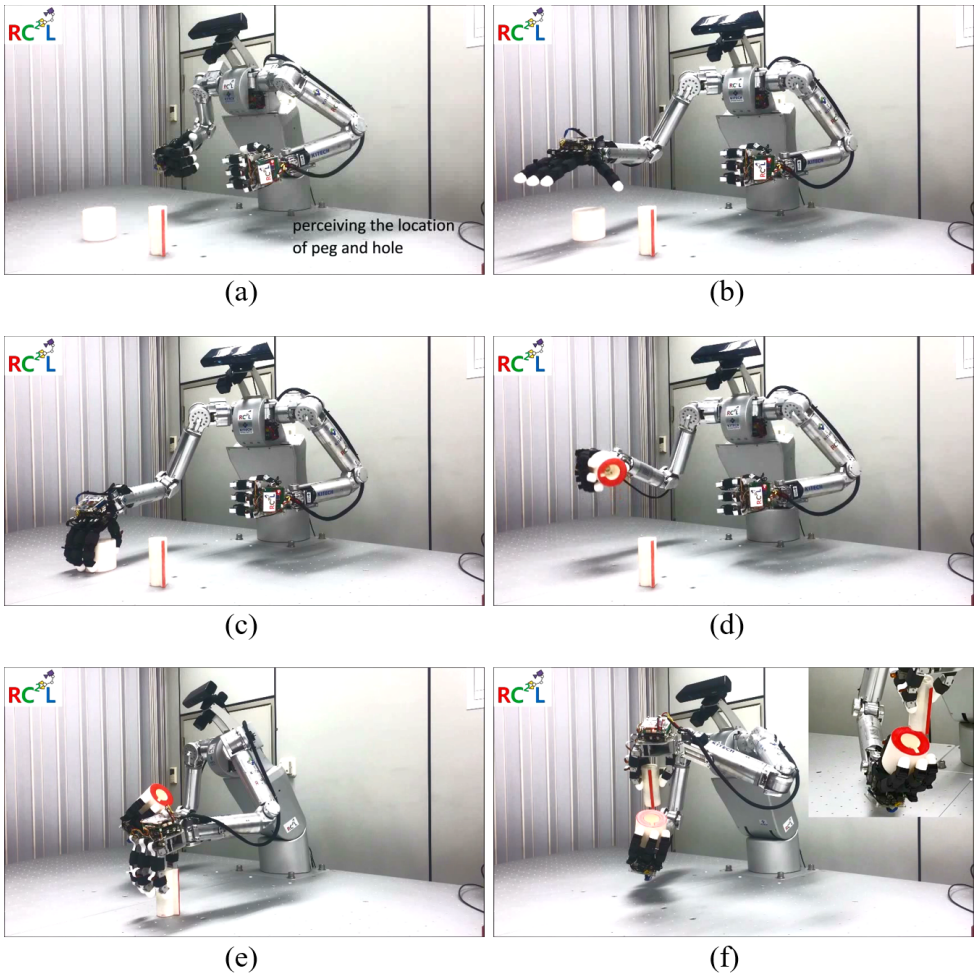

Figure 2.42: Snapshots of peg-in-hole assembly with dual hands: (a) initial posture, (b) approach to the hole, (c) grasp the hole, (d) lift the hole, (e) grasp the peg, and (f) ready to assemble the peg and hole.

initial error of the object, the error in the gripping process, and the estimation error of the kinematics of the grasped object.

Fig. 2.42 and Fig. 2.43 shows the snapshots of the peg and hole assembly experiment.

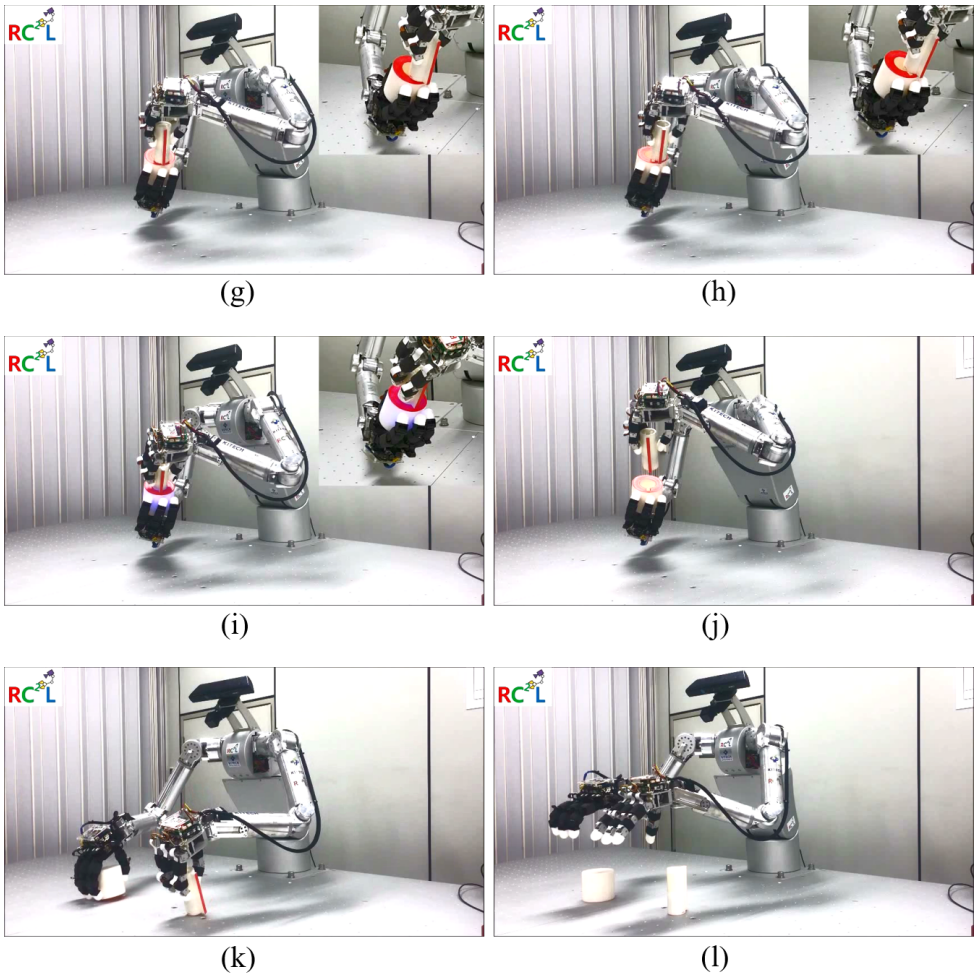

Figure 2.43: Snapshots of peg-in-hole assembly with dual hands: (g) contact between two objects, (h) search the hole, (i) insert the peg to the hole, (j) extract two objects, (k) put down the objects to table, and (l) release the objects.

2.6 Discussion

2.6.1 Peg-in-Hole Transition

In section 2.3.2, the peg-in-hole procedure was divided into three steps:approaching, searching, and inserting. In the actual experiment, the peg-in hole process does not sequentially follow the three steps depending on the uncertainty of information about the hole. Fig. 2.44 depicts the transition map of peg-in-hole procedure. The thickness of the line indicates the frequency of transition. The peg-in-hole procedure starts in the state shown in Fig. 2.44(a). The process of peg-in-hole by the proposed strategy generally follows from Fig. 2.44(a) to (b) to (c) to (d). In extremely rare cases, the assembly task go from (a) to (d) at once. As a result of the experiment, depending on uncertainty of the position error and the orientation error, there were cases where (a) to (b) to (d) or (a) to (c) to (d). If the process of searching the hole fails because the error of the hole information exceeds the strategy's overcoming range, the strategy starts again from the beginning through step (e). Since there are various cases of such a peg-in-hole process, the proposed peg-in-hole strategy has the advantages of high success rate and disadvantages of large variance of elapsed time.

2.6.2 Influential Issues

In this section, I discuss a few issues the effect of peg/hole size, acceptable recognition error, and manipulator issues not addressed in earlier sections. Firstly, I investigated if the peg/hole size affects the performance of task completion using comparatively smaller 20 mm and 10 mm diameter pegs and corresponding holes. After performing a hundred experiments with optimal gains, obtained

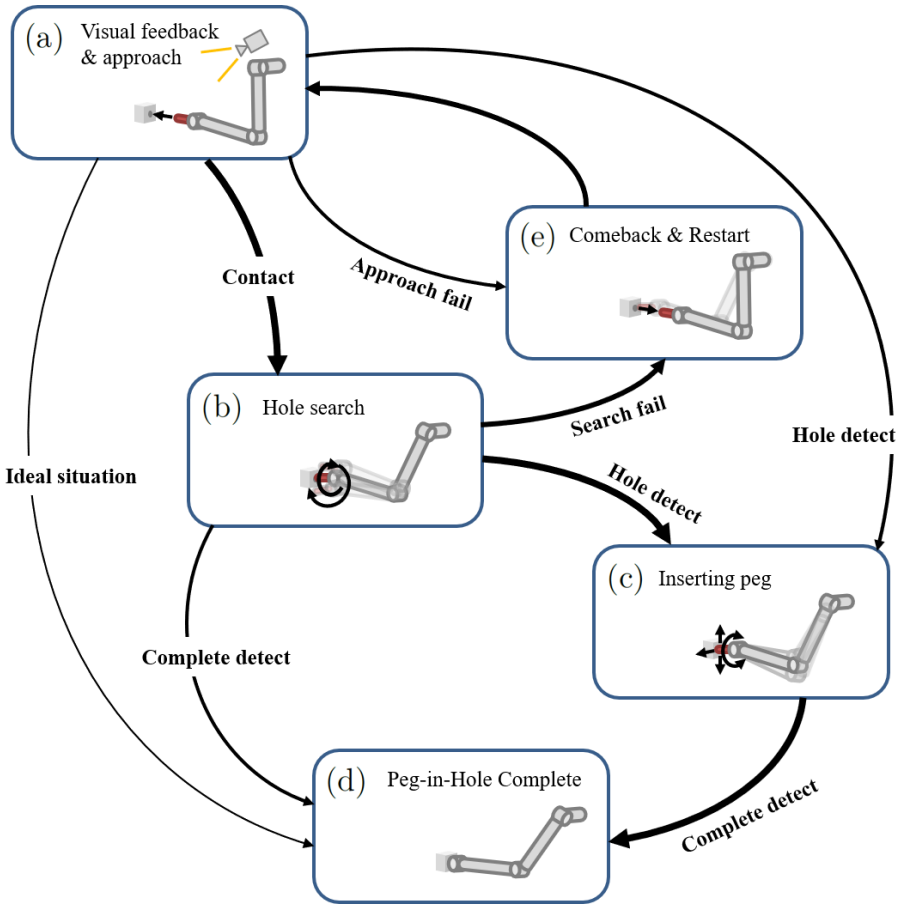

Figure 2.44: Peg-in-hole transition map.

using the method presented in section 2.5.2.2, I was able to achieve an average task completion time of 6.3 seconds with a 100% success rate. In these experiments, the spiral path for searching the hole was regenerated according to the peg diameter, and it was confirmed that the size of the peg hardly affected the peg-in-hole performance in a reasonable range of peg sizes (10-50 mm).

Meanwhile, the accuracy of object (hole) recognition affects the performance of the proposed method. The proposed strategy assumes that the recognition information is rough; but there is a range of perceived information that must

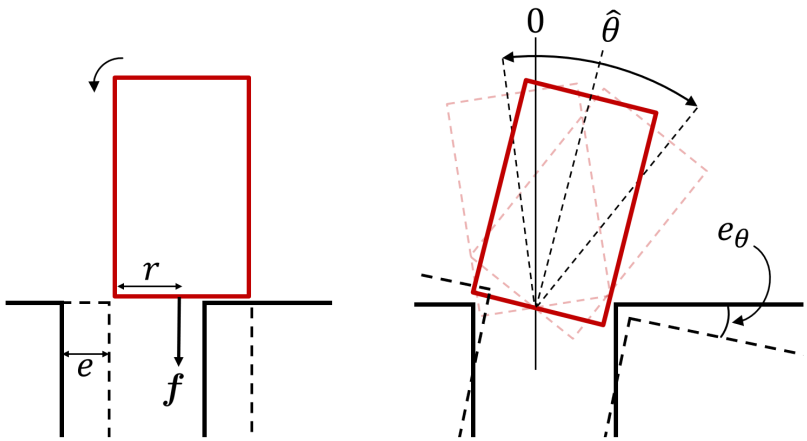

Figure 2.45: Impact of recognition error: (a) position; (b) orientation.

come within a certain range. Fig. 2.45(a) shows the relationship between the recognition error and peg radius. The solid line indicates the position of the actual hole, and the dotted line indicates the position of the hole estimated through the recognized information. In order for the tip of the peg to tilt into the hole, the maximum recognition error must be less than the peg radius.

Fig. 2.45(b) shows the range of wiggling to reduce the recognized orientation error. The wiggle range, based on the recognition error, should theoretically have values starting from zero degrees and not exceeding 90 degrees. A value of zero indicates a true value, and if the angle exceeds 90 degrees, the peg deviates away from the hole. Through various experiments, it was confirmed that the success rate is high when the search range is greater than twice the error. Therefore, the maximum recognition error of the vision system should be less than 30 degrees.

In addition, a hardware issue related to robot performance must be noted. Although I employed a redundant 8-DOF robotic arm for the experiments,

redundancy is not a necessary condition to apply the proposed method. On the other hand, the motor drive system of the manipulator must be capable of torque control to ensure control over the robot force. Robotic joints, in general, have low gear ratios and low friction for a passively compliant motion. Each joint of the robotic arm in this research had a 100:1 gear ratio with torque control capability based on current servoing.

Chapter 3

WRENCH TRAJECTORY

The proposed peg-in-hole strategy generates an assembly force following spiral force trajectory and succeeds in assembling through adaptation to the environment. This method achieves a high success rate, but it is difficult to predict the completion time because the search process is highly dependent on the initial error. In this chapter, I analyze the spiral force trajectory, and propose the advanced force trajectory[50]. Probability concept is used in the process of analyzing and proposing force trajectory. The proposed force trajectory has the faster average success time and the smaller distribution of elapsed-time performance than those of the spiral trajectory.

3.1 Problem Statement

3.1.1 Hole Search Process

In chapter 2, the contact status between peg and hole is classified into four cases. Fig. 3.1 shows the five classification of the contact states between the polygon peg and hole. The line contact state shown in Fig. 3.1 is added according to the inclined direction of the peg, but only four contact state is considered by tilting the peg in the direction of the vertex. The two-point contact state is the most frequent situation encountered during peg-in-hole assembly. The three-point contact state is the globally unique solution for peg-in-hole assembly associated with a fixed orientation [51]. In this study, I considered this three-point contact state as the completion of the hole search process. The hole search process begins with uncertainty regarding the location of a hole. The inaccurate geometric information of a hole $\hat{\boldsymbol{p}}_{\mathrm{h}}$ is expressed as

$$\begin{aligned} \hat{\boldsymbol{p}}_{\mathrm{h}} &= \boldsymbol{p}_{\mathrm{h}} + \boldsymbol{e}, \\ \boldsymbol{e} &= \begin{bmatrix} e_x & e_y & e_z & e_\alpha & e_\beta & e_\gamma \end{bmatrix}^{\mathrm{T}}, \end{aligned} \tag{3.1}$$

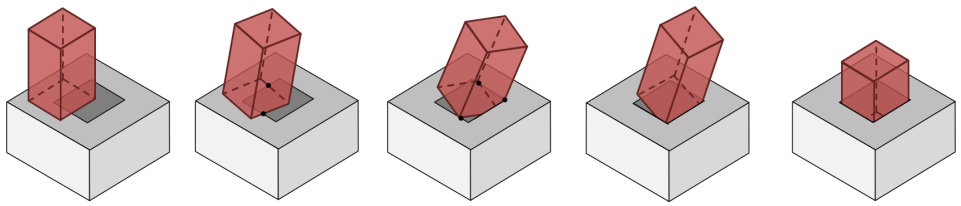

Figure 3.1: Contact state between polynonal peg and hole: (a) plane contact, (b) two-point contact, (c) three-point contact, (d) line contact, and (e) insert.

$\boldsymbol{p}_{\mathrm{h}} \in \mathbb{R}^{6\times1}$ denotes precise information on the hole. $\boldsymbol{e} \in \mathbb{R}^{6\times1}$ denotes the error during recognition of the hole position and orientation. Suppose that the insertion is along the z-direction. For finding the position of the hole, the depth of the insertion need not to be considered. Thus, $\boldsymbol{e}$ can be expressed using polar coordinates as

$$\boldsymbol{e} = \begin{bmatrix} e_r\cos(e_\theta) & e_r\sin(e_\theta) & e_z & e_\alpha & e_\beta & e_\gamma \end{bmatrix}^{\mathrm{T}}, \tag{3.2}$$

e_r and e_θ denote the radial distance and polar angle between the exact and estimated position of the hole, respectively. For searching the hole position without force feedback, the Archimedes spiral trajectory obtained by linearly changing $\hat{e}_r$ and $\hat{e}_\theta$ is commonly used in search algorithms[22], [53]. In our study, I assumed the magnitude of e_r to be smaller than the radius of the inscribed circle of the assembly object so that assembly could be started in the two-point contact state.

Fig. 3.2(a) and (b) present the various views of the two-point contact state shown in Fig. 3.1(b). A and B indicate the contact points. $\boldsymbol{f}_{\mathrm{a}}$ represents the assembly force applied on the peg. Fig. 3.2(c) and (d) illustrate the spiral force trajectory. $\boldsymbol{f}_t$ is the force vector responsible for changing the contact state from the two-point contact state the three-point contact state. Because the information on e_θ in (3.2) is uncertain, the force trajectory should cover the entire range of [0 2π]. Consequently, this method has a high success rate; however, the time consumed in the search process is always unpredictable.

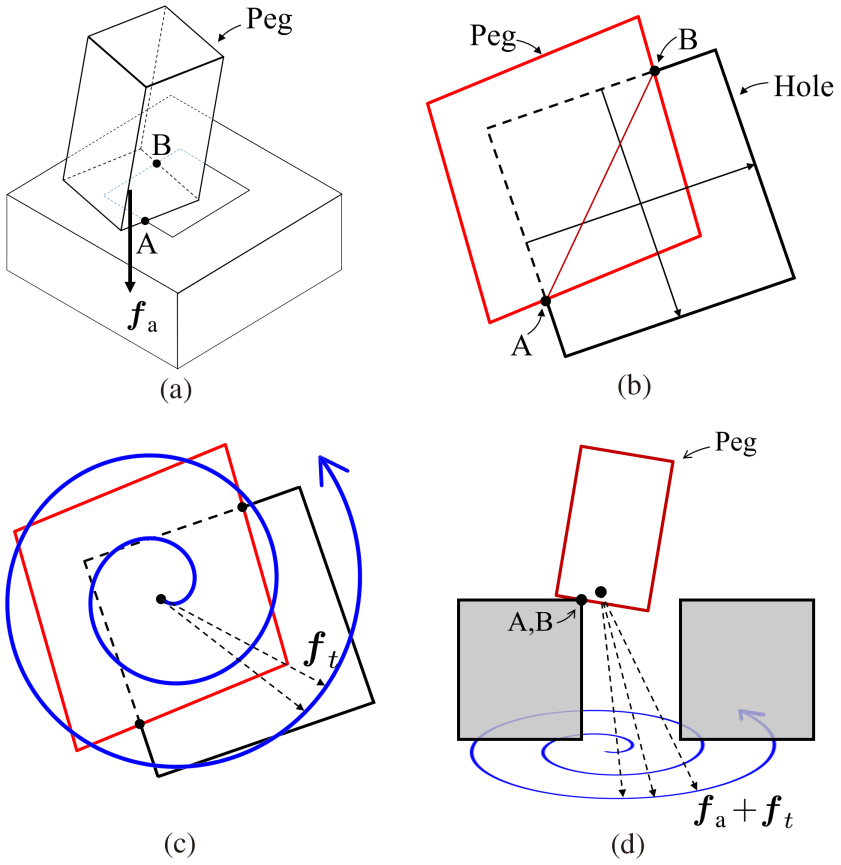

Figure 3.2: Diagram of two-point contact between square peg and hole: (a) example of two-point contact, (b) top view, and (c) spiral force trajectory in top view (d) and side view.

3.1.2 Spiral Force Trajectory Analysis

Fig. 3.3 depicts the spiral force trajectory(SFT). The path expands and contracts, and the trajectory overlaps the previous path. $\boldsymbol{f}_t$ is generated to vary along spiral trajectory $\boldsymbol{p}_t$ at a constant velocity over time t. h represents the change in $\boldsymbol{p}_t$ during Δt. $\boldsymbol{f}_t$ is determined by multiplying the distance between

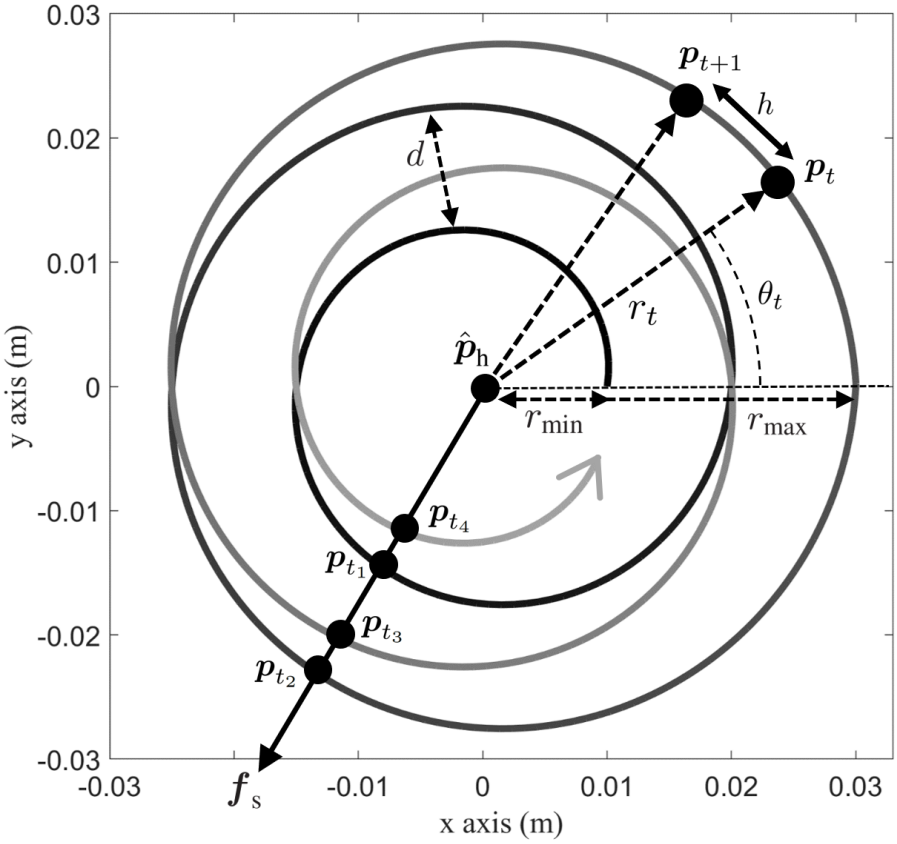

Figure 3.3: Spiral force trajectory.

peg position $\boldsymbol{p}_{\mathrm{p}}$ and $\boldsymbol{p}_t$ by spring constant k_p as

$$\boldsymbol{f}_t = k_p(\boldsymbol{p}_t - \boldsymbol{p}_{\mathrm{p}}). \tag{3.3}$$

Compliant behavior is implemented by determining k_p. Setting k_p to a low value renders the robot softer. r_t and θ_t for $\boldsymbol{p}_t$ are defined as follows:

$$\theta_t = \theta_{t-1} + \tan^{-1}\left(\frac{h}{r_t}\right),$$
$$r_t = \begin{cases} r_{\min} + (\theta_t - \theta_o)\frac{d}{2\pi}, (\dot{r_t} > 0) \\ r_{\max} - (\theta_t - \theta_o)\frac{d}{2\pi}, (\dot{r_t} < 0) \end{cases} \tag{3.4}$$

The r_t and θ_t values of the force trajectory have ranges of $[r_{\min},\ r_{\max}]$ and $[0,\infty]$, respectively. The trajectory is created until the peg and hole are in a three-point contact state. θ_o has an initial value of 0 and is updated with the current angle when the direction of the SFT is changed.

When the peg and hole are currently in a two-point contact state, the force vector generated to change the state to a three-point contact state is $\boldsymbol{f}_{\mathrm{s}}$, shown in Fig. 3.3. If θ_{s} represents the angle of $\boldsymbol{f}_{\mathrm{s}}$, then $\boldsymbol{p}_t(r_t, \theta_t)$ having the same angle as θ_{s} is defined as follows:

$$\boldsymbol{p}_{t_n} = \boldsymbol{p}_t(r_t, \theta_{\mathrm{s}} + 2(n-1)\pi),\ \ (n = 1, 2, \cdots, \infty). \tag{3.5}$$

$\boldsymbol{p}_{t_n}$ represents a vector having the same angle as θ_{s} among the $\boldsymbol{p}_t$ vectors with the nth overlap with θ_{s}. Because of uncertainties such as peg and hole contact situations, the amount of compliance of the peg, and contact friction, it is probable that the contact state of the peg and the hole changes to a three-point contact state when $\boldsymbol{p}_t$ passes $\boldsymbol{p}_{t_n}$. When t is t_n, P is defined as the probability of reaching a three-point contact state. P is determined by the amount of compliance, magnitude of the assembly force, contact state, and velocity of the SFT. I assumed P as always equal to a certain constant value. The estimated

elapsed time t_n, expected value, and variance of t_n to reach the three-point contact state through $\boldsymbol{f}_{t_n}$ are determined as follows:

$$t_n(\theta_\mathrm{s}) = \frac{1}{v}\int_0^{\theta_\mathrm{s}+2(n-1)\pi} \sqrt{{r_t}^2 + \left(\frac{dr_t}{d\theta_t}\right)^2}\, d\theta_t,\ v = \frac{h}{\Delta t}. \tag{3.6}$$

The elapsed time t_n is calculated by dividing the length of the arc by the velocity. For integration, $\tan^{-1}(h/r_t)$ in Eq. (3.4) is converted to h/r_t using small-angle approximation. The distribution of t_n is determined by probability P and the increase in the integral range. To analyze the distribution of t_n considering P for various θ_s, sample elapsed time $\hat{t}_n$ is calculated for random samples θ_s. Algorithm 1 explains the process for calculating the $\hat{t}_n$ of N samples having angle θ_s created by uniform distribution $U(0, 2\pi)$. The mean and variance of $\hat{t}_n$ are defined as

$$\mu = \frac{1}{N}\sum_{n=1}^{N}\hat{t}_n, \quad \sigma^2 = \frac{1}{N}\sum_{n=1}^{N}(\mu - \hat{t}_n)^2. \tag{3.7}$$

Algorithm 1 N elapsed time by N random sample of θ_s

Input: Probability P defined by constant
Output: N elapsed time $\hat{t}_i$ (i=1, 2, $\cdots$, N)
  Initialize : $\hat{\theta}_i \in U(0, 2\pi)$ (i=1, 2, $\cdots$, N)
  for $i = 1$ to N **do**
    for $j = 1$ to ∞ **do**
      if ($rand$(0,1) $\leq$ P) **then**
        $\hat{t}_i = t_j(\theta_i)$
      end if
    end for
  end for
  return $\hat{t}_i$ (i=1, 2, $\cdots$, N)

Table 3.1: μ and σ of $\hat{t}_n$ about various P with SFT; success failure criteria is $100s$

P	μ	σ	success rate
0.2	35.37 s	44.14 s	100 %
0.4	14.16 s	14.78 s	100 %
0.6	7.55 s	8.20 s	100 %
0.8	4.28 s	4.52 s	100 %

The mean and standard deviation of elapsed time $\hat{t}_n$ for 250 samples having angle θ_{s} are listed in Table 3.1. The success rate is calculated by defining the threshold time for success and failure. The mean and standard deviation indicate clearly the high performance of the compliance-based peg-in-hole strategy using SFTs. High success rates are based on generous success time criteria, and a short average elapsed time is accompanied by high standard deviations.

The standard deviation can be reduced by decreasing the distribution of t_n or increasing probability P. The reason for the wide distribution of t_n is that the integral range θ_t increases by 2π for every increase in n. Thus, to reduce the variance of tn, I propose a PSFT with a limited integral period and compliance-based controller to increase P.

3.2 Partial Spiral Force Trajectory

3.2.1 Force Trajectory with Tilted Posture

To overcome e_r with a range of [0,2π], the polar angle range of the force trajectory was set to [0,2π]. The concept of "attractive region" was used to reduce the range of the force trajectory. Qiao *et al.* presented the "attractive region in envi-

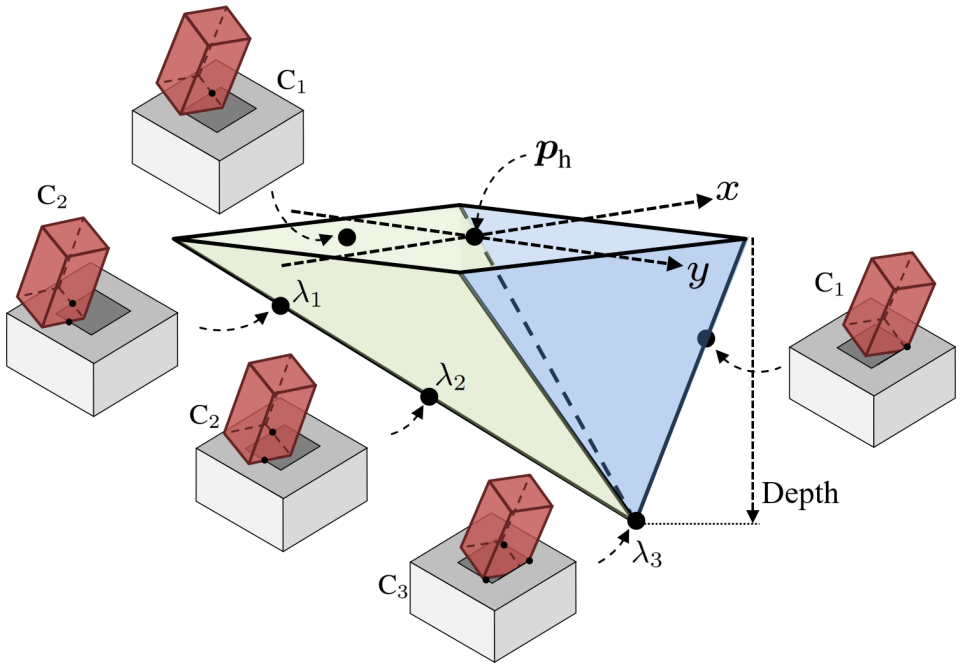

Figure 3.4: Constrained region formed by the square peg and hole in the configuration space when the orientation of the peg is fixed; C_i denotes the i-th point contact state.

ronment (ARIE)" that visualizes the contact state of the peg and hole[51],[52]. The ARIE is a representation of a set of peg positions in Cartesian coordinates when the tilted peg is in contact with the hole. Fig. 3.4 shows the motion region of the square peg constrained by the edge of the square hole in the configuration space. The depth of the ARIE depends on the tilting angle of the peg. The lowest globally unique point, λ_3, represents three-point contact between the peg and hole. C_3 is the stable state of the assembly system in the ARIE. The proposed force trajectory aims at paths λ_1, λ_2, and λ_3 starting from the two-point contact state and reaching the three-point contact state. If the peg-in-hole assembly is started in state λ_1, the range of the force trajectory is confined. For the first contact state of the peg and hole to be λ_1, the peg must initially be intentionally tilted and translated in a specific direction. These motions increase

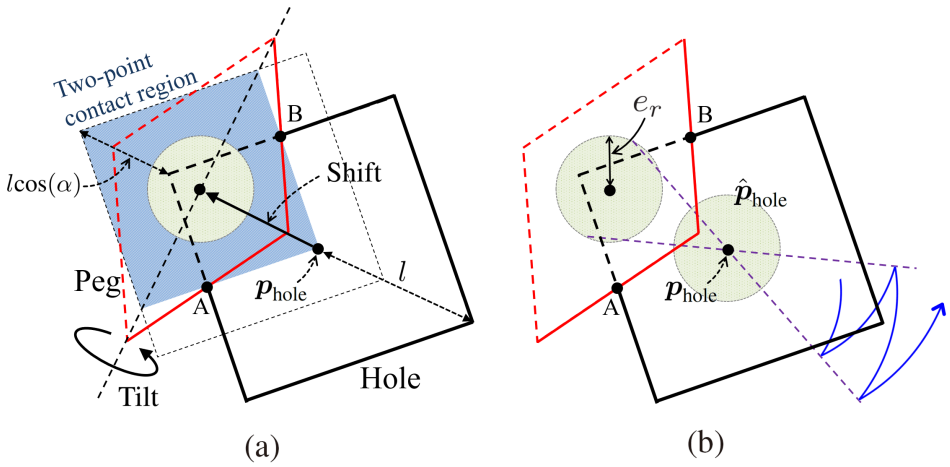

Figure 3.5: Top view after shift and tilt motions: (a) two-point contact region and (b) partial spiral force trajectory.

the initial error $\boldsymbol{e}$ and elapsed time but provide a reduction in the mean and variance of the elapsed time.

Fig. 3.5(a) depicts the region of $\boldsymbol{p}_{\text{p}}$ where the peg and hole are in the two-point contact state. Let the tilting angle be α, and distance between the center of the hole and the edge point chosen to be the third contact point be l. The magnitude of the displacement required to shift the initial position of the peg to the center of the two-point contact region is

$$\frac{1}{2}(l + l\cos(\alpha)). \tag{3.8}$$

Fig. 3.5(b) presents the partial spiral force trajectory required to change the current contact state to a three-point contact state. The polar angle range of the PSFT is designed to be larger than

$$2\tan^{-1}\left(\frac{2e_r}{l + l\cos(\alpha)}\right). \tag{3.9}$$

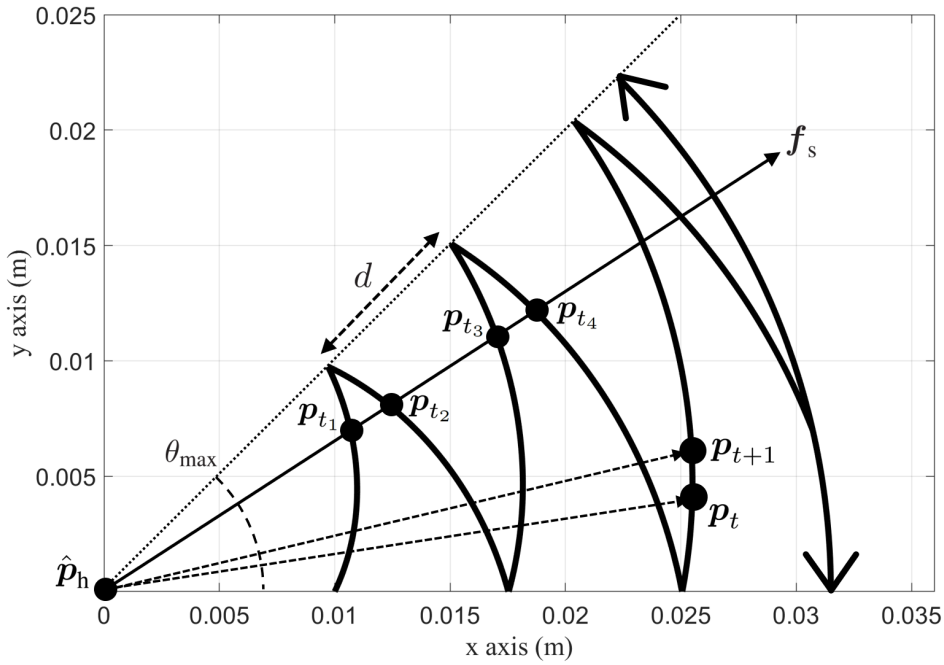

Figure 3.6: Partial spiral force trajectory.

The peg is moved by the PSFT while maintaining the two-point contact state, and it is stopped once it reaches the three-point contact state.

Fig. 3.6 shows the PSFT. Vector $\boldsymbol{p}_t(r_t, \theta_t)$ is generated using

$$\theta_t = \begin{cases} \theta_{t-1} + \tan^{-1}(\frac{h}{r_t}), (\text{dir} = \text{ccw}) \\ \theta_{t-1} - \tan^{-1}(\frac{h}{r_t}), (\text{dir} = \text{cw}) \end{cases},$$
$$r_t = \begin{cases} r_{\min} + \hat{\theta}_t \frac{d}{2\theta_{\max}},\ \hat{\theta}_t = \hat{\theta}_{t-1} + \tan^{-1}(\frac{h}{r_t}) \\ r_{\max},\ (r_t > r_{\max}) \end{cases}. \tag{3.10}$$

θ_t has a value in the range of $[0, \theta_{\max}]$, and r_t increases from $r_{\min}$ to $r_{\max}$. Elapsed time t_n is calculated using the following equation:

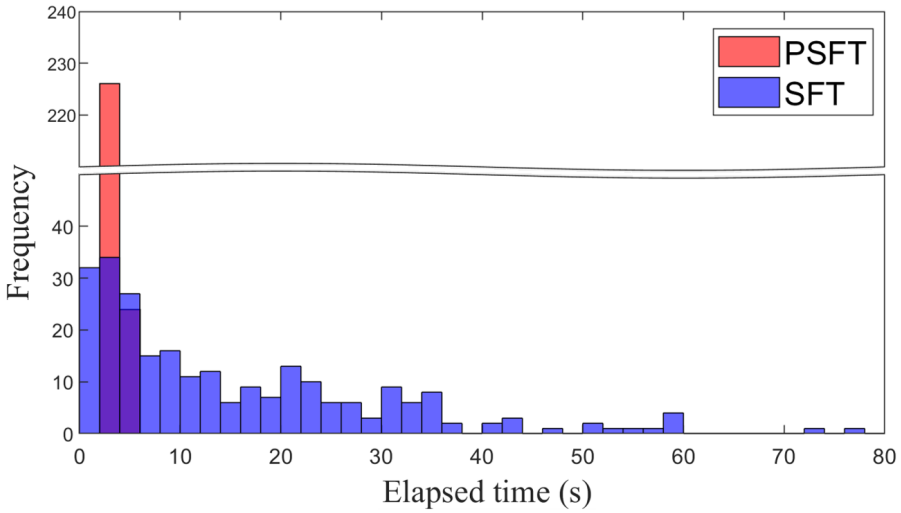

Figure 3.7: Histogram of $\hat{t}_n$; h, P, Δt, t_{tilt} , and $\theta_{\max}$ are set to 0.0005, 0.4, 0.003, 3, and $\pi/2$, respectively.

$$
\begin{aligned}
t_n &= \frac{1}{v}\int_0^{\theta_{t_n}} \sqrt{{r_t}^2 + \left(\frac{dr_t}{d\hat{\theta}_t}\right)^2}\, d\hat{\theta}_t + t_{\text{tilt}},\ v = \frac{h}{\Delta t} \\
\theta_{t_n} &= \begin{cases} (n-1)\theta_{\max} + \theta_{\text{s}}, (n = 1, 3, 5, \cdots) \\ n\theta_{\max} - \theta_{\text{s}}, (n = 2, 4, 6, \cdots) \end{cases}.
\end{aligned}
\tag{3.11}
$$

t_{tilt} denotes the offset time caused by shift and tilt motions. As mentioned in the previous subsection, $\hat{t}_n$ values were calculated from $\hat{\theta}_{\text{s}}$ of random samples. Fig. 3.7 shows the histogram of $\hat{t}_n$ with the PSFT and SFT obtained from θ_{s} of 250 samples belonging to $U(0, \pi/2)$. The mean and standard deviation were calculated and they are listed in 3.2. The standard deviation observed in the PSFT is eight times lower than that observed in the SFT.

Fig. 3.8 illustrates the entire peg-in-hole assembly process performed using the proposed strategy. When the task starts, the peg approaches the hole owing

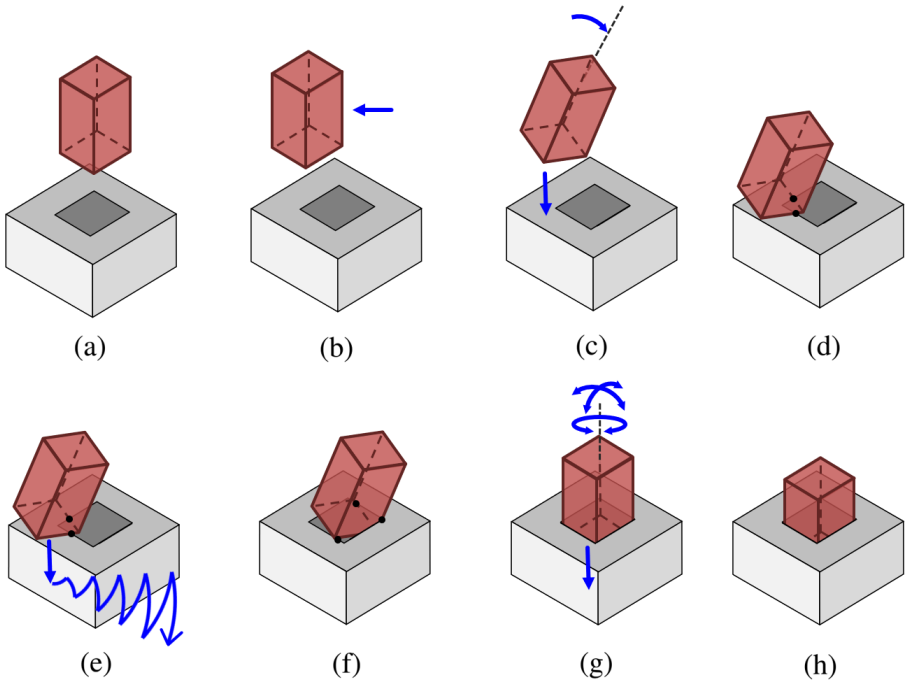

Figure 3.8: Peg-in-hole procedure with PSFT: (a) init, (b) shift, (c) tilt and push, (d) two-point contact, (e) PSFT, (f) three-point contact, (g) screw and wiggle, and (h) finish.

to the assembly force in the tilted and shifted states. When the peg contacts the vicinity of the hole, it stops and the phase transitions to the next steps. Because of the PSFT, the contact state changes from the two-point to the three-point contact state. The peg is still tilted and is pushed deeper. At the end of this phase, the peg stops in the three-point contact state. The insertion process is

Table 3.2: μ and σ of $\hat{t}_n$ at various P values; success/ failure criterion is $100s$.

P	μ	σ	success rate
0.2	7.39 s	5.20 s	100 %
0.4	4.47 s	2.13 s	100 %
0.6	3.66 s	1.03 s	100 %
0.8	3.34 s	0.51 s	100 %

accomplished through the wiggle motion. The wiggle motion helps the peg fit into the hole by repeatedly rotating it along the vertical and horizontal planes. The transition from the current phase to the next one occurs when the peg stops. The velocity of the peg is determined through kinematic information from the robot.

3.2.2 Probability to Three-point Contact

For the peg to be able to adapt in three-point contact state, the compliance characteristic and force equilibrium are important. The compliance is implemented using a passivity-based controller with low spring constant gain,[55],[56]. The proposed strategy is implemented by applying forces and moments to the peg. The wrench vector applying force and moment $\boldsymbol{f}^*$ are given as

$$\boldsymbol{f}^* = \begin{bmatrix} \boldsymbol{f} & \boldsymbol{m} \end{bmatrix}^{\mathrm{T}}. \tag{3.12}$$

$\boldsymbol{f}$ and $\boldsymbol{m} \in \mathbb{R}^{3\times 1}$ are the applied force and moment to the peg, respectively. These are set as follows:

$$\begin{aligned} &\boldsymbol{f} = \boldsymbol{\Omega}\boldsymbol{f}_t + \overline{\boldsymbol{\Omega}}\boldsymbol{f}_{\mathrm{a}}, \;\; \boldsymbol{f}_t = k_p(\boldsymbol{p}_t - \boldsymbol{p}_{\mathrm{p}}), \\ &\boldsymbol{m} = k_\omega \boldsymbol{\delta\Phi}, \quad \boldsymbol{\delta\Phi} = \boldsymbol{E}_{\mathrm{r}}(\boldsymbol{R}_t, \boldsymbol{R}_{\mathrm{p}}), \end{aligned} \tag{3.13}$$

where $\boldsymbol{\Omega} \in \mathbb{R}^{3\times 3}$ is the generalized task-specification matrix used to separate the position control space from the force control space. k_p is the proportional gain for the position control, and k_ω is the orientation control gain. $\boldsymbol{p}_t$ and

$\boldsymbol{p}_{\mathrm{p}} \in \mathbb{R}^{3\times1}$ are the desired and current position vectors of the peg, respectively, and $\boldsymbol{R}_t$ and $\boldsymbol{R}_{\mathrm{p}} \in \mathbb{R}^{3\times3}$ are the desired and current rotation matrices of the peg, respectively. The motions shown in Fig. 3.8 are implemented using $\boldsymbol{p}_t$ and $\boldsymbol{R}_t$. Finally, $\boldsymbol{\delta\Phi} \in \mathbb{R}^{3\times1}$ is the angular rotation error vector.

Spring constant k_p in (3.13) determines the amount of compliance and magnitude of $\boldsymbol{f}_t$. A smaller k_p makes it easy for the peg to adapt to the external environment, but it is difficult for the peg to move along the direction of the PSFT owing to contact friction. Compliance c_t and k_p are inversely related to each other. There is a minimum compliance required for adapting to the external environment. Thus, k_p is lower than $1/c_t$. If ϵ is defined as the minimum gain for the peg to overcome contact friction, k_p must be chosen such that

$$\epsilon < k_p < 1/c_t. \tag{3.14}$$

Fig. 3.9(a) presents the assembly force and force generated by the PSFT in two-point contact. For the peg to move toward three-point contact, the sum of $\boldsymbol{f}_{\mathrm{a}}$ and $\boldsymbol{f}_t$ must be greater than the frictional forces generated at contact points A and B. Fig. 3.9(b) shows $\boldsymbol{f}_{\mathrm{a}}$ and $\boldsymbol{f}_t$ in the three-point contact state. For the peg to stop and adapt to the three-point contact state, the sum of $\boldsymbol{f}_{\mathrm{a}}$ and $\boldsymbol{f}_t$ must be less than the sum of the frictional forces acting at contact points A, B, and C. Because the assembly force is set as small as possible to prevent breakage of the assembly object, $\boldsymbol{f}_{\mathrm{a}}$ must be set first and $\boldsymbol{f}_t$ t must be formulated considering k_p and $\boldsymbol{p}_t$. It is difficult to establish an accurate model because it is a friction-related problem in a contact state with uncertainty.

Therefore, I performed iterative simulations to find the optimal parameters for comparing the performance of SFT and PSFT.

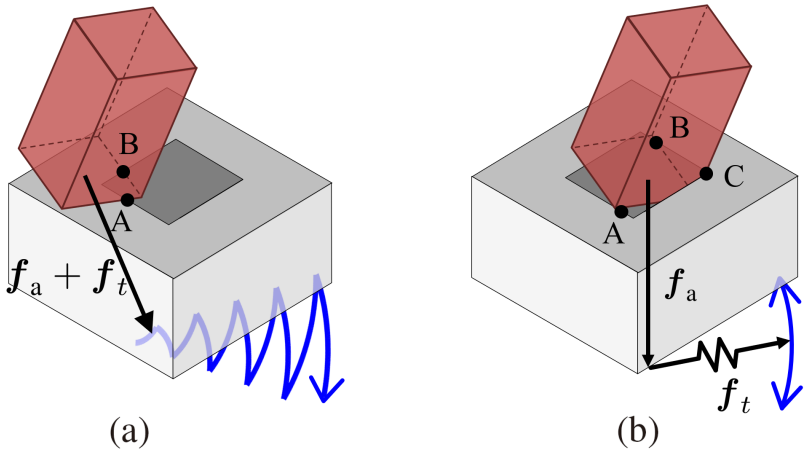

Figure 3.9: Assembly force and force generated by PSFT (a) two-point contact and (b) three-point contact.

3.3 SIMULATION & EXPERIMENT

3.3.1 Simulation

Simulations were performed to analyze the performance difference between the SFT and PSFT using the robotics simulator MuJoCo, which stands for multi joint dynamics with contact. The simulations were conducted with only the pegs and holes except the robot, and the assembly process was implemented by applying force and moments directly on the peg. Fig. 3.10 show the simulation environment.

The hole was square-shaped with a side of $50mm$, and the tolerance was $0.01mm$. The control frequency was set to 300 Hz. Because I used a simulation

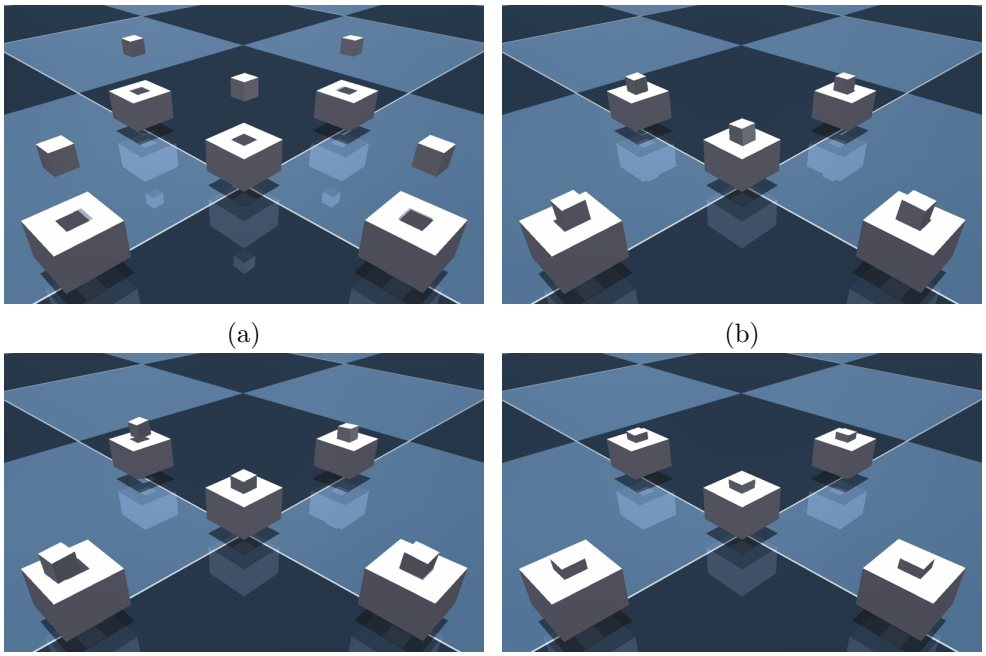

Figure 3.10: Simulation environment: (a) initial posture of the peg and hole, (b),(c) progress of the peg-in-hole assembly, and (d) finish posture.

environment, accurate geometrical information about the hole $\boldsymbol{p}_{\mathrm{h}}$ in (3.1) could be obtained. To obtain $\hat{\boldsymbol{p}}_{\mathrm{h}}$, the values of $\boldsymbol{e}$ were determined randomly within a uniform distribution, and they are listed in Table 3.3. The $\boldsymbol{e}$ values were different for each simulation.

When the SFT is used, the speed of the trajectory affects the strategy performance with k_p. Simulations were performed 250 times for each parameter

Table 3.3: Parameters for determining information error.

Parameter	Value range
e_r	$U(0, 15)$ [mm]
e_θ	$U(0, 2\pi)$ [rad]
e_α, e_β, e_γ	$U(-2, 2)$ [deg]

value, and the assembly was regarded as a failure when the elapsed time exceeded 100 s. Table 3.4 lists the success rate, average elapsed time, and standard deviation determined from the simulation results.

Fig. 3.11 show the simulation snapshots of peg-in-hole simulation with PSFT. According to the simulation results, the compliance-based peg-in-hole strategy using the SFT shows a 100% success rate within a certain range of parameters. However, along with this high success rate, this strategy shows a large standard deviation in the elapsed time. Figs. 3.12(a)-(c) depict the trajectory of the peg in three arbitrary cases. The graphs show that the standard deviation of the elapsed time is large because the time taken by the peg to reach

Table 3.4: Simulation with SFT; Success rate, μ, and σ are listed sequentially for each parameter duing 250 trials.

h	k_p			
	50	100	200	400
0.0005	66 %	100 %	100 %	100 %
	15.78 s	13.72 s	9.61 s	10.95 s
	22.37 s	12.64 s	6.08 s	5.69 s
0.001	66.4 %	99.2 %	100%	100 %
	14.06 s	12.52s	9.54 s	10.47 s
	19.68 s	10.3s	5.5 s	5.6 s
0.005	58.4 %	100 %	100 %	49.2 %
	12.41 s	9.76 s	10.1 s	15.81 s
	13.79 s	8.42 s	6.64 s	22.93 s
0.01	65.6 %	100 %	100 %	68.8 %
	9.89 s	12.75 s	8.74 s	23.49 s
	13.79s	15.4 s	6.01 s	26.58 s
0.02	57.6 %	88.8 %	90.4 %	65.6 %
	8.98 s	11.68 s	10.96 s	16.38 s
	11.29 s	14.42 s	13.9 s	23.27 s

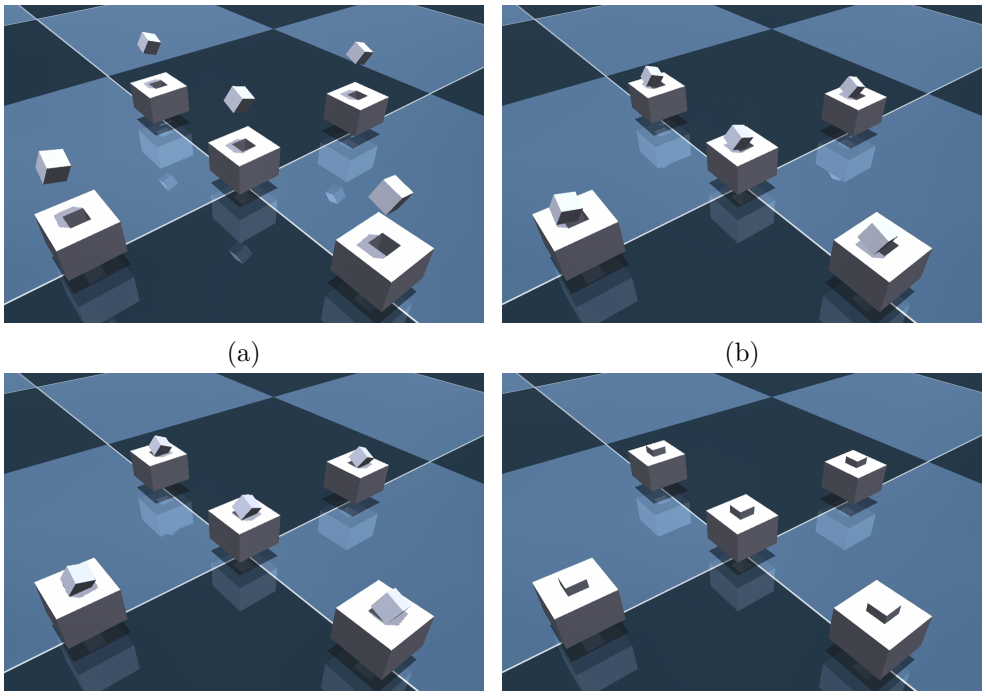

Figure 3.11: Simulation with PSFT: (a) initial posture of the peg and hole, (b) a two-point contact, (c) a three-point contact, and (d) finish posture.

the three-point contact state is highly different in each case.

According to Table 3.4, the SFT is valid within a certain range of parameters, as mentioned in (3.14). In this case, k_p had to be between 100 and 200. Additionally, the value of h had to be less than 0.01.

Figs. 3.12(d)-(f) show the graphs of the peg trajectory obtained using the PSFT. Because the process of searching the location of the hole is simplified, the elapsed time for the peg-in-hole process has much smaller variations. The performances of each strategy are summarized in Table 3.5. Each simulation was performed 250 times with the same parameters, and k_p and h were set to 200 and 0.001, respectively. The success rate is high for both cases, but the average

elapsed time of the PSFT is shorter. In particular, considering the standard deviation, the PSFT definitely exhibits a low deviation in the elapsed time.

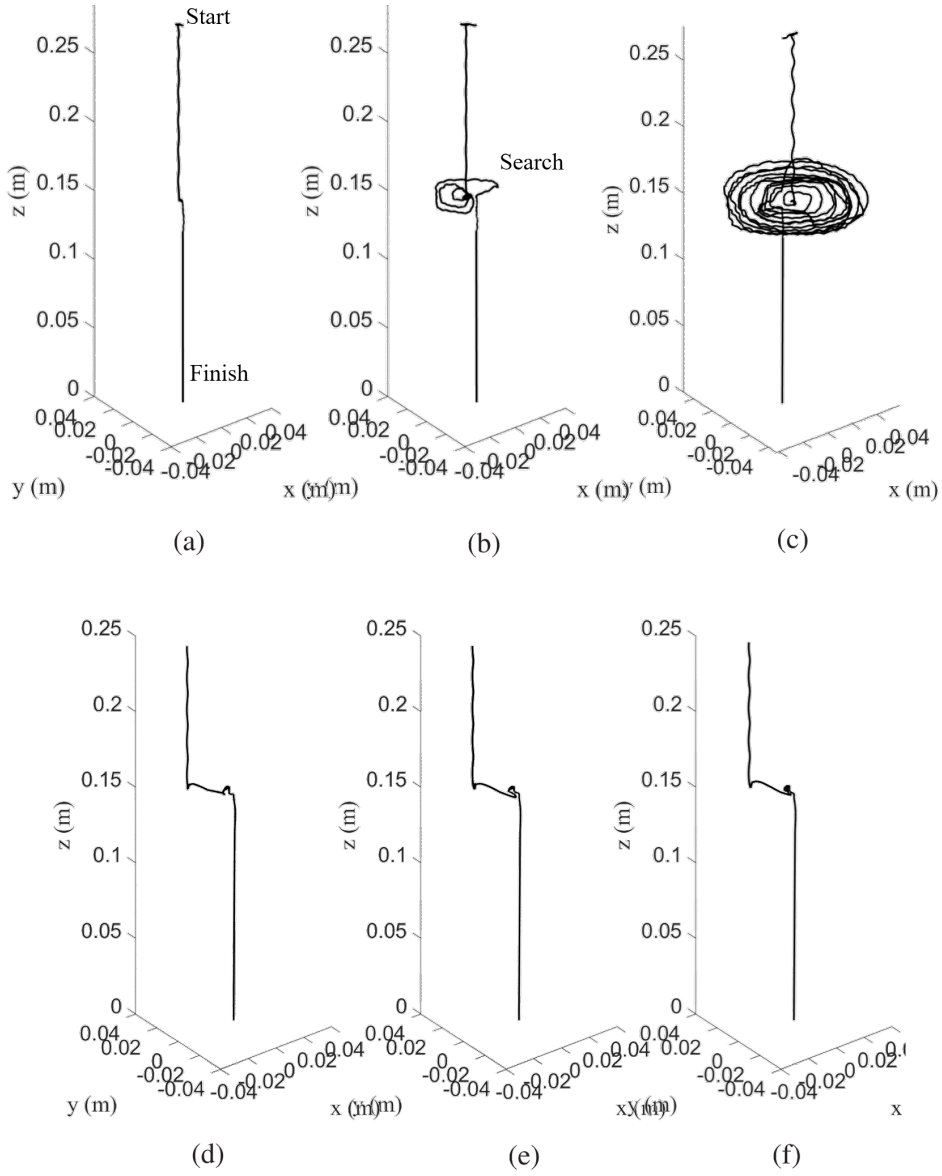

Figure 3.12: Sample graphs showing the peg trajectory observed during simulations with SFT:(a)-(c) and PSFT(d)-(f); elapsed times according to each graph are (a) 5.289 s, (b) 8.808 s, (c) 12.465 s, (d) 5.217 s, (e) 5.148 s, and (f) 5.136 s. k_p and h are 200 and 0.001, respectively.

Table 3.5: Means and standard deviations observed in SFT and PSFT simulations.

	μ	σ	Success rate
SFT	9.54 s	5.5 s	100 %
PSFT	7.37 s	0.2 s	100 %

3.3.2 Experiment

To verify the feasibility of the proposed strategy, peg-in-hole assembly experiments with a manipulator were performed. An eight-joint manipulator was used for the experiments[57]. The manipulator has torque control capability based on current servoing. The peg was installed at the end of the manipulator, and the hole was fixed at the environment, respectively. The pegs and holes were square-shaped with sides measuring $49.9mm$ and $50mm$, circular with diameters of $49.9mm$ and $50mm$ circular, and triangular with sides measuring $42.95mm$ and $43mm$, respectively. The experiments for all the shapes were performed with all the parameters and gains set equal.

When a peg attached to the manipulator encounters the external environment, friction from all joints prevents the peg from adapting to the contact force. Therefore, the controller was designed considering the friction and gravity compensation with $\boldsymbol{f}^*$ in (3.12) generated using the PSFT strategy. The final input to the manipulator was the torque, and the designed controller is defined as follows:

$$\boldsymbol{\tau} = \boldsymbol{J}^{\mathrm{T}} \boldsymbol{f}^* + \boldsymbol{\tau}_{\mathrm{fric}} + \boldsymbol{g}, \tag{3.15}$$

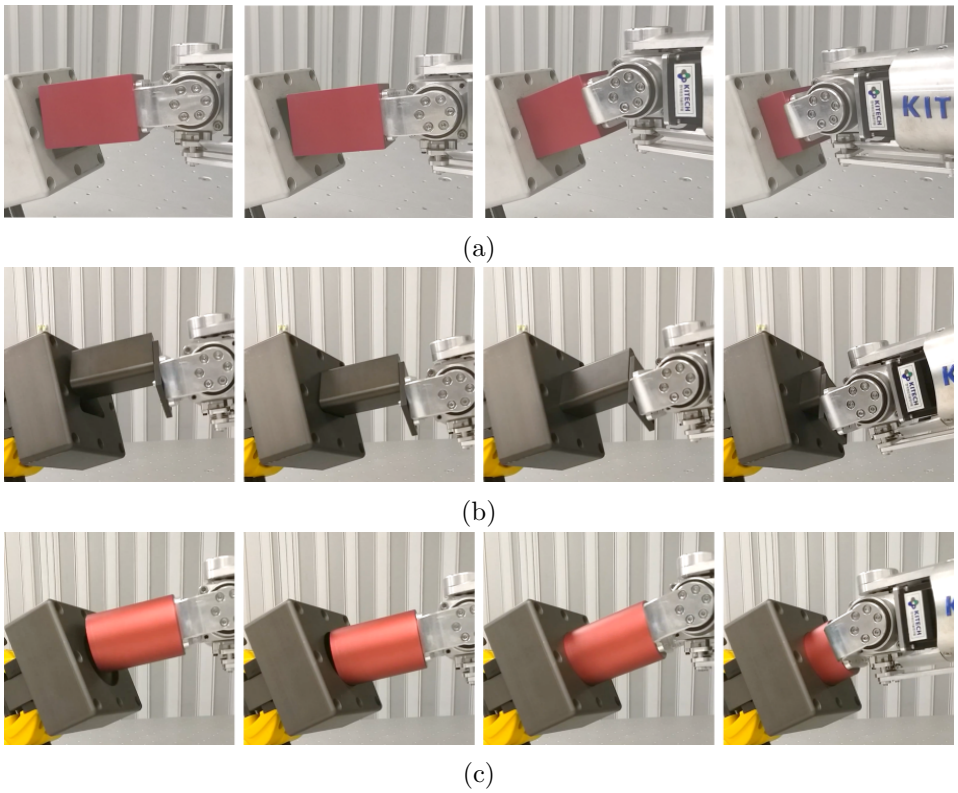

Figure 3.13: Snapshots of peg-in-hole experiment with PSFT; 2-point contact, 3-point contact, Insert, finish in sequence (a) square, (b) triangle, and (c) circle.

where $\boldsymbol{J}$ denotes the Jacobian matrix of the manipulator, $\boldsymbol{\tau}_{\mathrm{f}}$ denotes the joint friction compensation vector[22],[56], and $\boldsymbol{g}$ denotes the gravity compensation vector. k_p, k_ω, and f_a were set to 300, 3, and 7, respectively.

Fig. 3.13 presents snapshots of the square peg-in-hole experiment performed using the PSFT strategy. Fig. 3.14 shows the graph depicting the trajectory of the square peg during the experiment. The peg starts from the shifted position, approaches the hole, and makes the first contact. The peg moves until it reaches the three-point contact state and is then inserted into the hole.

Fig. 3.15 indicates the velocities, positions, and orientations of the peg dur-

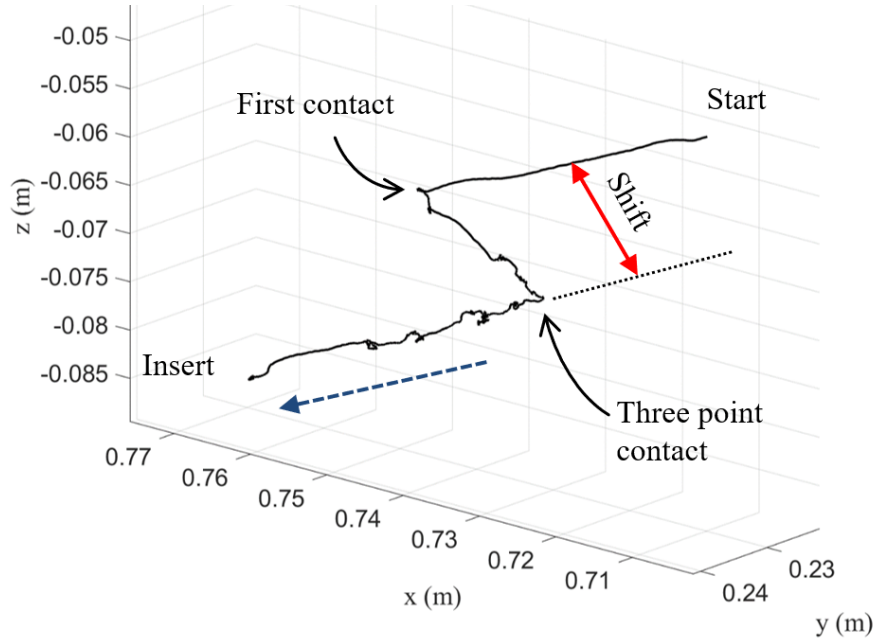

(a)

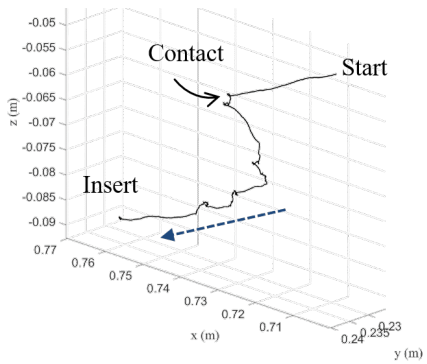

(b)

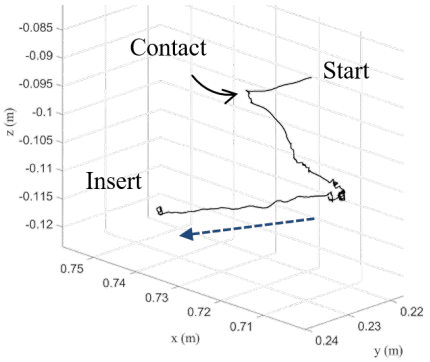

(c)

Figure 3.14: The trajectory of the peg in experiment (a) square, (b) circle, and (c) triangle.

ing the square peg-in-hole experiment carried out using the PSFT strategy. All the graphs were prepared according to global Cartesian coordinates. I have shown the graphs representing the worst scenarios because each step could not be clearly observed in most cases owing to the extremely rapid transitions be-

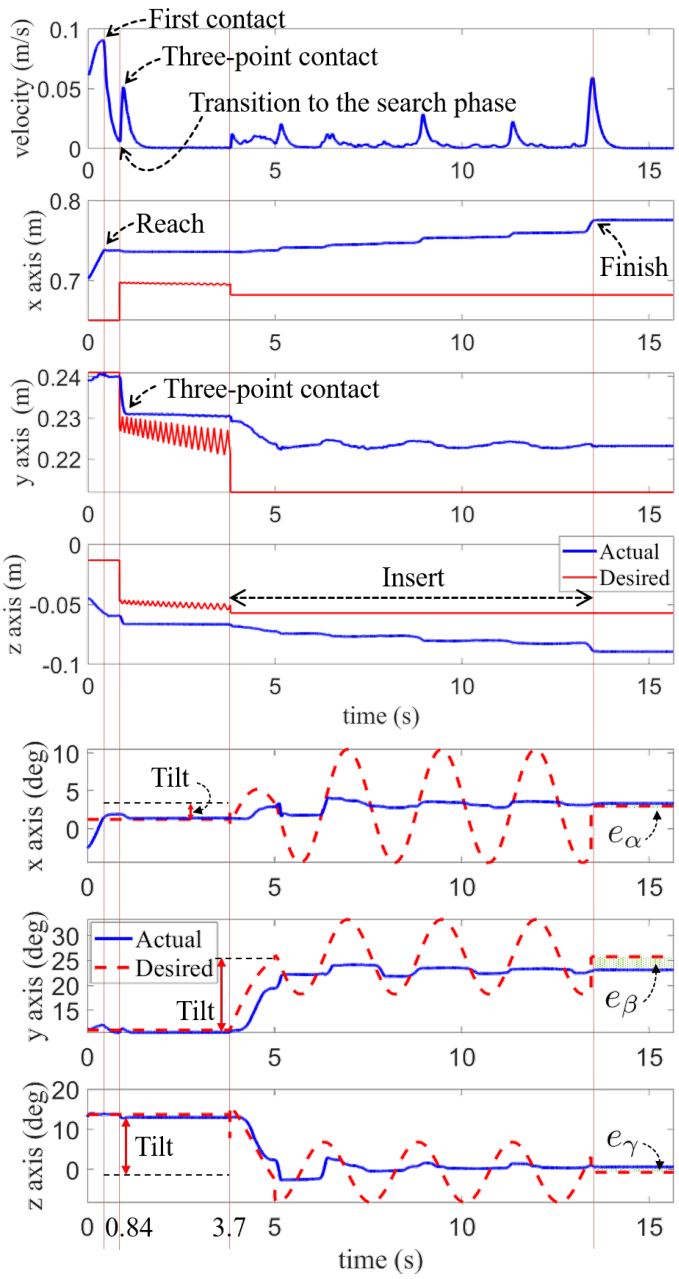

Figure 3.15: Velocity, position of the peg in global coordinate during peg-in-hole procedure.

Table 3.6: Performance comparison between SFT and PSFT strategies. Each experiment involved 20 trials.

Shape	Strategy	μ	σ	Success rate
Square	SFT	7.39 s	3.43 s	100 %
	PSFT	5.87 s	0.54 s	100 %
Circular	SFT	8.49 s	3.21 s	100 %
	PSFT	7.20 s	0.85 s	100 %
Triangular	SFT	15.78 s	12.84 s	100 %
	PSFT	10.92 s	1.07 s	100 %

tween the steps.

The first graph shows the change in the velocity of the peg. At 0.84 s, I can observe that when the velocity reaches zero after the first contact, the state transitions to the next phase. At 3.7 s, the search phase ends and transitions to the insert phase by ending the PSFT. The tilt motion is disabled and the peg exhibits a wiggling motion. In the graph showing the orientation of the peg, the difference between the desired and current values is because of compliance. In addition, the difference between target value and present value shown in the last phase is the initial uncertainty error.

Fig. 3.16 shows the histogram comparing the square peg-in-hole experiments. The proposed and spiral search strategies were executed 20 times each, and the average elapsed time and standard deviation are listed in Table 3.6. Similar to the simulation results, the standard deviations sharply reduced by 84.3%, 73.5%, and 91.7% in the square, circular and triangular cases, respectively. I confirmed that the mean elapsed time also reduced by 20.6%, 15.2%, and 30.8% in each case, respectively. In all cases, the success rate of the peg-in-hole process was 100%.

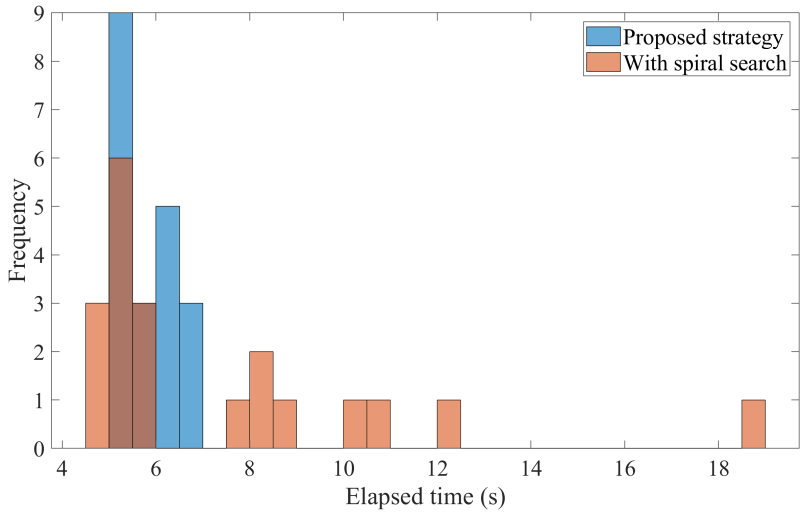

Figure 3.16: Histogram of the square peg-in-hole experiment comparing PSFT and SFT strategies.

Table 3.7 lists the performance of various strategies, including the one proposed in this paper. It is difficult to evaluate the performance of the strategy through the comparison of tolerance and time, because there are differences in the experimental environment such as the material, shape, and size of the assembled object, but it can be clearly seen that the proposed strategy is close to the state-of-the-art.

Table 3.7: Performance comparison between different strategies

Author	Category	Method	Clearance / Elapsed time
Kim et al.[58]	Sensing information with high precision control	FT sensor	0.1mm / 10s
Luo et al.[59]		FT sensor	0.02mm/46s
Tang et al.[60]		FT sensor	0.03mm/19s
Zhang et al.[61]		FT sensor	0.5mm/55s
Huang et al.[62]		Visual sensor	4mm/0.7s
Duque et al.[63]		Visual sensor with learning	1mm/43s
Jain et al.[64]	Compliant mechanism with high precision control	RCC with camera	0.5mm/3s
Baksys et al.[65]		RCC with vibratory devices	0.22mm/0.4s
Balletti et al.[66]		RCC	0.5mm/25s
Inoue, et al.[67]	Learing	Reinforcement learning	0.01mm / 4.68s Training 80min
Proposed strategy[22]	Compliance control based	A series of combination of unit motions	0.01mm / 4.5s

Chapter 4

CONCLUSIONS

In this research, I proposed a robotic peg-in-hole strategy given positional uncertainty. The strategy does not require any type of force or tactile sensor, because of which the robot's hardware and software structures can be simplified with higher potential for application to industries. First, the contact between the peg and the hole was analyzed, and basic units of motion were proposed based on the results. The peg-in-hole procedure, constructed by using a combination of unit motions and conditions for estimating the contact state, was then presented. The fundamental control law needed to attain the compliant characteristics and control framework for the strategy were addressed. Conditions for estimating the contact state were experimentally modified to find suitable ratios between the assembly force and the position control gain. The effectiveness of the method was verified by actual peg-in-hole experiments using a fifty-DoF humanoid upper body robot developed by Korea Institute of Industrial Technology. Method to find a suitable ratio between assembly force and position control gain was experimentally addressed. As a result of exper-

imentally analyzing the performance of the proposed strategy, it showed that the elapsed time is unpredictable. This is related to the force trajectory of the rubbing motion among the four unit motions. I proposed force trajectory for a compliance-based peg-in-hole strategy. The proposed strategy reduced the large variation of the elapsed time which is a disadvantage of the strategy with spiral force trajectory. I analyzed the problem of the spiral force trajectory, which is commonly used in the process of searching the hole position based on the uncertain information. The reason why spiral force trajectory has uncertainty in the elapsed time was analyzed using the probability concept. Based on the results, I propose partial spiral force trajectory with shift and tilt motion inspired by attractive region. The performance of the proposed strategy was compared with the existing strategy through simulations. Its effectiveness was confirmed through peg-in-hole experiments using three different shapes. According to the experiments conducted with square, circular, and triangular objects, the proposed method showed a dramatically reduced deviation of the elapsed time from 73.5 to 91.7 %, with a decreased mean elapsed time from 15.2 to 30.8 %. The effectiveness of the proposed method can provide practical advantages when implemented in production and assembly lines in future. When applied to actual assembly processes, the proposed method can help in predicting and managing the tact time of assembly tasks. In this research, only the polygonal shaped peg was considered to verify the proposed idea. The author's on-going research includes expanding and generalizing the proposed idea to the peg-in-hole case with more complex objects.

Bibliography

[1] J. Pauli, A. Schmidt, and G. Sommer, "Vision-based integrated system for object inspection and handling," *Robotics and autonomous systems*, vol. 37, no. 4, pp. 297-309, 2001.

[2] J. Miura and K. Ikeuchi, "Task-oriented generation of visual sensing strategies in assembly tasks," *IEEE Trans. Pattern Anal. Mach. Intell.*, vol. 20, no. 2, pp. 126-138, 1998.

[3] R. J. Chang, C. Y. Lin, and P. S. Lin, "Visual-based automation of peg-in-hole microassembly process," *J. Manuf. Sci. Eng.*, vol. 133, no. 4, pp. 041015, 2011.

[4] J. Kofman et al., "Teleoperation of a robot manipulator using a vision-based human–robot interface," *IEEE Trans. Ind. Electron.*, vol. 52, no. 5, pp. 1206-1219, 2005.

[5] G. Du and P. Zhang, "A makerless human-robot interface using particle filter and Kalman filter for dual robots," *IEEE Trans. Ind. Electron.*, vol. 62, no. 4, pp. 2257-2264, 2015.

[6] B. Shirinzadeh, Y. Zhong, P. D. W. Tilakaratna, Y. Tian, and M. M. Dalvand, "A hybrid contact state analysis methodology for robotic-based ad-

justment of cylindrical pair," *Int. J. Adv. Manuf. Technol.*, vol. 52, no. 1, pp. 329-342, 2011.

[7] H.-C. Song, Y.-L. Kim, and J.-B. Song, "Guidance algorithm for complex-shape peg-in-hole strategy based on geometrical information and force control," *Advanced robotics*, vol. 30, no. 8, pp. 552-563, 2016.

[8] A. Lopes and F. Almeida, "A force-impedance controlled industrial robot using an active robotic auxiliary device," *Robotics and computer-integrated manufacturing*, vol. 24, no. 3, pp. 299-309, 2008.

[9] J. Oh and J.-H. Oh, "A modified perturbation/correlation method for force-guided assembly," *J. mechanical science and technology*, vol. 29, no. 12, pp. 5437-5446, 2015.

[10] W. S. Newman, Y. Zhao, and Y.-H. Pao, "Interpretation of force and moment signals for compliant peg-in-hole assembly," in *Proc. IEEE Int. Conf. Robot. Autom.*, pp. 571-576, 2001.

[11] M. W. Abdullah, H. Roth, M. Weyrich, and J. Wahrburg, "An approach for peg-in-hole assembling using intuitive search algorithm based on human behavior and carried by sensors guided industrial robot," *15th IFAC Symp. information control problems in manufacturing*, vol. 48, no. 3, pp. 1476-1481, 2015.

[12] F. Dietrich et al., "On Contact Models for Assembly Tasks: Experimental Investigation Beyond the Peg-in-Hole Problem on the Example of Force-Torque Maps," in *Proc. IEEE Int. Conf. Intell. Robots Syst.*, pp. 2313-2318, 2010.

[13] S. R. Chhatpar and M. S. Branicky, "Search strategies for peg-in-hole assemblies with position uncertainty," in *Proc. IEEE Int. Conf. Intell. Robots Syst.*, pp. 1465-1470, 2001.

[14] A. D. Luca and R. Mattone, "Sensorless robot collision detection and hybrid force/motion control," in *Proc. IEEE Int. Conf. Robot. Autom.*, pp. 999-1004, 2005.

[15] H. Lee and X. Zhao, and J. Wahrburg, "An active sensing strategy for contact location without tactile sensors using robot geometry and kinematics," *Autonomous robots*, vol. 36, no. 1, pp. 109-121, 2013.

[16] H. Park, J.-H. Bae, J.-H. Park, M.-H. Baeg, and J. park, "Intuitive peg-in-hole assembly strategy with a compliant manipulator," in *44th Int. Symp. on robotics*, pp. 1-5, 2013.

[17] T. Lozano-Pérez, M. T. Mason, and R. H. Taylor, "Automatic synthesis of fine-motion strategies for robots," *Int. J. Robotics Res.*, vol. 3, no 1, pp.3-24, 1984.

[18] W. Haskiya, H. Qiao, and J. A. G. Knight, "A new strategy for chamferless peg-hole assembly," in *IEEE Int. Symp. on assembly and task planning*, pp. 90-95, 1997.

[19] B. Huard et al., "Sensorless force/position control of a single-acting actuator applied to compliant object interaction," *IEEE Trans. Ind. Electron.*, vol. 62, no. 6, pp. 3651-3661, 2015.

[20] Q. Xu, "Robust impedance control of a compliant microgipper for high-speed position/force regulation," *IEEE Trans. Ind. Electron.*, vol. 62, no. 2, pp. 1201-1209, 2015.

[21] S. G. Khan et al., "Compliance control and human-robot interaction: part 1 - survey," *Int. J. Humanoid Robotics*, vol. 11, no 3, pp.1430001, 2014.

[22] H. Park, J. Park, D.-H. Lee, J.-H. Park, M.-H. Baeg, and J.-H. Bae, "Compliance-based robotic peg-in-hole assembly strategy without force feedback," *IEEE Trans. Ind. Electron.*, vol. 64, no. 8, pp. 6299-6309, Aug. 2017.

[23] T. Inoue, G. D. Magistris, A. Munawar, T. Yokoya, and R. Tachibana, "Deep reinforcement learning for high precision assembly tasks," in *Proc. IEEE Int. Conf. Intell. Robots Syst.*, 2017. pp. 819-825.

[24] G. Thomas *et al.*, "Learning robotic assembly from CAD," in *Proc. IEEE Int. Conf. Robot. Autom.*, 2018. pp. 3524-3531.

[25] L. Roveda, G. Pallucca, N. Pedrocchi, F. Braghin, and L. M. Tosatti, "Iterative learning procedure with reinforcement for high-accuracy force tracking in robotized tasks," *IEEE Trans. Ind. Informat.*, vol. 14, no. 4, pp. 1753-1763, Apr. 2018.

[26] C. B. Ahn, J. H. Kim, and Z. H. Cho, "High-speed spiral-scan echo planar NMR imaging-I," *IEEE Trans. on medical imaging*, vol. 5, no. 1, pp. 2-7, 1986.

[27] C. Galuzzi, K. Bertels, and S. Vassiliadis, "The spiral search: A linear complexity algorithm for the generation of convex MIMO instruction-set extensions," in *Int. Conf. on field-programmable technology*, pp. 12-14, 2007.

[28] B. Siciliano, et al., *Robotics: modelling, planning and control*, Springer, London, 2009.

[29] S. Arimoto, M. Sekimoto, H. Hashiguchi, and R. Ozawa, "Natural resolution of ill-posedness of inverse kinematics for redundant robots: A challenge to Bernstein's degrees-of-freedom problem," *Advanced robotics*, vol. 19, no. 4, pp. 401-434, 2012.

[30] M. Takegaki and S. arimoto, "A new feedback method for dynamic control of manipulators," *J. Dyn. Sys., Meas., Control*, vol. 103, no. 2, pp. 119-125, 1981.

[31] O. Khatib, "A unified approach for motion and force control of robot manipulators: The operational space formulation," *IEEE J. Robotics and Automation*, vol. 3, no. 1, pp. 43-53, 1987.

[32] J.-H. Bae et al., "Task space control considering passive muscle stiffness for redundant robotic arms," *Intelligent Service Robotics*, vol. 8, no. 2, pp. 93-104, 2015.

[33] M. Sekimoto and S. Arimoto, "Experimental study on reaching movements of robot arms with redundant DoFs based upon virtual spring-damper hypothesis," in *Proc. IEEE Int. Conf. Intell. Robots Syst.*, pp. 562-567, 2006.

[34] H. Park et al, "Robotic peg-in-hole assembly by hand arm coordination," *The Journal of Korea Robotics Society*, vol. 10, no. 1, pp. 42-51, 2015.

[35] Z. Li and S. S. Sastry, "Task-oriented optimal grasping by multifingered robot hands," *IEEE J. Robot. Autom.*, vol. 4, no. 1, pp. 32-44, 1988.

[36] D. Williams and O. Khatib, "The virtual linkage: a model for internal forces in multi-grasp manipulation," in *Proc. IEEE Int. Conf. Robot. Autom.*, pp. 1025-1030, 1993.

[37] R. C. Bonitz and T. C. Hsia, "Internal force-based impedance control for cooperating manipulators," *IEEE Trans. Robot. Autom.* vol. 12, no. 1, pp. 78-89, 1996

[38] S. A. Schneider and J. R. H. Cannon, "Object impedance control for cooperative manipulation: theory and experimental results," *IEEE Trans. Robot. Autom.* vol. 8, no. 3, pp. 383-394, 1992

[39] F. Caccavale, S. Chiaverini, C. Natale, B. Siciliano, and L. Villani, "Geometrically consistent impedance control for dual-robot manipulation," in *Proc. IEEE Int. Conf. Robot. Autom.*, pp. 3873-3878, 2000.

[40] O. Khatib, "Inertial properties in robotic manipulation: an object-Level framework," *Int. J. Robot. Res.*, vol. 14, no. 1, pp. 19-36, 1995.

[41] T. Wimböck, C. Ott, A. Albu-Schäffer, and G. Hirzinger, "Comparison of object-level grasp controllers for dynamic dexterous manipulation," *Int. J. Robot. Res.*, vol. 31, no. 1, pp. 3-23, 2011.

[42] T. Wimboeck, C. Ott, and G. Hirzinger, "Passivity-based object-level impedance control for a multifingered hand," in *Proc. IEEE Int. Conf. Intell. Robots Syst.*, pp. 1025-1030, 1993.

[43] A. B. A. Cole, J. E. Hauser, and S. S. Sastry, "Kinematics and control of multifingered hands with rolling contact," *IEEE Trans. Autom. Control*, vol. 34, no. 4, pp. 398-404, 1989.

[44] V. D. Sapio and J. Park, "Multitask constrained motion control using a mass-weighted orthogonal decomposition," *J. Appl. Mech.*, vol. 77, no. 4, 041004, 2010.

[45] J.-H. Bae, S.-W. Park, D. Kim, M.-H. Baeg, and S.-R. Oh, "A grasp strategy with the geometric centroid of a groped object shape derived from contact spots," in *Proc. IEEE Int. Conf. Robot. Autom.*, pp. 3798-3804, 2012.

[46] J.-H. Bae, S. Arimoto, Y. Yamamoto, H. Hashiguchi, and M. Sekimoto, "Reaching to grasp and preshaping of multi-DOFs robotic hand-arm systems using approximate configuration of objects," in *Proc. IEEE Int. Conf. Intell. Robots Syst.*, pp. 3798-3804, 2012.

[47] S. Arimoto, K. Tahara. J.-H. Bae, and M. Yoshida, "A stability theory of a manifold:concurrent realization of grasp and orientation control of an object by a pair of robot fingers," *Robotica*, vol. 21, no. 2, pp. 163-178, Mar. 2003.

[48] M. Yoshida, S. Arimoto, and J.-H. Bae, "Blind grasp and manipulation of a rigid object by a pair of robot fingers with soft tips," in *Proc. IEEE Int. Conf. Robot. Autom.*, pp. 4707-4714, 2007.

[49] S. Arimoto, M. Yoshida, and J.-H. Bae, "Stable blind grasping of a 3-D object under non-holonomic constraints," in *Proc. IEEE Int. Conf. Robot. Autom.*, pp. 2124-2130, 2006.

[50] H. Park, J. Park, D.-H. Lee, J.-H. Park, and J.-H. Bae, "Compliant peg-in-hole assembly using partial spiral force trajectory with tilted peg posture," *IEEE Robot. Autom. Letters*, vol. 5, no. 3, pp. 4447-4454, Jul. 2020.

[51] H. Qiao *et al.*, "The concept of attractive region in environment and its application in high-precision tasks with low-precision systems," *IEEE/ASME Trans. Mechatronics*, vol. 20, no. 5, pp. 2311-2327, Oct. 2015.

[52] R. Li and H. Qiao, "Condition and strategy analysis for assembly based on attractive region in environment," *IEEE/ASME Trans. Mechatronics*, vol. 22, no. 5, pp. 2218-2228, Oct. 2017.

[53] K. V. Wyk, M. Culleton, J. Falco, and K. Kelly, "Comparative peg-in-hole testing of a force-based manipulation controlled robotic hand," *IEEE Trans. Robot.*, vol. 34, no. 2, pp. 542-549, Apr. 2018.

[54] H. Park *et al.*, "Dual arm peg-in-hole assembly with a programmed compliant system," in *Proc. IEEE Int. Conf. on ubiquitous robots and ambient intelligence*, 2014, pp. 431-433.

[55] B. Siciliano *et al.*, *Robotics: Modelling, Planning and Control*, London, U.K.: Springer, 2009.

[56] M. Sekimoto and S. Arimoto, "Experimental study on reaching movements of robot arms with redundant DoFs based upon virtual spring-damper hypothesis," in *Proc. IEEE Int. Conf. Intell. Robots Syst.*, 2006, pp. 562-567.

[57] D.-H. Lee, H. Park, J.-H. Park, M.-H. Baeg, and J.-H. Bae, "Design of an anthropomorphic dual-arm robot with biologically inspired 8-DOF arms," *Intelligent service robotics*, vol. 10, no. 2, pp. 137-148, Apr. 2017.

[58] Y. L. Kim, H. C. Song, and J. S. Song, "Hole detection algorithm for chamferless square peg-in-hole based on shape recognition using F/T sensor," *Int. J. Precis. Eng. Manuf.*, vol. 15, no. 3, pp. 425-432, Mar. 2014.

[59] R. C. Luo, A. Chang, and L. Cheng, "A novel peg-in-hole approach based on geometrical analysis for inclined uncertainty," in *Proc. IEEE Int. Conf. Adv. Intell. Mechatronics*, 2017, pp. 891-896.

[60] T. Tang, H.-C. Lin, Y. Zhao, W. Chen, and M. Tomizuka, "Autonomous alignment of peg and hole by force/torque measurement for robotic assembly," in *IEEE International Conference on Automation Science and Engineering*, 2016, pp. 162-167.

[61] X. Zhang, Y. Zheng, J. Ota, and Y. Huang, "Peg-in-hole assembly based on two-phase scheme and F/T sensor for dual-arm robot," *Sensors*, vol. 17, no. 9, pp. 1-19, Sep. 2017.

[62] S. R. Huang, K. Murakami, Y. Yamakawa, T. Senoo, and M. Ishikawa, "Fast peg-and-hole alignment using visual compliance," in *Proc. IEEE/RSJ Int. Conf. Intell. Robots Syst.*, pp. 286-292, 2013.

[63] D. A. Duque, F. A. Prieto, and J. G. Hoyos, "Trajectory generation for robotic assembly operations using learning by demonstration," *Robot. Comput. Integr. Manuf.*, vol. 57, pp. 292-302, Jun. 2019.

[64] R. K. Jain, S. Majumder, and A. Dutta, "SCARA based peg-in-hole assembly using compliant IPMC micro gripper," *Robotics and autonomous systems*, vol. 61, no. 3, Mar, 2013.

[65] B. Baksys, J.Baskutiene, A. B. Povilionis, andK.Ramanuskyte, "Sensorless vibratory manipulation of the automatically assembled parts," *Solid State Phenom.*, vol. 164, pp. 265-270, 2010.

[66] L. Balletti et al., "Towards variable impedance assembly: The VSA peg-in-hole," in *Proc. 12th IEEE-RAS Int. Conf. Humanoid Robots*, pp. 402-408, 2012.

[67] T. Inoue, G. D. Magistris, A. Munawar, T. Yokoya, and R. Tachibana, "Deep reinforcement learning for high precision assembly tasks," in *Proc. IEEE Int. Conf. Intell. Robots Syst.*, pp. 819-825, 2017.

초 록

펙인홀 조립은 로봇의 접촉 작업을 대표하는 작업으로, 펙인홀 조립 전략을 연구함으로써 산업 생산 분야의 조립작업에 적용할 수 있다. 펙인홀 조립작업은 일반적으로 펙과 홀 간의 접촉상태를 추정함으로써 이루어진다. 접촉상태를 추정하기 위해 가장 널리 쓰이는 방법은 힘 센서를 사용하는 것인데, 접촉 힘과 모멘트를 측정하여 접촉상태를 추정하는 방식이다. 만약 이러한 센서를 사용하지 않을 수 있다면, 하드웨어 비용과 소프트웨어 연산량 감소 등의 장점이 있음은 자명하다. 본 논문에서는 힘 센서 혹은 수동 컴플라이언스 장치를 사용하지 않는 펙인홀 전략을 제안한다. 홀에 대한 인식 오차 혹은 로봇의 제어 오차를 극복하기 위하여 먼저 펙과 홀의 접촉 가능 상태를 분석하고 로봇의 컴플라이언스 모션을 위한 제어 프레임워크를 디자인한다. 전략은 컴플라이언스 특징에 기반하며 펙에 힘과 모멘트를 생성시킴으로써 조립작업을 수행한다. 펙은 외부환경에 순응함으로써 홀에 삽입된다. 제안한 전략은 낮은 공차를 갖는 펙인홀 실험을 통해서 그 유효성이 검증된다. 펙과 홀을 로봇팔과 외부환경에 각각 고정된 환경에서의 실험, 인간형 로봇핸드를 이용하여 펙을 잡아서 고정된 홀에 삽입하는 실험, 그리고 테이블에 놓인 펙과 홀을 각각 로봇핸드로 파지하여 조립하는 총 세 가지의 실험을 수행하였다. 핸드로 펙을 파지하고 조작하기 위하여, 파지 방법과 핸드를 이용한 물체 조작 알고리즘을 간략히 소

개하였다. 제안한 전략의 성능을 실험적으로 분석한 결과, 높은 조립 성공률을 갖는 대신 조립시간이 예측할 수 없는 단점이 나타나 이를 보완하기 위해서 렌치 궤적 또한 제안하였다. 먼저 가장 일반적으로 사용되는 나선 힘 궤적을 이용했을 때 조립 성공시간의 분산이 큰 이유를 확률개념을 이용해 분석하고, 이를 보완하기 위한 부분적 나선 힘 궤적을 제안한다. 제안한 힘 궤적이 나선 힘 궤적에 비해 갖는 성능의 우수성을 증명하기 위하여 수치적 분석, 반복적 시뮬레이션, 그리고 로봇을 이용한 실험을 수행하였다.

주요어: 컴플라이언스 조립, 펙인홀 전략, 힘 제어

학번: 2014-30817